



NTNU – Trondheim
Norwegian University of
Science and Technology

Vortex Induced Vibrations Of Slender Marine Structures

Inverse Analysis

Daming Wang

Marine Technology

Submission date: June 2013

Supervisor: Carl Martin Larsen, IMT

Norwegian University of Science and Technology
Department of Marine Technology



M.Sc. thesis 2013

for

Stud. tech. Daming Wang

VORTEX INDUCED VIBRATIONS OF SLENDER MARINE STRUCTURES – INVERSE ANALYSIS

(Virvelindusert respons i slanke marine konstruksjoner)

VIV has been studied experimentally at MARINTEK/NTNU for almost two decades. These experiments include flexibly supported rigid cylinders, forced motion of rigid cylinders and long, flexible beams. The overall aim has been to improve the understanding of VIV and thereby establish a reliable response model for prediction of VIV. One result of this effort is the computer program VIVANA that can calculate fatigue damage caused by VIV for a large variety of slender marine structures.

A key issue for programs like VIVANA is to establish a data base for hydrodynamic coefficients that are used as parameters in a semi-empirical model. Such coefficients have so far been found from dedicated experiments with rigid cylinders; spring supported or with forced motions. An alternative to such experiments is to measure the response in flexible beams in current, and calculate local forces from observed accelerations and/or bending strains. This method is referred to as “system identification” or “inverse analysis”.

Other uncertainties of equal importance are related to damping from fluid/structure interaction outside the excitation zone and the contribution to fatigue from higher order frequency components of the response. Improved understanding of both issues can be obtained from analysis of data from experiments.

The work may be divided into the following activities:

1. Apply system identification techniques to estimate excitation and damping coefficients from experiments
2. Compare results to existing models in VIVANA for excitation and damping
3. Calculate fatigue damage from varying frequency intervals in order to find the contribution from the primary CF frequency and higher order frequency components

The work may show to be more extensive than anticipated. Some topics may therefore be left out after discussion with the supervisor without any negative influence on the grading.

The candidate should in her/his report give a personal contribution to the solution of the problem formulated in this text. All assumptions and conclusions must be supported by mathematical models and/or references to physical effects in a logical manner.

The candidate should apply all available sources to find relevant literature and information on the actual problem.

The report should be well organised and give a clear presentation of the work and all conclusions. It is important that the text is well written and that tables and figures are used to support the verbal presentation. The report should be complete, but still as short as possible.

The final report must contain this text, an acknowledgement, summary, main body, conclusions and suggestions for further work, symbol list, references and appendices. All figures, tables and equations must be identified by numbers. References should be given by author name and year in the text, and presented alphabetically by name in the reference list. The report must be submitted in two copies unless otherwise has been agreed with the supervisor.

The supervisor may require that the candidate should give a written plan that describes the progress of the work after having received this text. The plan may contain a table of content for the report and also assumed use of computer resources.

From the report it should be possible to identify the work carried out by the candidate and what has been found in the available literature. It is important to give references to the original source for theories and experimental results.

The report must be signed by the candidate, include this text, appear as a paperback, and - if needed - have a separate enclosure (binder, DVD/ CD) with additional material.

Supervisor at NTNU is professor Carl M. Larsen
Contact person at MARINTEK is Jie Wu

Trondheim, February 2013

Carl M. Larsen

Submitted: January 2013
Deadline: June 10 2013

Master Thesis 2013

**VORTEX INDUCED VIBRATIONS
OF SLENDER MARINE
STRUCTURES – INVERSE
ANALYSIS**

Daming Wang

Adviser: Carl. Martin. Larsen

Contact Person: Jie Wu

Jun 10, 2013

Abstract

With the development of the offshore engineering and the increasing of water depth, VIV (vortex induced vibrations) becomes a big challenge of the design of slender marine structures.

In engineering field, we use some empirical VIV prediction codes like VIVAVA and Shear 7 to predict VIV. A key issue for using the codes is to establish a data base for hydrodynamic coefficients. Such coefficients have so far been found from experiments. An alternative way to get the force coefficients is to measure the response in flexible beams in current, and get the local force using some mathematical calculation method, which is called inverse analysis.

In this project, we analyzed 44 NDP riser model tests. First we apply inverse analysis method to estimate the excitation force coefficients for one test and make comparison with the previous results from the rigid pipe model test. And we can find out the inverse analysis method is quite an efficient way to calculate the force coefficients.

Second we compare the results with the existing models in VIVAVA for excitation and damping coefficients. We can see that the model in VIVAVA can give more reasonable results of the damping coefficients compared with inverse analysis when the non-dimensional frequency is outside the excitation range.

Third we calculate the fatigue damage from the varying frequency components in order to find the contribution from the primary cross flow frequency and higher order frequency. We find that the fatigue generated by higher order frequency components is as important as that from the primary cross flow frequency component and cannot be neglected. We can introduce a parameter which can be used to find out the total fatigue damage from the primary frequency fatigue damage.

Acknowledgements

This thesis work was carried out in Norwegian University of Technology and Science (NTNU).

First of all, I want to acknowledge my supervisor, Prof. Carl Martin Larsen from NTNU. I thank him for guiding me through the whole semester with his invaluable experience and enthusiastic encouragement

I feel grateful to Jie Wu from MARINTEK for sharing his Matlab programs in inverse analysis, and for his help and patience during my study.

I also would like to thank my friends at the marine technology center at Tyholt. I've learned a lot from PhD candidate Cheng Li and Zhao He. I also enjoyed the friendship with other students.

Thanks to my parents, they also gave me a lot of advice and money for my study in Norway.

Contents

Abstract	2
Acknowledgements	3
Contents	4
Nomenclature	6
1 Introduction	9
1.1 Background	9
1.2 Research Objectives	10
1.3 Thesis Outline	10
2 Theoretical Background	12
2.1 Vortex Induced Vibration	12
2.2 Extracting Hydrodynamic Force coefficients	16
2.2.1 Rigid Pipe Tests with Harmonic Motion	16
2.2.2 Rigid Pipe Tests with Observed Orbits	17
2.3 Empirical Program VIVAVA	19
2.3.1 Experiment Environment (NDP High Mode Test)	19
2.3.2 Experiment Environment (Rotating Rig Test)	20
2.4 Empirical Program VIVAVA	22
2.4.1 Analysis Procedure	22
2.4.2 Hydrodynamic Load Model	22
3 Force coefficient Identification by Inverse Analysis Method	24
3.1 Introduction	24
3.2 Finite Element Beam Model	25
3.3 Pre-Processing Measurements	26
3.4 Inverse Analysis Based on Optimal Control Theory	27
4 Application of Inverse Analysis on Flexible Beam VIV Experiments	30
4.1 Inverse Analysis for NDP Test of Sheared Current Flow	30
4.1.1 NDP Shear flow Case 2340	30
4.1.2 Results of Different Sensitivity of Weighting Parameters	31
4.2.3 Calculation of Excitation and Added Mass Coefficients along the Riser	36
4.2.4 Contour Plot of Excitation and Added Mass Coefficients	37

4.2 Inverse Analysis for NDP High Mode Tests of Uniform Current Flow	40
4.2.1 NDP High Mode Test 2030	40
4.2.2 Results of Different weighting parameters.....	40
4.2.3 Calculation of Excitation and Added Mass Coefficients along the Riser	43
4.3 Summary	46
5 Comparison of Excitation Coefficients.....	47
5.1 The Venugopal's Damping Model	47
5.1.1 Dimensional Damping Coefficients.....	47
5.1.2 Non-Dimensional Damping Coefficients.....	48
5.2 Calculation for Non-Dimensional Damping Coefficients.....	50
5.3 Summary	54
6 Fatigue Analysis for NDP High Mode Tests	55
6.1 Pre-Processing of 44 NDP Test Cases	55
6.1.1 Introduction	55
6.1.2 Band Pass Filtering of the Experiment Data.....	60
6.2 Calculation of Non-Dimensional Amplitude and Stress along the Riser	65
6.2.1 Non-Dimensional Amplitude Analysis.....	65
6.2.2 Standard Deviation of Stress of NDP tests	69
6.3 Calculation of Annual Cumulative Fatigue Damage along the Riser	70
6.3.1 SN Curve	70
6.3.2 Rain Flow Counting Method	70
6.3.3 Miner Summation.....	71
6.3.4 Total, $1 \times \omega$ and $3 \times \omega$ Frequency Component Fatigue Damage.....	72
6.3.5 Difference of Total, $1 \times \omega$ and $3 \times \omega$ Fatigue Damage.....	74
6.3.6 Ratio of Fatigue Damage of Total, $1 \times \omega$ and $3 \times \omega$ Frequency Component.....	76
6.3.7 Contour plots for the Ratio of Fatigue Damage of Total, $1 \times \omega$ and $3 \times \omega$ Frequency Component.....	77
6.3.8 Average Value and Standard Deviation of the Ratio of Fatigue Damage of Total, $1 \times \omega$ and $3 \times \omega$ Frequency Component	79
6.3.9 Influence of Different SN Curve on the Results of the Fatigue analysis.....	80
6.4 Summary	83
7 Conclusions	84
7.1 Summary of Present Work	84
7.2 Recommendation of Future Work	85
A Annual Cumulative Fatigue Damage Results of NDP Tests	86
A.1 Comparison of Annual Cumulative Fatigue Damage Results for Total, $1 \times \omega$ and $3 \times \omega$ Frequency Component for Shear Flow Cases.....	86
A.2 Comparison of Annual Cumulative Fatigue Damage Results for Total, $1 \times \omega$ and $3 \times \omega$ Frequency Component for Uniform Flow Cases	99
B Annual Cumulative Fatigue Damage Results of NDP Tests	110
B.1 Comparison of Annual Cumulative Fatigue Damage Ratio for Total, $1 \times \omega$ and $3 \times \omega$ Frequency Component for Shear Flow Cases.....	110
B.2 Comparison of Annual Cumulative Fatigue Damage Ratio for Total, $1 \times \omega$ and $3 \times \omega$ Frequency Component for Uniform Flow Cases	122
Bibliography	133

Nomenclature

Abbreviations

1D	One dimensional
2D	Two dimensional
3D	Three dimensional
CF	Cross flow
CFD	Computational Fluid Dynamics
IL	In-line
MIT	Massachusetts Institute of Technology
NDP	Norwegian Deepwater Program
NTNU	Norwegian University of Science and Technology
VIV	Vortex Induced Vibration

Greek Symbols

\mathcal{E}	Strain
Γ	Input matrix
κ	Curvature
λ	Lagrange multiplier
μ	Viscosity
ω	Circular frequency
ω_{osc}	Oscillation frequency
ϕ	Mode shape

Φ	Mode shape matrix
σ_F	Standard deviation of error between estimated force and true force
σ_Z	Standard deviation of error between estimated displacement and true displacement
Θ	System matrix in discrete time domain
θ	Phase angle between IL and CF displacement
ν	Kinematic viscosity

Mathematical Symbols

$\dot{\nabla}, \ddot{\nabla}$	Time derivatives
$\frac{\partial \nabla}{\partial \nabla}$	Partial derivative
∇^T	Matrix transpose

Roman symbols

γ	Weight factor
\hat{f}	Non-dimensional frequency
A	Displacement amplitude
C	Damping matrix
C_a	CF added mass coefficient
C_e	CF excitation coefficient
D	Pipe diameter
E	Young's modulus
F	Hydrodynamic force
f_0	Cylinder eigen frequency in still water
f_v	Vortex shedding frequency
j_Z, j_F, j_X	Cost functions for measurements, external forces and state vectors respectively

K	Stiffness matrix
L	Pipe length
M	Mass Matrix
m	Mass per unit length
Q	Measurement noise variance matrix
Q_{ZZ}, Q_{FF}, Q_{XX}	Error covariance matrix for measurements external forces and state vectors respectively
R	Process noise covariance matrix
Re	Reynolds number
St	Strouhal number
T	Oscillation period
t	Time variable
U	Current velocity
U_r	Reduced velocity
X	State vector
x	Displacement in IL direction
Y	Displacement vector
y	Displacement in CF direction
Z	Measured vector
\hat{z}	Displacement obtained from measured acceleration

Chapter 1

Introduction

1.1 Background

Slender marine structures are extremely important for offshore industry and oil production. Risers which are exposed in the waves and current will suffer from vortex induced vibrations (VIV), causing fast accumulation of fatigue damage. Another consequence is that in-line drag will be amplified. This will lead to the static displacement in current and create some problem for the drilling and workover risers. With the development of the offshore industry, the prediction of the riser response becomes more and more important.

Nowadays we can use some codes and programs to predict VIV on risers. Some of the present VIV prediction tools available for industry practice are the empirical models, VIVAVA, VIVA, and SHEAR7. See figure 1.1.

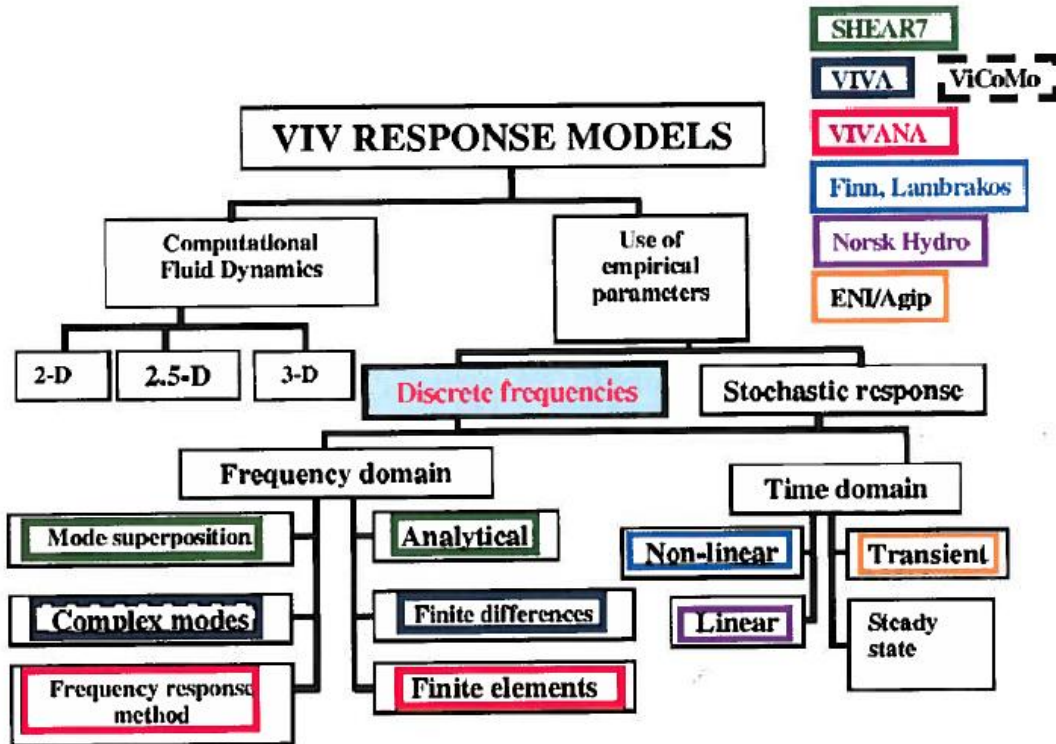


Figure 1.1: classification of some VIV prediction models. Figure from Larsen [2]

However, the flow conditions are much more complicated in the fields than in the lab. Some important aspects of VIV phenomenon of a flexible pipe, such as the interaction of CF and IL, the Reynolds number effects, and higher order force components have not been sufficiently modeled in the coefficient database obtained from rigid pipe experiments.

1.2 Research Objectives

The overall objective is to get a better understanding of the VIV of slender marine structures .

Find a reliable and simpler tool to identify hydrodynamic forces coefficients from limited number of measurements of riser VIV experiments (accelerations and strains).

After finding the hydrodynamic coefficients, we have to compare the results with the present code VIVAVA in order to find the difference.

Then we need to do the fatigue analysis for the NDP riser model tests to calculate the cumulative fatigue damage and make comparison with VIVANA.

1.3 Thesis Outline

The project is organized as the following 7 chapters:

Chapter 2 gives an overview of the VIV phenomenon and defines some important parameters which are used in the thesis. Review some different ways to extract hydrodynamic force coefficients from experiments.

Chapter 3 introduces inverse analysis method which can identify external forces from experimental measurements along the riser.

Chapter 4 applied the inverse analysis method into two NDP flexible riser VIV experiment data, one for shear flow case and the other for uniform flow case. Hydrodynamic forces along the riser are identified and the force coefficients are calculated. The trends of the obtained force coefficients are studied. The differences with existing data are compared.

In chapter 5, compare the excitation coefficients from inverse analysis with the results from damping model in VIVANA-the Venugopal's damping model.

In chapter 6, analyze 44 NDP tests, including 2 shear flow cases and 22 uniform flow cases, calculate the annual cumulative fatigue damage for different cases along the riser. Find out the parameters which can be used in VIVANA to get the total fatigue damage.

In chapter 7, major contributions in this research work is summarized. Conclusions are drawn and recommendations for future work are proposed.

Chapter 2

Theoretical Background

2.1 Vortex Induced Vibration Phenomenon

Vortex Shedding

When the water flows towards the cylinder, the high fluid pressure close to the leading edge impels the flow to the cylinder as boundary layers develop on both sides of the riser.

But the high pressure is not enough to force the flow to go back to the cylinder at high Reynolds numbers. The boundary layers separate from each side of the cylinder surface and become two shear layers that trail after in the flow and bound the wake. Since the inner part of the shear layers is in contact with the cylinder moves much more slowly than the outside portion of the shear layers. The shear layers roll into the wake close by, they fold on each other and become discrete vortices.

The vortices interact with the cylinder are called vortex induced vibration, see figure 2.1. Ref. Blevins[3]

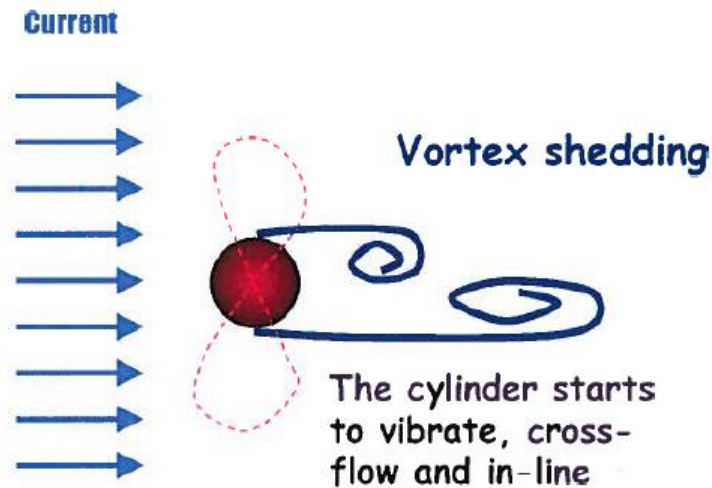


Figure 2.1 Vortex shedding. Figure from Larsen [4]

The vortices shedding generate time varying pressure over the cylinder. Integrated over the cylinder surface and can give rise to the lift force in cross flow (CF) direction and drag force in in line (IL) direction. The lift force oscillates at the vortex shedding frequency of the cylinder; while the drag force oscillates at twice the vortex shedding frequency.

Flow Regimes

The parameter describing the flow around a cylinder depends on the Reynolds number Re .

$$Re = \frac{UD}{\nu} \quad (2.1)$$

In eq 2.1, U is the flow speed, D is the cylinder diameter, ν is the kinematic viscosity. The detailed classification of flow regimes is shown in figure 2.2:




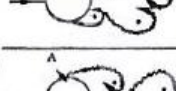

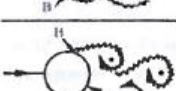
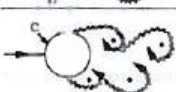

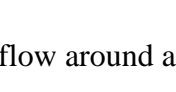
a)		No separation. Creeping flow	$Re < 5$
b)		A fixed pair of symmetric vortices	$5 < Re < 40$
c)		Laminar vortex street	$46 < Re < 200$
d)		Transition to turbulence in the wake	$200 < Re < 300$
e)		Wake completely turbulent. A: Laminar boundary layer separation	$300 < Re < 3 \times 10^5$ Subcritical
f)		A: Laminar boundary layer separation B: Turbulent boundary layer separation, but boundary layer laminar	$3 \times 10^5 < Re < 3,5 \times 10^5$ Critical (Lower transition)
g)		B: Turbulent boundary layer separation; the boundary layer partly laminar partly turbulent	$3,5 \times 10^5 < Re < 1,5 \times 10^6$ Supercritical
h)		C: Boundary layer com- pletely turbulent at one side	$1,5 \times 10^6 < Re < 4 \times 10^6$ Upper transition
i)		C: Boundary layer com- pletely turbulent at two sides	$4 \times 10^6 < Re$ Transcritical

Figure 2.2: regimes of flow around a smooth, circular cylinder in steady current. Figure from Sumer and Fredsoe [5]

Strouhal Number St

The Strouhal number is based on the shedding frequency of a fixed cylinder in constant flow. It is proportionality constant between the vortex shedding frequency f_v and U/D . it's defined as:

$$St = \frac{f_v D}{U} \quad (2.2)$$

Strouhal number varies significantly for different Reynolds number ranges. As seen from Figure 2.3.

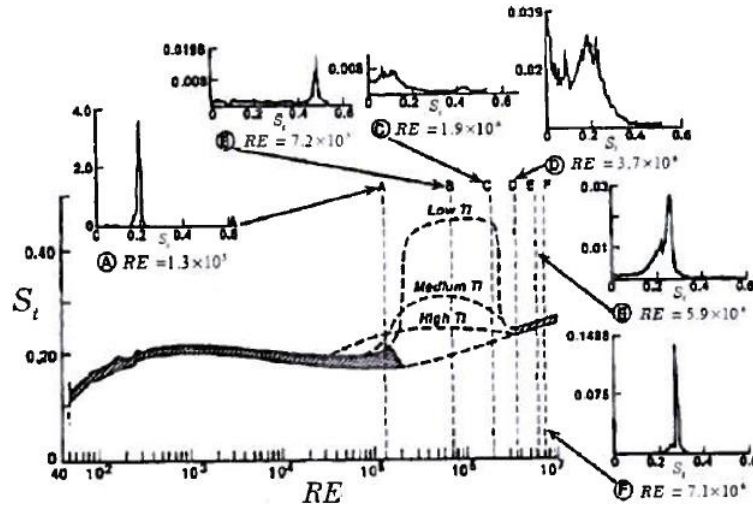


Figure 2.3: the dependence of St number on Re. Figure from Pantazopoulos [6]

Hydrodynamic Force Coefficient C_e and C_a

In VIVAVA, CF force and motion is band pass filtered around primary vortex shedding frequency component before calculating force coefficients. The filtered force in CF direction can be separated into one component in phase with the acceleration and the other component in phase with the velocity.

The excitation coefficient is expressed as

$$C_e = \frac{\frac{2}{T} \lim_{T \rightarrow \infty} \int F(t) \dot{y}(t) dt}{\frac{1}{2} \rho D L U^2 (\varpi y_0)} \quad (2.3)$$

The added mass coefficient is expressed as

$$C_a = \frac{\frac{2}{T} \lim_{T \rightarrow \infty} \int F(t) \ddot{y}(t) dt}{\frac{\pi}{4} \rho D^2 L (\varpi^2 y_0)^2} \quad (2.4)$$

Where, U is the flow velocity, L is the length and $F(t)$ is total hydrodynamic force on the cylinder. y_0 is the amplitude of the displacement. $\dot{y}(t)$ and $\ddot{y}(t)$ are the velocity and acceleration. ϖ is the angular frequency. D is the external diameter of the cylinder. T is the time of integer number or periods.

Non –Dimensional Frequency \hat{f}

The non-dimensional frequency is used as input parameters to select added mass and excitation coefficients in empirical models. which is defined by

$$\hat{f} = \frac{f_{osc} D}{U} \quad (2.5)$$

Where f_{osc} is the oscillation frequency.

Reduced Velocity V_{r0}

The reduced velocity is defined as the ratio between the path length in flow direction per cycle and the cylinder diameter:

$$V_{r0} = \frac{U}{f_0 D} \quad (2.6)$$

f_0 is the natural frequency in still water, which is usually used as parameter to present measurements from free oscillation tests.

If the oscillation frequency is used in still water, the reduced velocity is defined as

$$V_r = \frac{U}{f_{osc} D} = \frac{1}{\hat{f}} \quad (2.7)$$

2.2 Extracting Hydrodynamic Force coefficients

2.2.1 Rigid Pipe Tests with Harmonic Motion

At present, the most widely used CF coefficient database is based on the results from Gopalkrishnan's test [7]. In his test, a rigid cylinder was towed at constant speed and given a forced harmonic motion in CF direction only. Forces got from the cylinder ends were measured and force coefficients were computed- excitation coefficient C_e and added mass coefficient C_a . Force coefficients got from his original plots were presented as contour plots with non-dimensional frequency \hat{f} and amplitude ratio $\frac{A}{D}$ see Figure 2.4

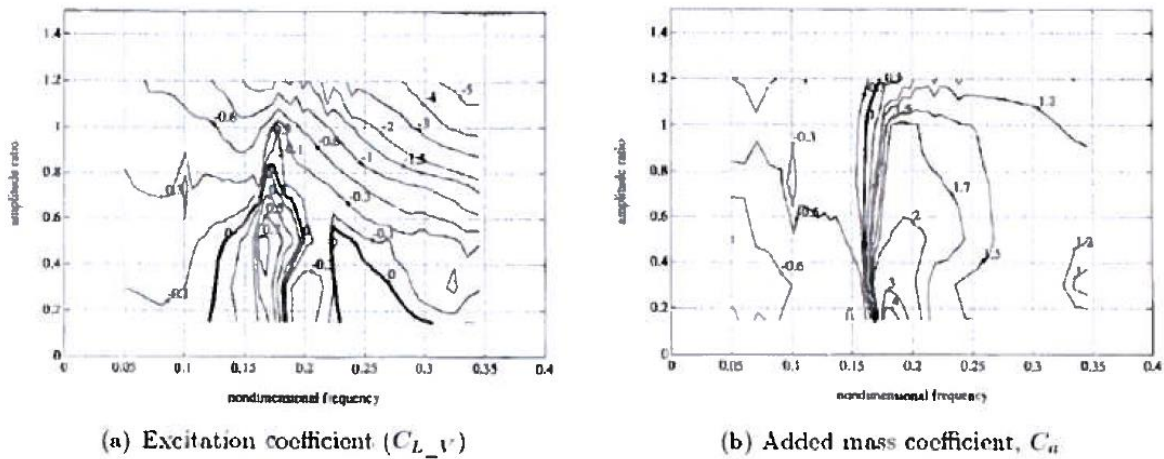


Figure 2.4: CF force coefficient database based on Gopalkrishnan's data. (a) excitation coefficient C_e ; (b) added mass C_a coefficient. Reynolds number is 10000.

There are Two excitation regions in the excitation coefficient contour plot which are given by the zero contour line in the plot. The first excitation region is between non-dimensional frequency $\hat{f}=0.125\sim 0.2$. The second excitation region is in the range of non-dimensional frequency $\hat{f}=0.22\sim 0.3$.

The contours of the added mass coefficients show an increase of the coefficients when the $\hat{f} = 0.16$ and the force coefficient jumps from negative values to positive values.

Measurements from field tests with long slender beam [8] show that VIV response is amplitude-modulated.

Because there are inherent limitation in the 2D rigid pipe experiments and existing database: Some differences between prediction of CF response and fatigue damage from empirical programs can be found [9].

Since the pipe is only able to vibrate at CF direction only, the fluid-structure interaction can be changed greatly when the pipe vibrates in both IL and CF direction. [10,11]

2.2.2 Rigid Pipe Tests with Observed Orbits

In order to get improved hydrodynamic force coefficient, we can use rigid cylinder experiment with obtained cross sectional orbits, see Fig 2.5. Non-dimensional frequency, amplitude, and Reynolds number were kept the same for both types of tests. The objective of this work is to obtain IL and CF hydrodynamic force coefficients at the primary vortex shedding frequency.

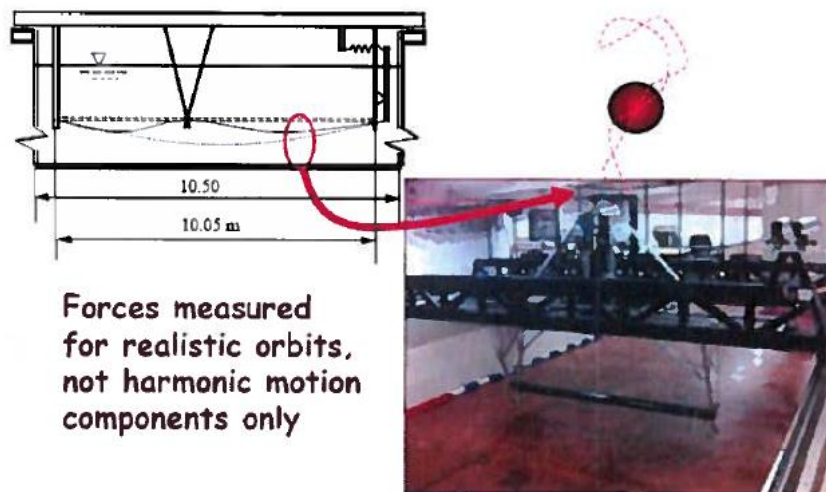


Figure 2.5: Trajectory taken from flexible beam experiment (left) is used as forced motion in the continuous rigid pipe test (right). Figure from Larsen [1]

This method needs a lot of experiments to produce enough data for force coefficient database. The amount of data is far less than what we need to cover all cases of practical interest. The work is continued by Yin [24] and Aglen [25].

Another alternative use of these results is to find the hydrodynamic force directly from the shape of the recent trajectory. This approach is described by Maincon [13].

2.3 Empirical Program VIVAVA

2.3.1 Experiment Environment (NDP Test)

The setup of the NDP test is given in figure 2.6:

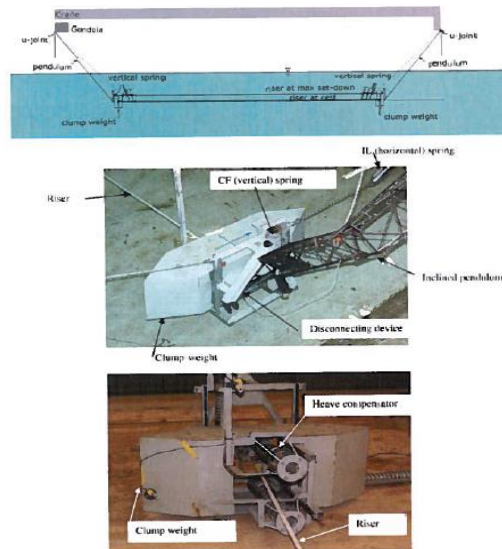


Figure 2.6: NDP high mode VIV test setup. Figure form Trim [18]

In NDP riser VIV tests, a 38 m horizontally towed cylinder was tested for VIV at different towing speeds in uniform flow and shear flow. The riser is made of a reinforced glass fiber pipe of 27 mm outer diameter, with a wall thickness of 3 mm. the mass ratio of the instrumented riser model is approximately 1.6. The key structural parameters are summarized in table 2.1

Table 2.1: Key Structural parameters of test pipe used in NDP experiment, taken form Trim [18]

Outer Diameter (D)	0.027	m
Wall thickness (t)	0.003	m
Length (L)	38	m
Section Modulus (EI)	598.8	Nm^2

We measure the bending strains at 24 locations along the riser in CF direction, and acceleration signals at 8 locations for both CF and IL direction, the test cases are seen in table 2.2. The eigen-frequencies are given in the test report. The stiffness of the pipe is tension controlled.

Table 2.2: Analyzed NDP high mode VIV test cases

Case No.	Max Current Speed (m/s)	Tension (N)
----------	-------------------------	-------------

2030	0.50 (uniform flow)	4000
2340	0.60 (shear flow)	4000

2.3.2 Experiment Environment (Rotating Rig Test)

The tests were performed with a rotating rig in MARINTEK's 10m deep towing tank. The test setup is shown in figure 2.7.

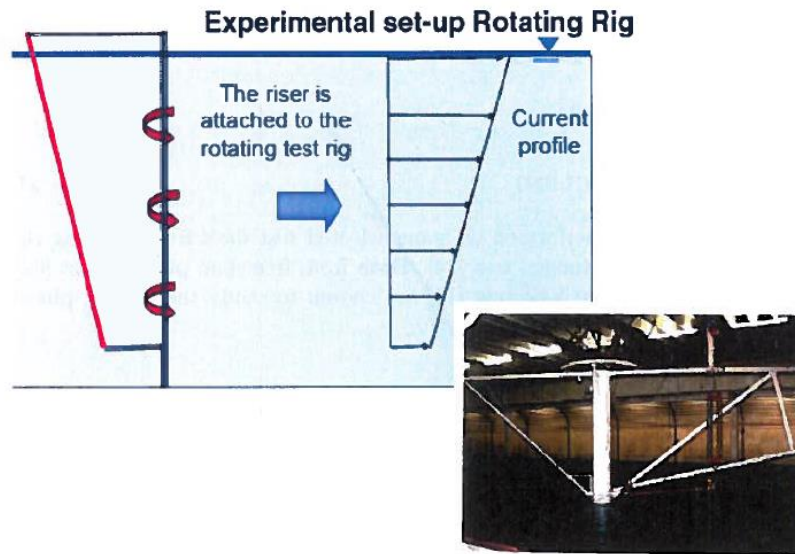


Figure 2.7: rotating rig test setup, figure from Barrholm [19]

The test rig was pinned at the floor of the tank. The upper end was attached to a force transducer. The slope of the riser can be adjusted so that it can be tested for different sheared/uniform flow profiles when the test rig rotates. The dimension of the riser is shown in table 2.3. 12 accelerometers were uniformly spaced along the riser to measure the response in cross-flow direction and 3 accelerometers were used to measure the in-line response. The sampling frequency was 200 Hz. The test case is summarized in table 2.4.

Table 2.3: Key Structural parameters of test pipe used in rotating rig test experiment, taken from Lie [20]

Outer Diameter (D)	0.02	m
Wall Thickness (t)	0.0046	m
Length (L)	11.34	m
Section Modulus (EI)	14.3	Nm^2

Table 2.4: Analyzed rotating rig VIV test case

Case No.	Current Speed at still water level (m/s)	Current Speed at bottom end (m/s)	Tension (N)
5205	0.16	0.61	725

By performing the rotating rig test, we can get the hydrodynamic force coefficients, see the excitation coefficients contour plot in figure 2.8

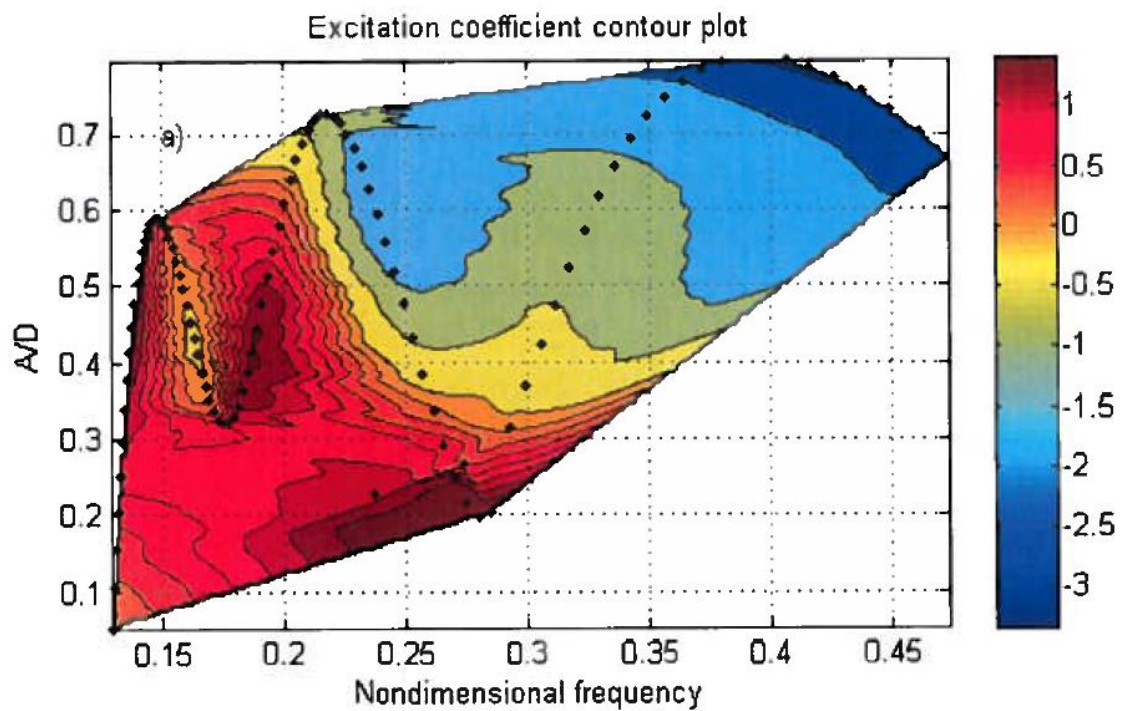


Figure 2.8: contour plot of excitation coefficients of non-dimensional amplitude and non-dimensional frequency (rotating rig test 5205) [21]

And the added mass coefficient contour plot in figure 2.9 [21]

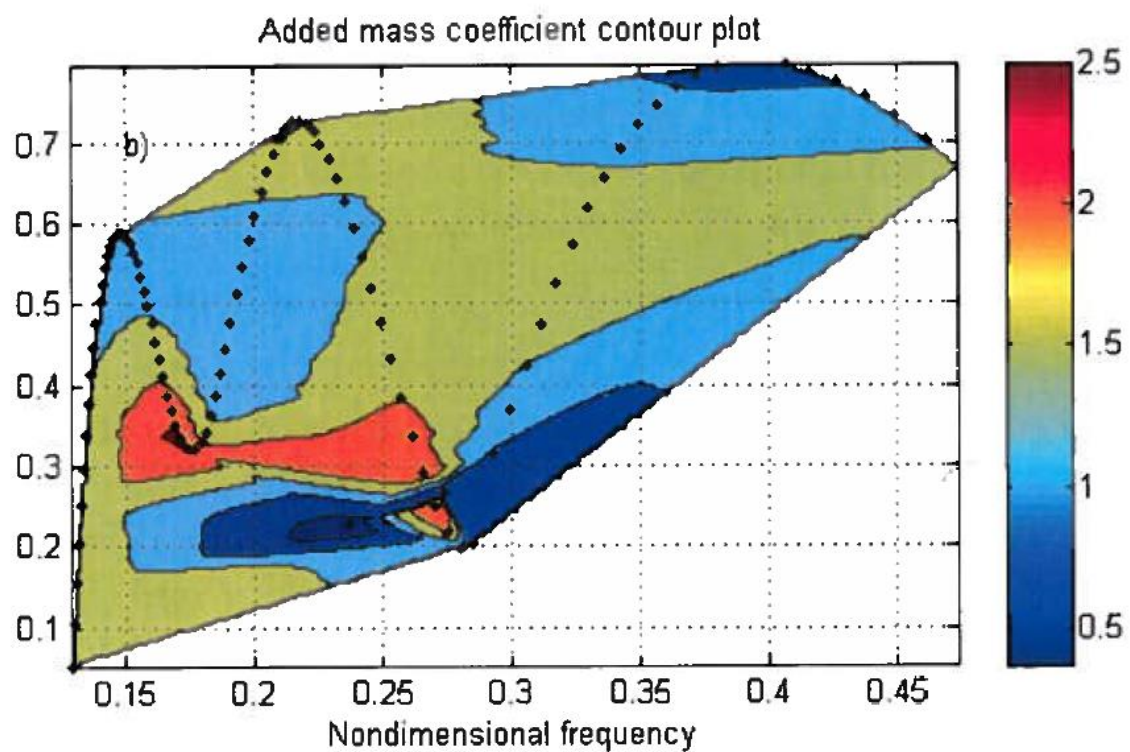


Figure 2.9: contour plot of added mass coefficients with non-dimensional amplitude and non-dimensional frequency (rotating rig test 5205) [21]

2.4 Empirical Program VIVAVA

2.4.1 Analysis Procedure

VIVAVA is a commercial software which can be used to predict VIV on slender marine structures which subject to current based on a semi-empirical approach. The hydrodynamic force along the riser is calculated from an empirical force coefficient database, which is in the form of several curves or functions that can provide coefficients when the local response parameters are known. The program is based on the assumption that the response takes place at one or more discrete eigen-frequencies.

2.4.2 Hydrodynamic Load Model

The empirical force coefficient database used in VIVANA is based on rigid pipe forced motion test results, which is done by Gopalkrishnan, see Fig 2.4

The CF added mass coefficient is approximated as response amplitude independently, as shown in Fig 2.10. Its value is found by taking the added mass values from Fig 2.4 at non-dimensional amplitude of 0.5.

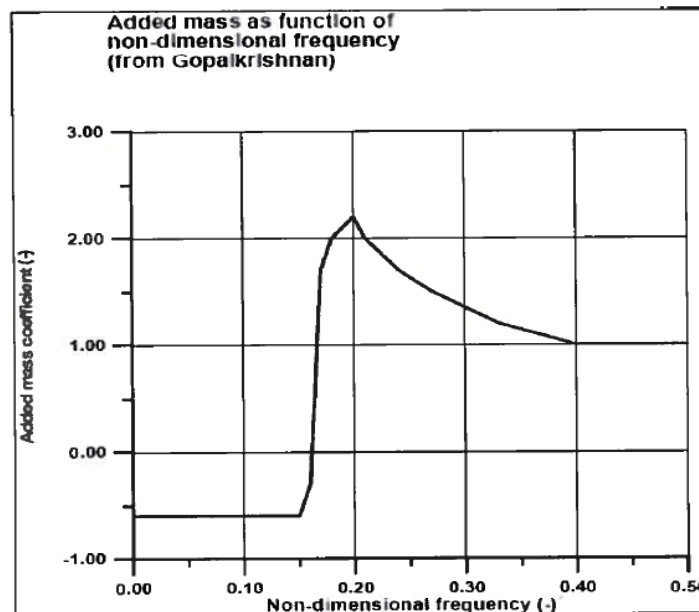


Figure 2.10: Added Mass curve in VIVANA. Figure from Larsen, [22]

In order to get the CF excitation force, VIVANA applies a set of parameters that defines the coefficient as a function of the amplitude. It simplifies the contour curves at a given non-dimensional frequency by second order polynomials. See figure 2.11. The curve is assumed to have a maximum value at point B, meaning that A-B and B-C can be given as two second order polynomial when the three points A, B and C are defined. The parameters are given as functions of the frequency.

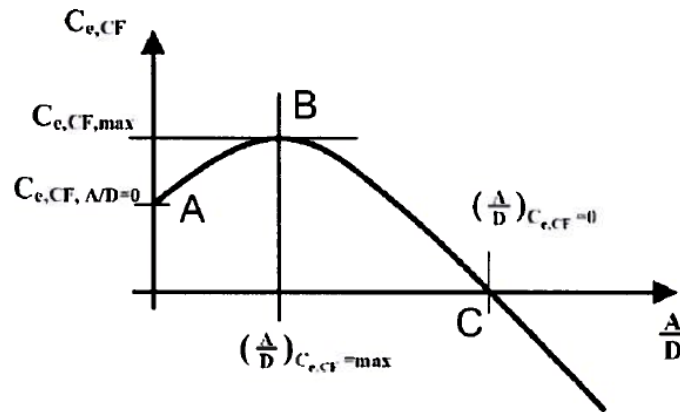


Figure 2.11: CF excitation coefficient curve defined from three points, figure from Larsen,[22]

The numerical values for A, B and C coordinates as functions of the non-dimensional frequency are defined in Fig 2.12 for cross-flow VIV. This figure makes it convenient to update the model with new information without changing the complete set of data as shown on Fig 2.4.

Detailed explanations can be found in the VIVANA theory manual [22].

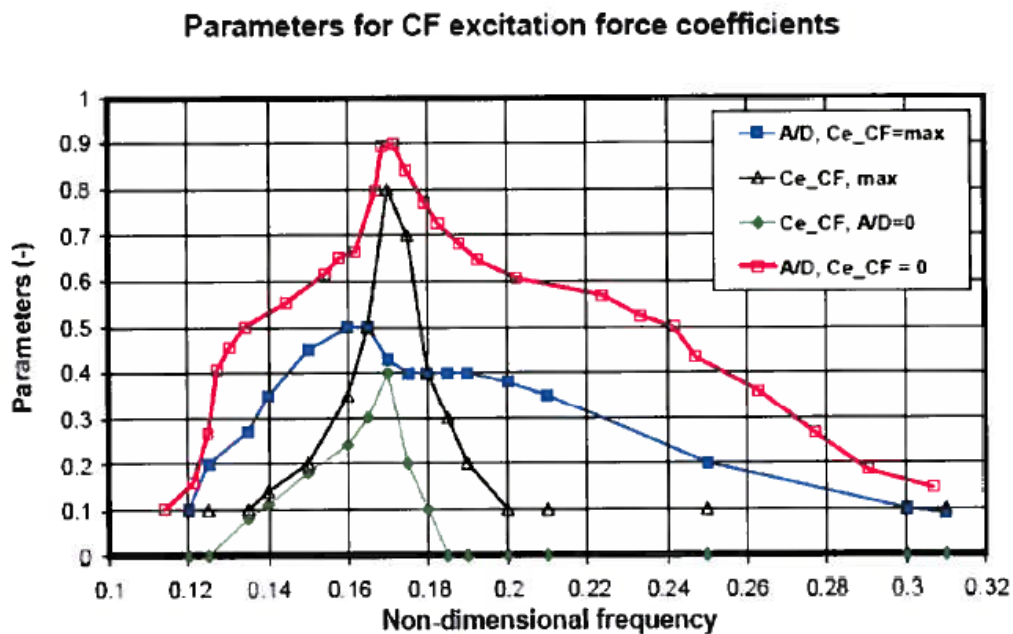


Figure 2.12: Parameters to define specific excitation coefficient curves for CF response analysis, figure from Larsen, [22]

Chapter 3

Force coefficient Identification by Inverse Analysis Method

3.1 Introduction

As we mentioned in chapter 2, direct measurement for the response of the riser is not realistic. It's only possible to measure the strain or acceleration at only a few points. The inverse analysis method is a method that can predict the response along the whole riser based on only a few measurements of the discrete points.

There are three ways to do the inverse analysis: the direct inverse analysis, the Kalman filter method and the optimal control theory method.

The direct method is to estimate displacement at unmeasured locations of the riser. The hydrodynamic forces can be calculated at more locations along the pipe than the measured locations. This method has large errors and not discussed in detail in the thesis.

The Kalman filter method is method is based on Karman filter. The filter models the system dynamics in a set of state equations. However, there is an unknown time delay between identified forces and response. This time delay may introduce error when calculating the force coefficients. As a result, this method is not discussed in detail in this report.

The third method is based on optimal control theory [14]. It is chosen over the frequency domain. The tension is kept constant in the present study. The rotation degrees of freedom are eliminated by master-slave condensation [15], which can improve the matrix number.

The acceleration and bending strain are measured at several locations along the flexible pipe during VIV test. Acceleration signals are measured at a number of locations along a flexible pipe during VIV test. And the acceleration signal can be transformed into displacement using double integration or modal. Bending strain signal also can be transformed to displacement before applied directly. The procedure is summarized in figure 3.1

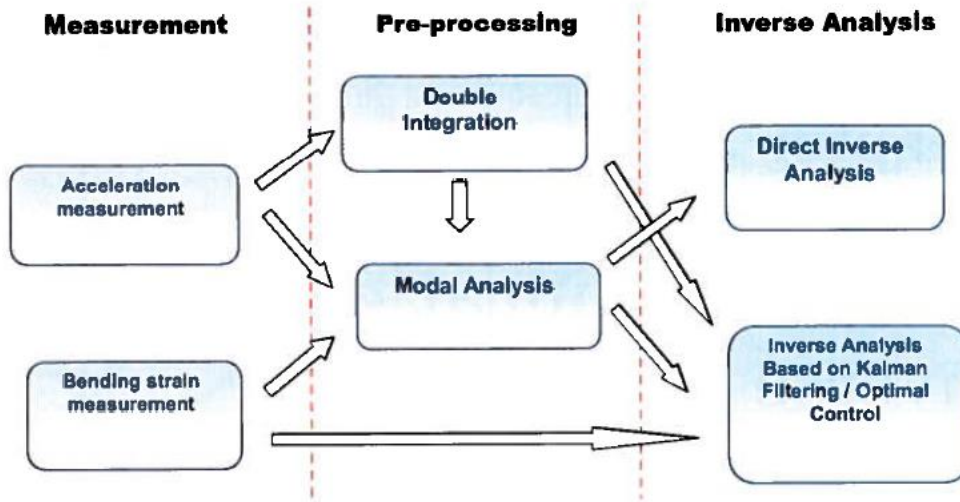


Figure 3.1: Inverse Analysis Procedure

3.2 Finite Element Beam Model

The beam is a tensioned Euler beam, shown by the following equation:

$$m \frac{\partial^2}{\partial t^2} y(z, t) - \frac{\partial}{\partial z} \left[T \frac{\partial}{\partial t} y(z, t) \right] + EI \frac{\partial^4}{\partial z^4} y(z, t) + c \frac{\partial}{\partial t} y(z, t) = F_{fluid}(z, t) \quad (3.1)$$

$y(z, t)$ is the beam deflection in CF direction, m is the mass of the beam per unit length without added mass, c is the structural damping characteristic, EI is the bending stiffness and T is the applied top tension. $F_{fluid}(z, t)$ is the total hydrodynamic forces, which is unknown.

The model is pinned at both ends and we does not consider axial displacements. The rotational degrees of freedom are eliminated by using maser-slave condensation. See Eq.(3.1).

$$M\ddot{Y}(t) + C\dot{Y}(t) + KY(t) = F(t) \quad (3.2)$$

M , C and K are the mass, damping and stiffness matrix respectively, Y is the CF displacement vector and F is the external hydrodynamic force vector. Rayleigh damping method has been used with C proportional to K .

The dynamic equilibrium equation of a finite element beam model defines in Eq. (3.2) can also transformed as the state-space model:

$$\dot{X}(t) = AX(t) + BF(t) \quad (3.3)$$

$$Z(t) = G^T X(t) \quad (3.4)$$

Where

$$X = \begin{bmatrix} Y \\ \dot{Y} \end{bmatrix} \quad (3.5)$$

$$A = \begin{bmatrix} 0 & I \\ -M^{-1}K & -M^{-1}C \end{bmatrix} \quad (3.6)$$

$$B = \begin{bmatrix} 0 \\ M^{-1} \end{bmatrix} \quad (3.7)$$

3.3 Pre-Processing Measurements

Direct measurements of riser displacements are not realistic. Accelerometer or strain gauges are normally used along the riser at limited locations to measure acceleration or strains signals, both accelerometer and strain gauges are used.

Acceleration signals measured at m locations along a flexible pipe during VIV test will be transformed to obtain displacement $Z = [z_1(t), z_2(t), \dots, z_m(t)]^T$ directly by double integration. The time varying shape of the riser can be composed as a series of mode shapes $\Phi = [\phi_1(t), \phi_2(t), \dots, \phi_m(t)]^T$. $\phi_i(t) = \sin(n\pi z/L)$.

$$\Phi \times w(t) = Z(t) \quad (3.8)$$

The model weight can be calculated by a least-square method.

$$w = (\Phi^T \Phi)^{-1} \Phi^T Z \quad (3.9)$$

The cylinder displacement at n locations $Y = [y_1(t), y_2(t), \dots, y_m(t)]^T$ is shown as :

$$Y(t) = \Phi \times w(t) \quad (3.10)$$

Another method to reconstruct the riser VIV response is expanding the displaced shape of the riser at any instance of time as a spatial Fourier series in both the sine and cosine terms [16].

Including additional cosine term may give more flexibility for the interpolating curve. Therefore, the travelling wave behavior can be better described.

3.4 Inverse Analysis Based on Optimal Control Theory

In order to identify a most probable external force F which creates response X close to the measured response Z , we minimize the cost function connected with the measurement error and external force and satisfying the dynamic equilibrium Eq.(3.3)

Cost Functions

Assuming that the measurement signal Z follows a Gaussian probability distribution about the true value Z_0 with a standard deviation σ_z . The cost connected to a difference between the true response Z_0 and the response Z is

$$j_z = \frac{1}{2}(Z_0 - Z)^T Q_{ZZ}(Z_0 - Z) \quad (3.11)$$

Where

$$Q_{ZZ} = \frac{1}{\sigma_z^2} I \quad (3.12)$$

The response vector Z_0 is related to state vector X by an observation matrix G :

$$Z_0(t) = G^T X(t) \quad (3.13)$$

Replace Eq 3.13 in Eq 3.11 and leave out the constant term associated with Z :

$$j_z = \frac{1}{2} X^T Q_{XX} X + Q_X X \quad (3.14)$$

Where

$$Q_{XX} = G^T Q_{ZZ} G \quad (3.15)$$

$$Q_X = -G^T Q_{ZZ} Z \quad (3.16)$$

The cost is:

$$j_F = \frac{1}{2} F^T Q_{FF} F \quad (3.17)$$

$$Q_{FF} = \frac{1}{\sigma_F^2} I \quad (3.18)$$

Where Q_{FF} includes the inverse of covariance of the force and σ_F the standard deviation of the error between estimated force and the true force

The total cost function is:

$$j = j_Z + j_F = \frac{1}{2} X^T Q_{XX} X + Q_X X + \frac{1}{2} F^T Q_{FF} F \quad (3.19)$$

Constrained Optimization

By minimizing a cost function of the response and the force under constraint, the external force is:

$$J = \int \left(\frac{1}{2} X^T Q_{XX} X + Q_X X + \frac{1}{2} F^T Q_{FF} F \right) dt \quad (3.20)$$

$\min_{X,F} J$, subjected to $\dot{X}(t) = AX(t) + BF(t)$

The system's dynamic equilibrium equation is:

$$X(k+1) = \Theta X(k) + \Gamma F(k) \quad (3.21)$$

The Lagrangian multiplier is:

$$J' = J - \sum_{k=0}^{n-1} \lambda^T(k+1) [X(k+1) - \Theta X(k) - \Gamma F(k)] \quad (3.22)$$

Taking the gradients of J' with respect to $X(k)$, $F(k)$ and $\lambda(k)$, the constrained optimization problem is solved by Franklin [23]. The external force F at time k is obtained by Eq. 3.23

$$F(k) = K_a(k)Z(k) + K_b(k) \quad (3.23)$$

For the last time step n

$$S(n) = Q_{XX}(n) \quad (3.24)$$

$$T(n) = Q_X(n) \quad (3.25)$$

The gains associated with response to $X(k)$ and external force $F(k)$ can be calculated backwards for time step k down from $n-1$ to 1 :

$$M_1(k) = \Theta^T(k)S(k+1)\Gamma(k) \quad (3.26)$$

$$M_2(k) = Q_{ZZ}(k) + \Theta^T(k)S(k+1)\Theta(k) \quad (3.27)$$

$$M_3^{-1}(k) = Q_{FF}(k) + \Gamma^T(k)S(k+1)\Gamma(k) \quad (3.28)$$

$$V_1(k) = \Theta^T(k)T(k+1) + Q_Z(k) \quad (3.29)$$

$$V_2(k) = \Gamma^T(k)T(k+1) \quad (3.30)$$

$$K_a(k) = -M_3(k)M_1^T(k+1) \quad (3.31)$$

$$K_b(k) = -M_3(k)M_2^T(k+1) \quad (3.32)$$

$$S(k) = M_1(k)K_a(k) + M_2 \quad (3.33)$$

$$T(k) = M_1(k)K_b(k) + V_1 \quad (3.34)$$

The gains $K_a(k)$ and $K_b(k)$ are calculated at each step k . The external force $F(k)$ is reconstructed by Eq 3.23. The response $X(k)$ is also obtained from Eq.3.21.

The major difficult is the poor conditioning of the matrix and it will cause stability problem and the computation time is too long. This limits the number of degrees of freedom that the method can calculate. Therefore, master-slave condensation is used to reduce rotation degree of freedoms [15], which also improves the numerical condition for inverting the matrix.

Regularization: Variance vs. Bias

The solution of the algorithm is influenced by the relative magnitude of Q_{ZZ} and Q_{FF} [17]: if Q_{ZZ} is high, then the estimated response from the algorithm will follow the measurement closely. On the other hand, if Q_{FF} is high, the solution of the algorithm will only be weakly related to the measured ones.

If the measurement data is adequate in precision, a range of ratio of Q_{ZZ} and Q_{FF} may exist. The solution does not change too much over this range.

Chapter 4

Application of Inverse Analysis on Flexible Beam VIV Experiments

4.1 Inverse Analysis for NDP Test of Sheared Current Flow

4.1.1 NDP Shear flow Case 2340

This case is a shear current case, the left end of the riser is with 0 current velocity, while the right end of the riser is with current velocity 0.6 m/s. see figure 4.1:

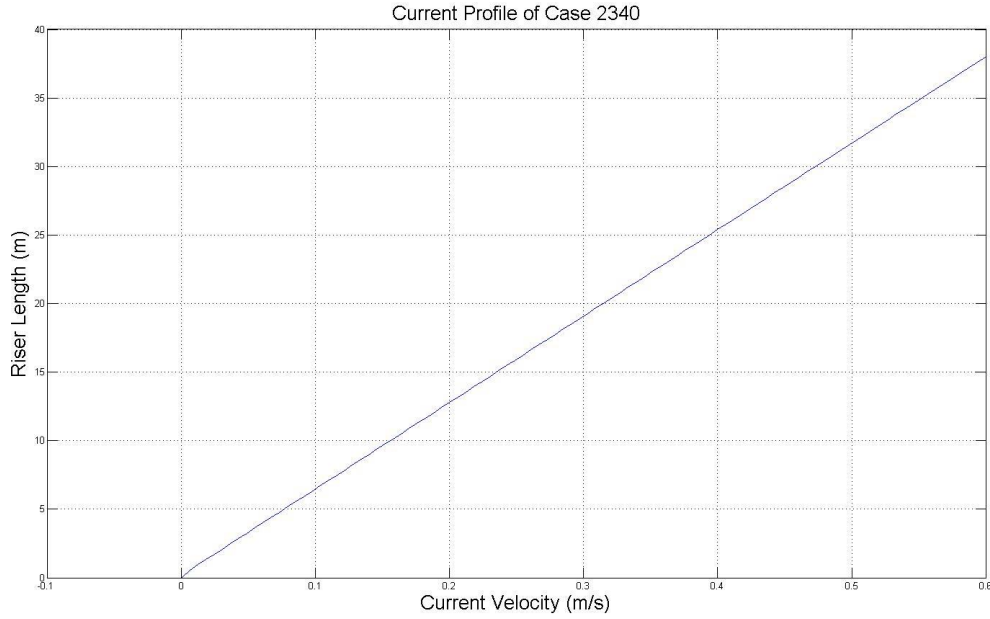


Figure 4.1: current velocity of NDP test case2340

In the test, we measure the bending strains at 24 locations along the riser in CF direction only, and the acceleration signals at 8 locations for both CF and IL direction. The strains and accelerations are transformed into displacements using Normal Mode Analysis method.

Then, we selected only 19 points along the riser and use their displacements as input of the inverse analysis calculation.

Before we carry on the inverse analysis we first have to decide the weighting factor in the cost function, see functions below:

$$j = j_Z + j_F = \frac{1}{2} X^T Q_{XX} X + Q_X X + \frac{1}{2} F^T Q_{FF} F \quad (4.1)$$

$$Q_{XX} = G^T Q_{ZZ} G \quad (4.2)$$

$$Q_X = -G^T Q_{ZZ} Z \quad (4.3)$$

We use the sensitivity of weighting parameter to control the weighting of the costs of the measured displacement and the force. The higher parameter is, the higher Q_{ZZ} we have, which means that the closer the calculated displacement data we get compared with the data from experiments.

4.1.2 Results of Different Sensitivity of Weighting Parameters

In order to find the influence of different parameters on the displacements, we select five different parameters to make a comparison:

We choose Parameter= 6, 7,8,9,10,15 separately.

From the tests, we can find that the displacements of the inverse analysis highly depend on the parameter. We select the midpoint of the riser and plot the displacement of the midpoint with time. See figure 4.2:

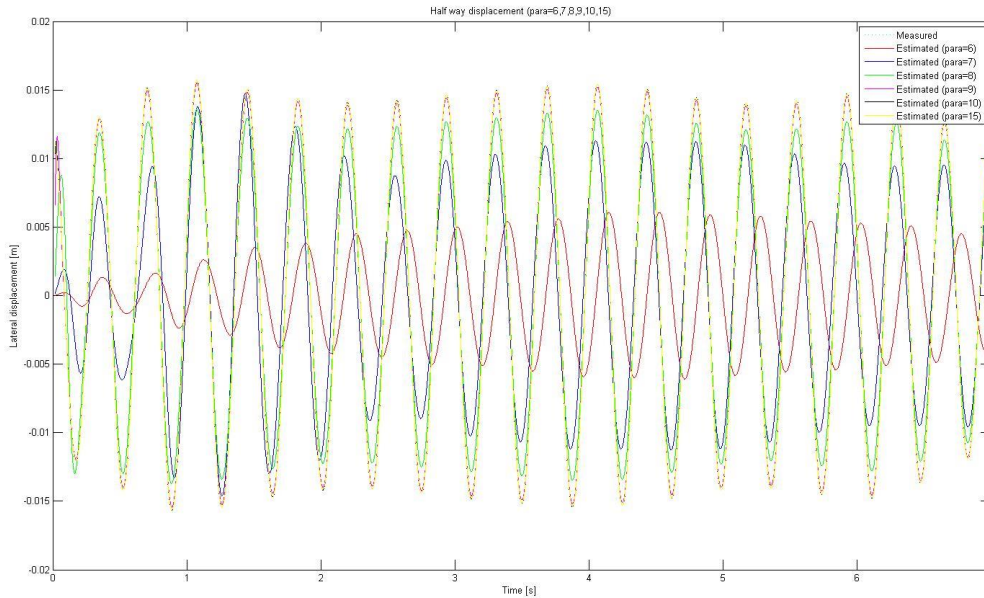


Figure 4.2: midpoint displacements of the riser for parameter=6, 7,8,9,10,15 and displacement measured

We can see from the figure, the higher parameter we use, the closer the displacement from inverse analysis to the displacement we got from experiments, which means with the increasing of parameter, the contribution of the force is increasing, which ‘forced’ the riser to behave exactly as it did in the experiment, normally it will make the force larger than true value.

Next, we can identify excitation coefficients and added mass coefficients for different parameters, using equation 4.4 and 4.5:

$$C_e = \frac{\frac{2}{T} \lim_{T \rightarrow \infty} \int F(t) \dot{y}(t) dt}{\frac{1}{2} \rho D L U^2 (\varpi y_0)} \quad (4.4)$$

$$C_a = \frac{\frac{2}{T} \lim_{T \rightarrow \infty} \int F(t) \ddot{y}(t) dt}{\frac{\pi}{4} \rho D^2 L (\varpi^2 y_0)^2} \quad (4.5)$$

We can get the excitation coefficient C_e and added mass coefficients C_a for these 19 points, plot them with riser length, see figure 4.3:

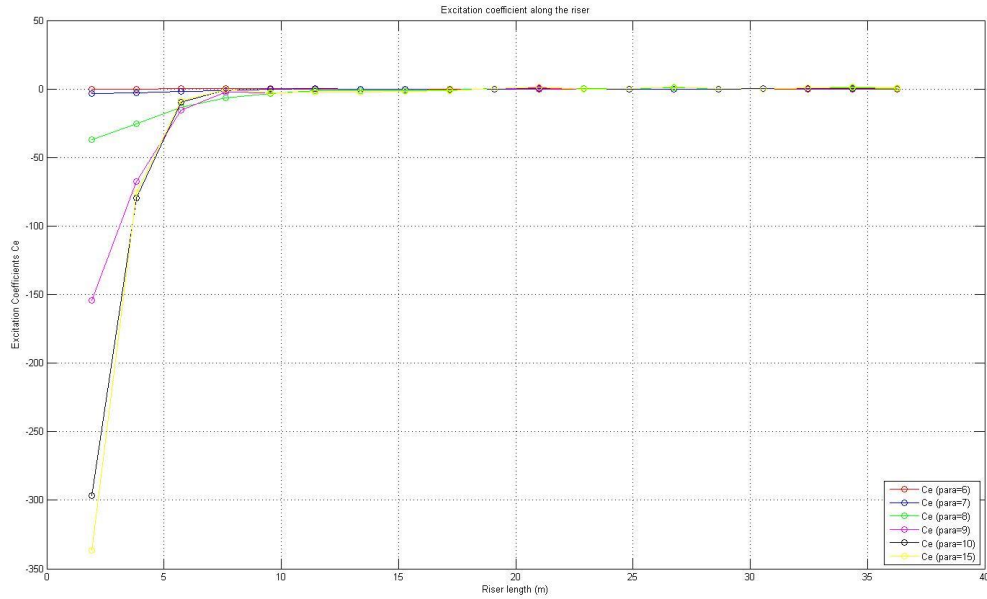


Figure 4.3: excitation coefficients along the riser for parameter=6, 7,8,9,10,15

We can see that when close to the left endpoint of the riser, the excitation coefficient is very unstable, that's basically because the velocity of the vibration close the left endpoint is very small (close to zero), even a small disturbance will cause large difference to the result.

To see the detail of the C_e for different parameter long the riser, we select the data from the riser length 15m to 38m in order to get rid of the influence of the small velocity, see figure 4.4:

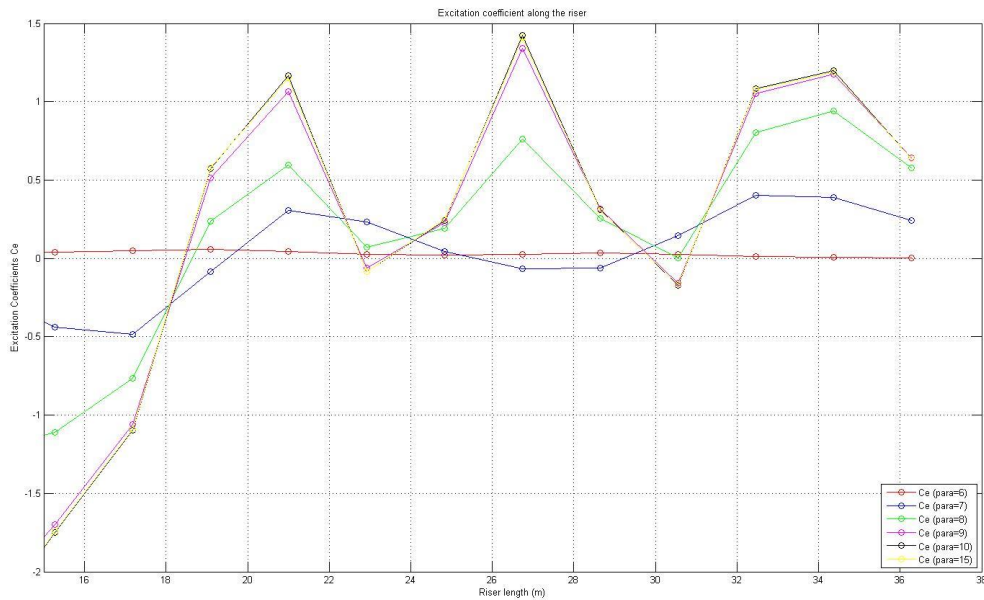


Figure 4.4: excitation coefficients along the riser (from 15m to 38m) for parameter=6, 7,8,9,10,15

And we can see with the increasing of the parameter, the excitation coefficient is also increased, this is because that as we discussed above, when increase the parameter, and the

estimated response from the inverse analysis will tend to follow the measurement closely. This may lead to the structure into the noisy measurements. And for parameter=6 and parameter=7, the excitation coefficients are quite small and unstable, which is not a good estimate, and for parameter=8, the estimated parameter have large difference compared with parameter=9, this is not a good estimate as well. While parameter=10, it has little difference with parameter=15, which means the coefficient is quite stable.

Similarly, we check the added mass coefficient, see figure 4.5:

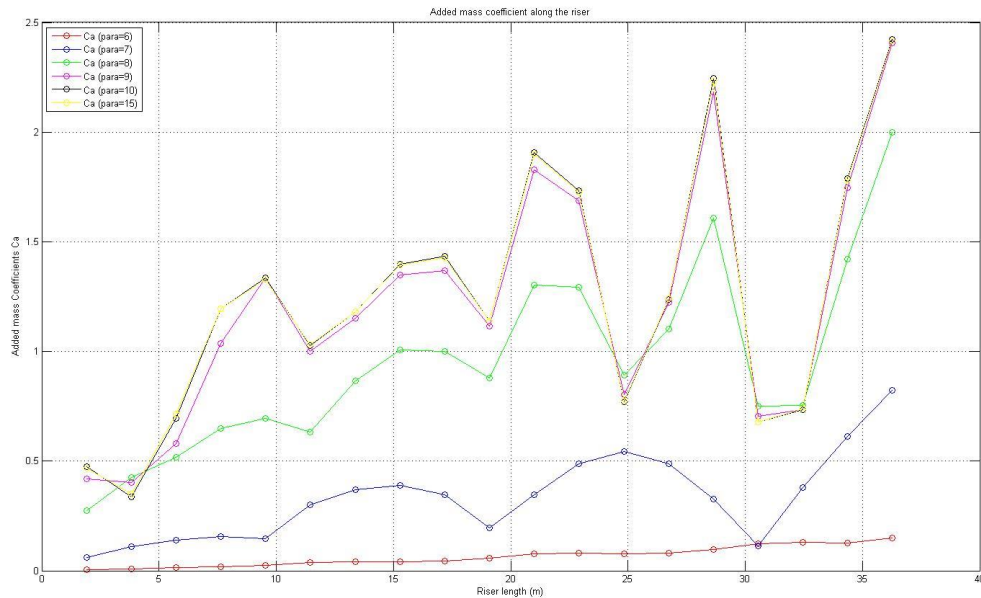


Figure 4.5: excitation coefficients along the riser for parameter=6, 7,8,9,10,15

We can find it has the same trend with the excitation coefficient. When we increase parameter, the added mass coefficient is also increased and the amplitude of Ca close to the right side is large is mainly because that the acceleration of the riser is close to zero, which means that it's easy to be affected by very small change. And when parameter=6, 7 and 8, the added mass coefficient are not small and unstable. While parameter=10 is better.

Next we will see the relationship of the force got from inverse analysis at the midpoint of the riser with time, see figure 4.6:

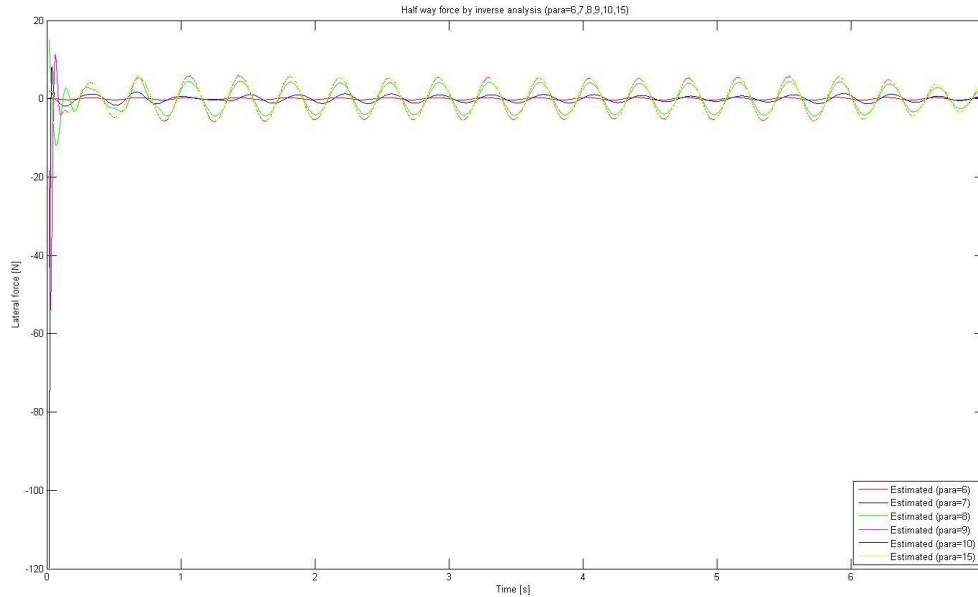


Figure 4.6: lateral force from inverse analysis for the midpoint of the riser with parameter=6, 7,8,9,10,15

We can see that at the beginning of the time interval, because the towing is just started, the velocity is quite small, which means that the towing force is very unstable and will give unrealistic values. We chose from time interval 0.4s to 7s to get rid of the large uncertainty. See the figure 4.7:

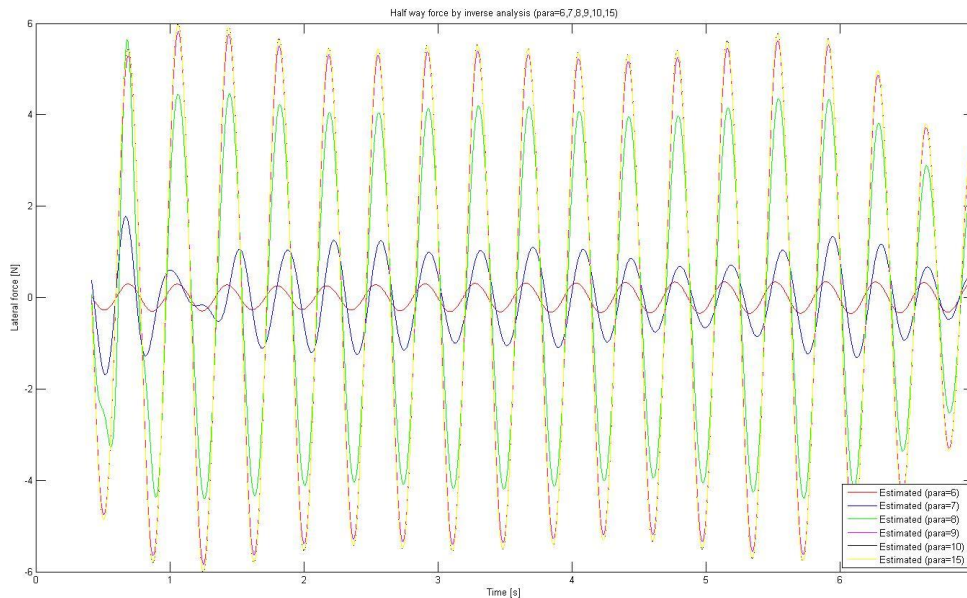


Figure 4.7: lateral force from inverse analysis for the midpoint of the riser with parameter=6, 7,8,9,10,15 from time 0.4s to 7s

We can see it clearly, as we expected, the force estimated by inverse analysis for small parameter is also smaller than the force estimated by large parameter as has already been explained. For parameter=6, 7, 8, the force estimated are also unrealistically small and unstable. For parameter=10, the force we estimated is quite stable.

In conclusion, we assume parameter=10 is the most correct value.

4.2.3 Calculation of Excitation and Added Mass Coefficients along the Riser

In the shear flow analysis, we can plot the relationship between excitation coefficient C_e and non-dimensional amplitude A/D , since we choose parameter=10 as the most correct one. We can divide the riser into more elements, to make the plot smoother in order to see the detail to the excitation parameter along the riser. Here we choose 90 points along the riser. See figure 4.8:

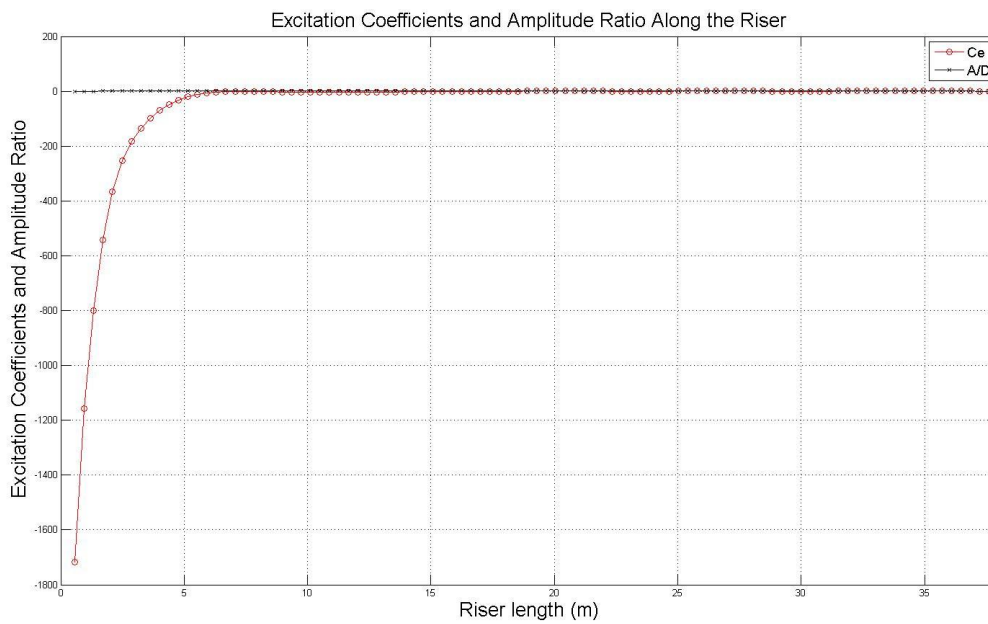


Figure 4.8: excitation coefficients and non-dimensional amplitude along the riser for parameter=10

Zoom in detail from riser length 15m to 38m, see figure 4.9:

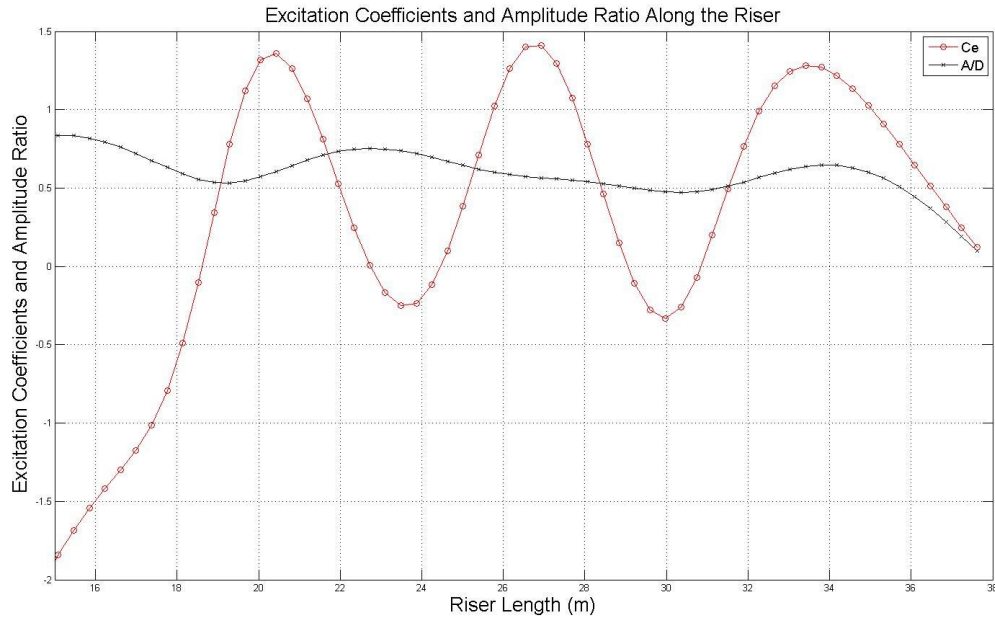


Figure 4.9: excitation coefficients and non-dimensional amplitude along the riser for parameter=10 from 15m to 38m

4.2.4 Contour Plot of Excitation and Added Mass Coefficients

Then we can get the contour plot of the excitation coefficient with A/D and non-dimensional frequency \hat{f} . As we have 90 points, the contour plot is quite smooth. In order to get rid of the unstable points of C_e near the left end side of the riser, we just use the last 80 points. See figure 4.10 below, the black dots in the figure represents the estimated force coefficients from inverse analysis. The contours are interpolated from the data points. The contours have limited accuracy due to the large variation of data density and they are also incomplete since the data points cannot cover the whole amplitude ratio and non-dimensional frequency space.

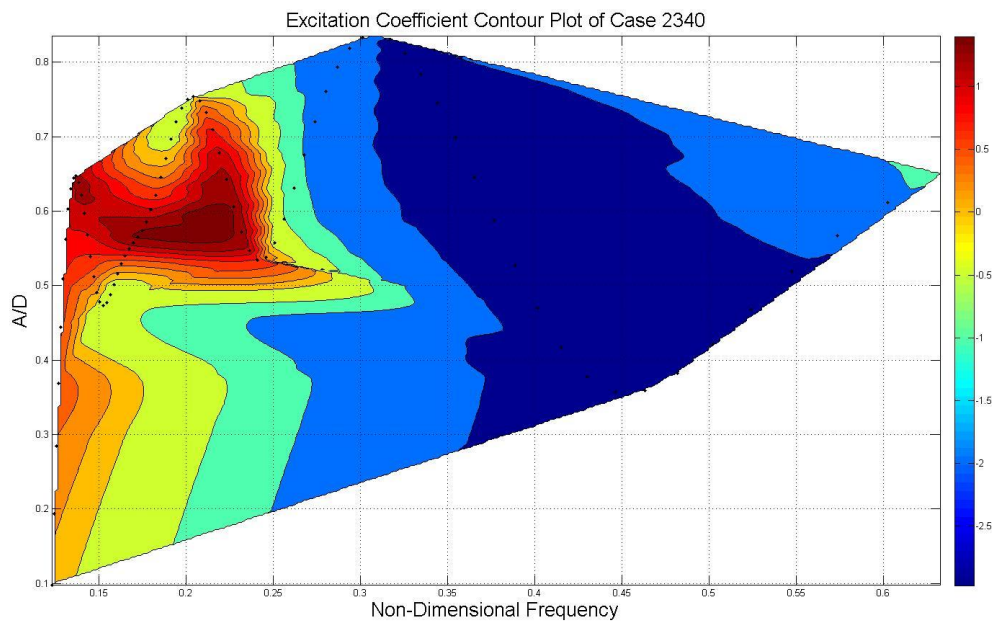


Figure 4.10: contour plot of excitation coefficients of non-dimensional amplitude and non-dimensional frequency, parameter=10

Compare the result with the inverse analysis results for rotating rig test 5205 [21], see figure 2.8 in chapter 2. We can see that for the NDP high mode test, there are two excitation ranges. The first excitation region is from $\hat{f}=0.12$ to 0.16 and the second one is from $\hat{f}=0.17$ to 0.31 . There is a valley with negative excitation coefficient around $\hat{f}=0.16$. When $\hat{f}=0.13$ there is a peak value excitation coefficient of about 1.0 is observed with amplitude ratio of about 0.62. When $\hat{f}=0.2$ there is another peak value about 1.5 with the maximum amplitude ratio of about 0.6.

While for the rotating rig test, we see that there are two excitation regions. The first region ranges from non-dimensional frequency $\hat{f}=0.12$ to $\hat{f}=0.22$. There is a valley as well with negative excitation around $\hat{f}=0.16$. Significantly high excitation coefficient with a value of 1.4 is observed at $\hat{f}=0.14$ with amplitude ratio of 0.5. The highest positive excitation coefficient is 1.5 at $\hat{f}=0.19$ and the corresponding amplitude ratio is around 0.45. The second excitation region seems to range from $\hat{f}=0.25$ to $\hat{f}=0.31$. The largest excitation coefficient value at $\hat{f}=0.28$ is considered less accurate due to small response amplitude.

Using the same method, we can plot the added mass coefficient with A/D along the riser, see figure 4.11 below:

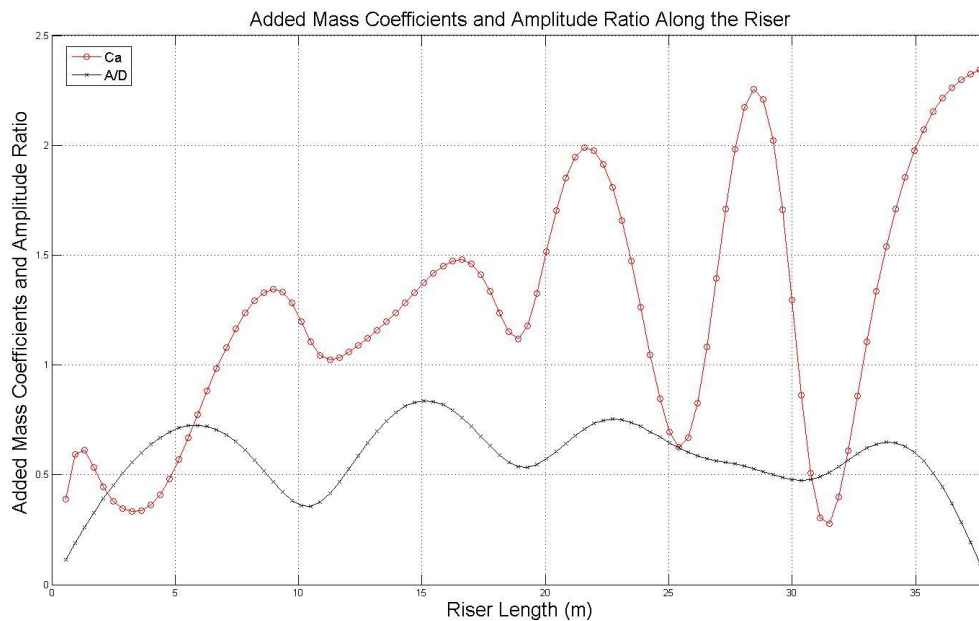


Figure 4.11: added mass coefficients and non-dimensional amplitude along the riser for parameter=10

Make the contour plot of added mass coefficient, see figure 4.12:

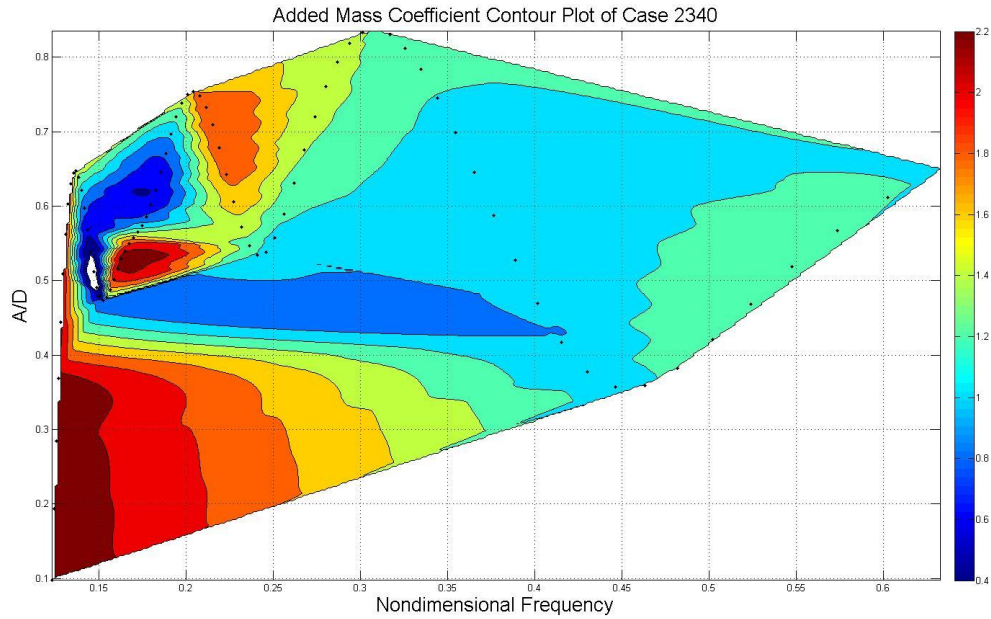


Figure 4.12: contour plot of added mass coefficients with non-dimensional amplitude and non-dimensional frequency, parameter=10

Compare the result with the results from rotating rig test 5205, see figure 2.9 in chapter 2. We see that for the NDP high mode test 2340, the added mass coefficients for $A/D < 0.4$ is very large, which is unrealistic, and this is basically because of the small amplitude of acceleration when A/D is small, since C_a is high for small displacement amplitude and with small amplitude, there is large uncertainty as well. As a result, we neglected the data for $A/D < 0.4$. Then we can see that when $\hat{f} = 0.17$, there is a peak value of C_a about 2.2 with non-dimensional amplitude 0.52. the value of C_a fits quite well with the result of rotating rig test, while the non-dimensional amplitude is different, because for the rotating rig test, the peak value of C_a will happen when $A/D = 0.4$. But the trend seems similar.

See from the results, even for the different experiments, the contour plot we get show similar trends. Which means when we consider the CF direction response only, we can use the non-dimensional frequency \hat{f} and non-dimensional amplitude A/D as a function of excitation and added mass coefficients. And the inverse analysis method seems to give quite reasonable results.

4.2 Inverse Analysis for NDP High Mode Tests of Uniform Current Flow

4.2.1 NDP High Mode Test 2030

This case is a uniform current case, the current velocity along the riser is constant, 0.5m/s. see figure 4.13:

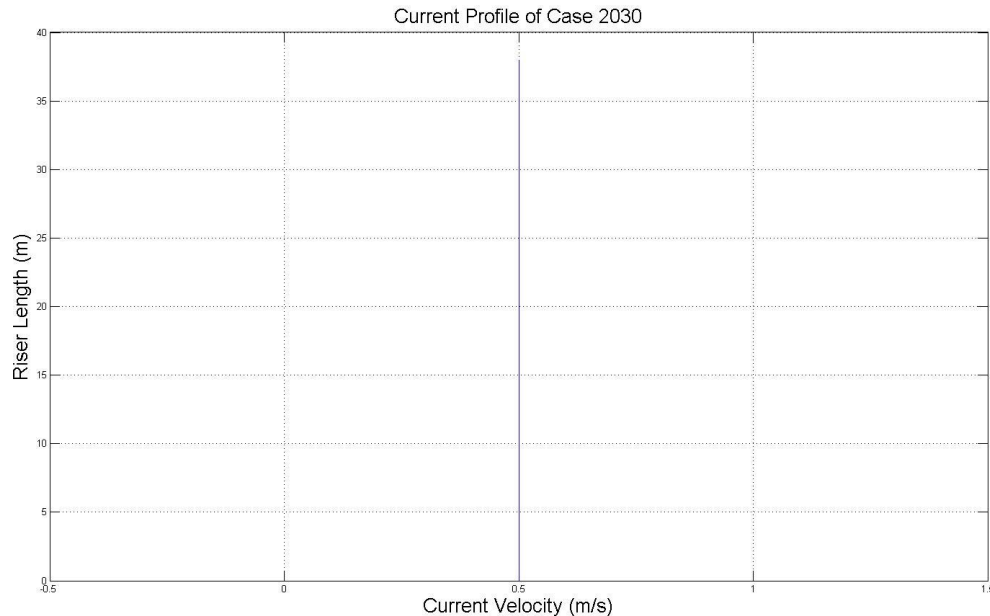


Figure 4.13: current velocity of the Test 2030

Then, we selected 19 points along the riser and take their displacement as input of the inverse analysis.

4.2.2 Results of Different weighting parameters

Before we carry out the inverse analysis we first have to decide the weighting factor in the cost function, we use the similar with mode test 2340. We select five different parameters:

Parameter= 6, 7,8,9,10,15 separately.

We find the same trend for test 2030. We select the midpoint of the riser and plot the displacement of the point with time. Compare the displacement of different parameters with the value from the measurement. See figure 4.14 below:

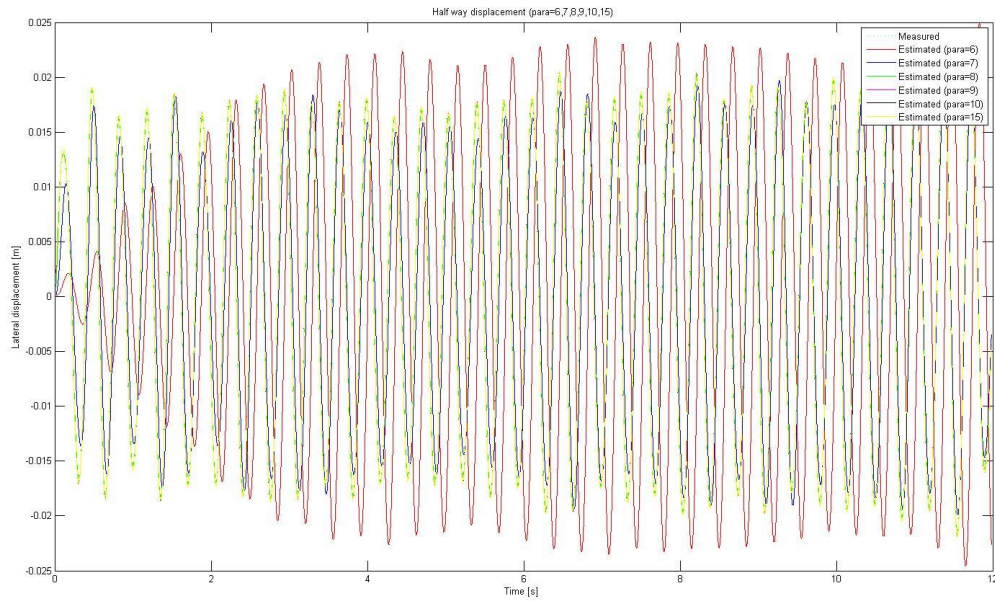


Figure 4.14: midpoint displacements of the riser for parameter=6, 7,8,9,10,15 and displacement measured of NDP test 2030

As we can see from the results, there are similar results with NDP test 2345, but there are difference when parameter is small (parameter=6), the displacement estimated by inverse analysis is larger than the experiment value. Basically speaking, the larger the parameter is, the closer the displacement by inverse analysis to the displacement measured.

Next, identify excitation coefficients and added mass coefficients for different parameter, see figure 4.15:

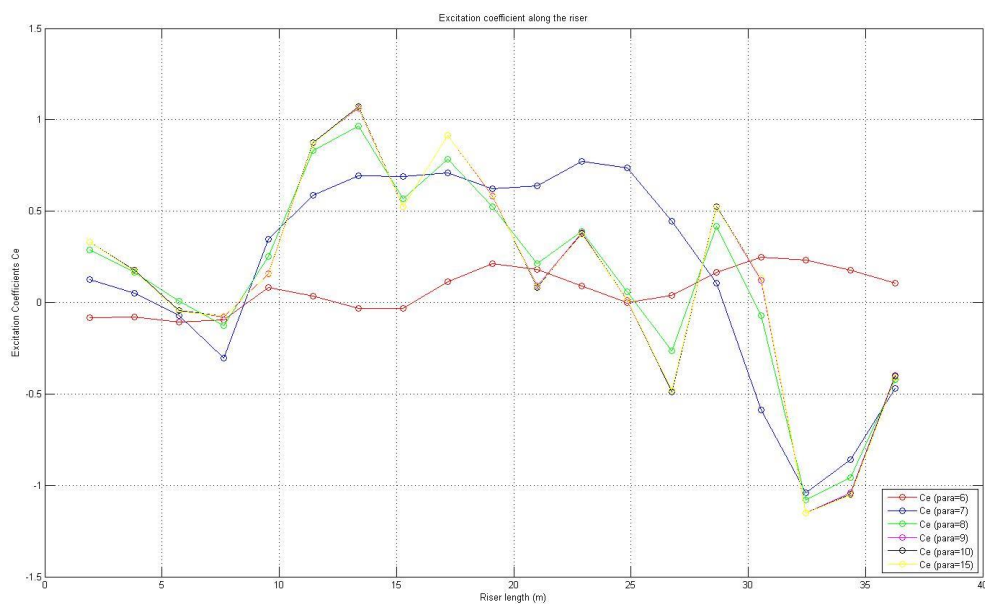


Figure 4.15: excitation coefficients along the riser for parameter=6, 7,8,9,10,15

We can find that when parameter is smaller than 8, the plot is very unstable, which means the C_e varies very much with parameter. The same phenomenon can be found from the C_a plot. See figure 4.16:

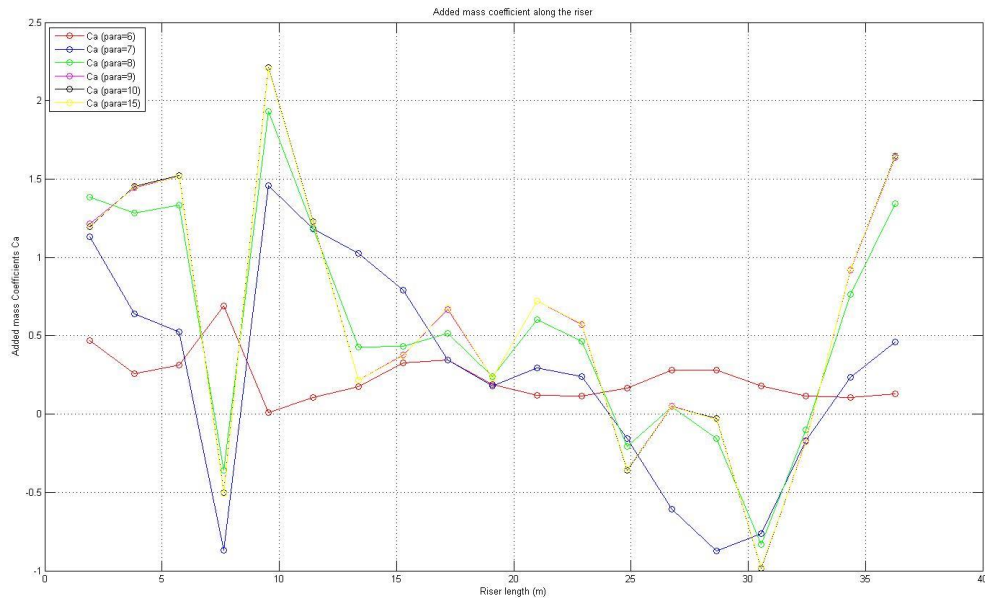


Figure 4.16: added mass coefficients along the riser for parameter=6, 7, 8, 9, 10, 15

Then we will see the relationship of the force got from inverse analysis at the midpoint of the riser with time, see figure 4.17:

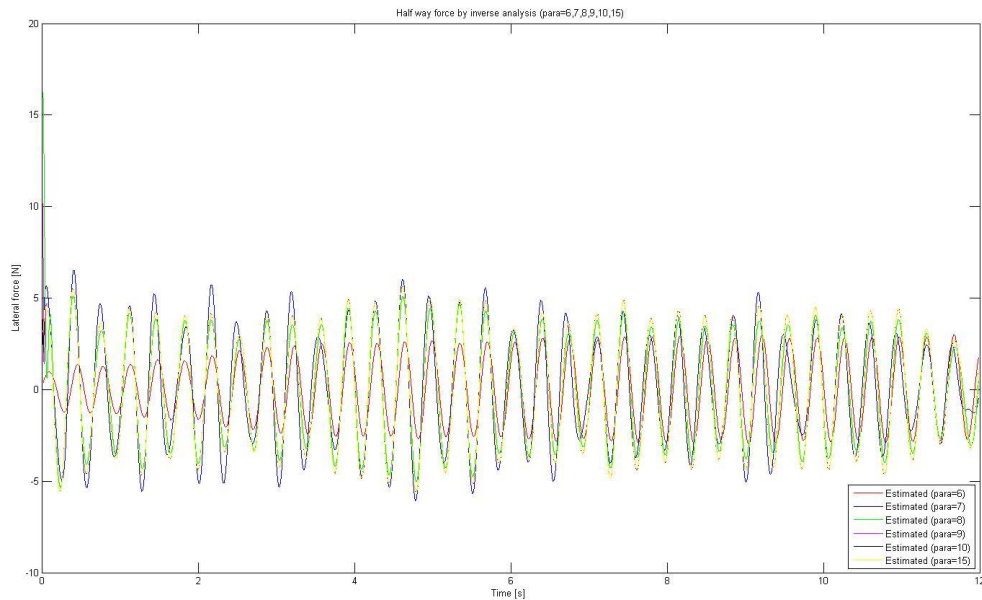


Figure 4.17: lateral force from inverse analysis for the midpoint of the riser with parameter=6, 7, 8, 9, 10, 15

We can see that at the beginning of the time interval, the force is very unstable, then we select from the 0.4 time as starting point, see the figure 4.18:

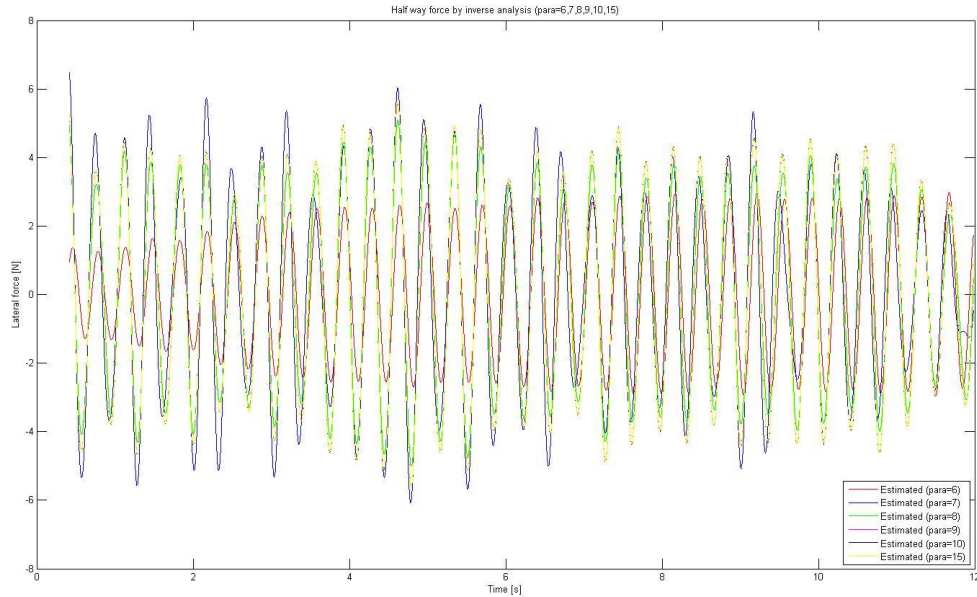


Figure 4.18: lateral force from inverse analysis for the midpoint of the riser with parameter=6, 7,8,9,10,15 between 0.4s and 12s

We can see it clearly, as we estimated, the force by small parameter is smaller than the force by large parameter. But this is not always correct, because when parameter=7, the force estimated is sometimes large than parameter=15. In conclusion, we assume parameter=10 is the most correct one.

4.2.3 Calculation of Excitation and Added Mass Coefficients along the Riser

In the uniform flow analysis, we can plot the relationship between excitation coefficient C_e and non-dimensional amplitude A/D , since we choose parameter=10 as the most correct one. Then we can divide the riser into more elements, to make the plot smoother. See figure 4.19 below:

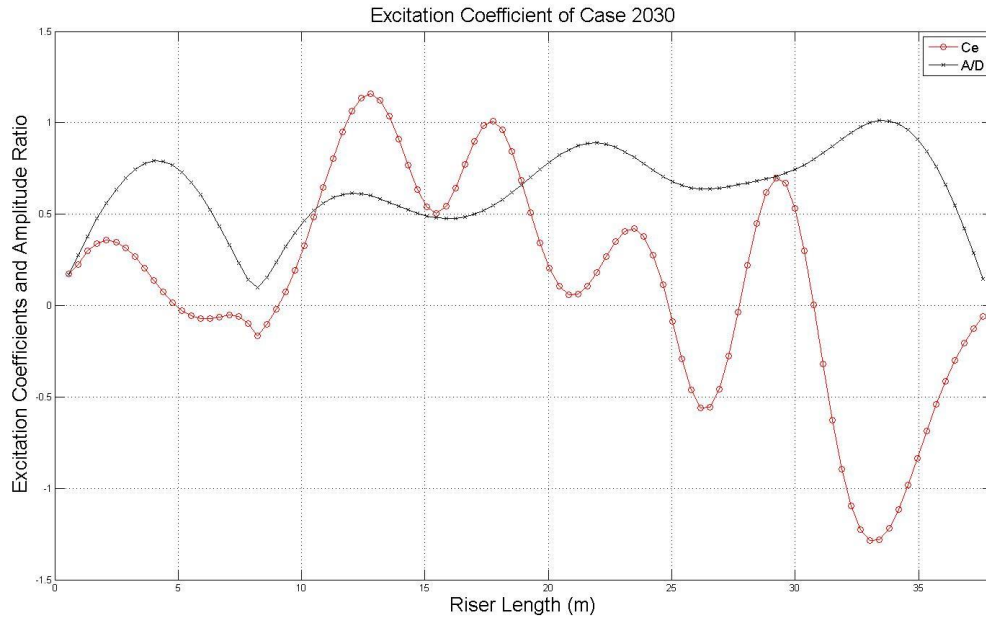


Figure 4.19: excitation coefficient and non-dimensional amplitude along the riser length

If we use A/D as x-axis and Ce as y-axis, we can see figure 4.20:

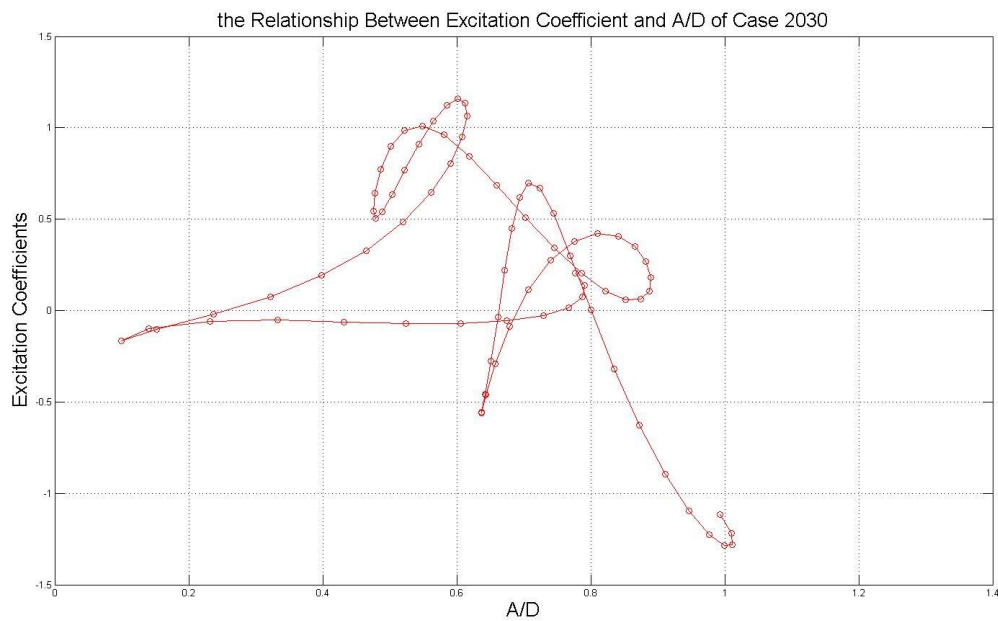


Figure 4.20: relationship between excitation and non-dimensional amplitude

When A/D is small, there will be large uncertainty with Ce, as a result, we neglect the points when A/D is smaller than 0.2, plot, see figure 4.21:

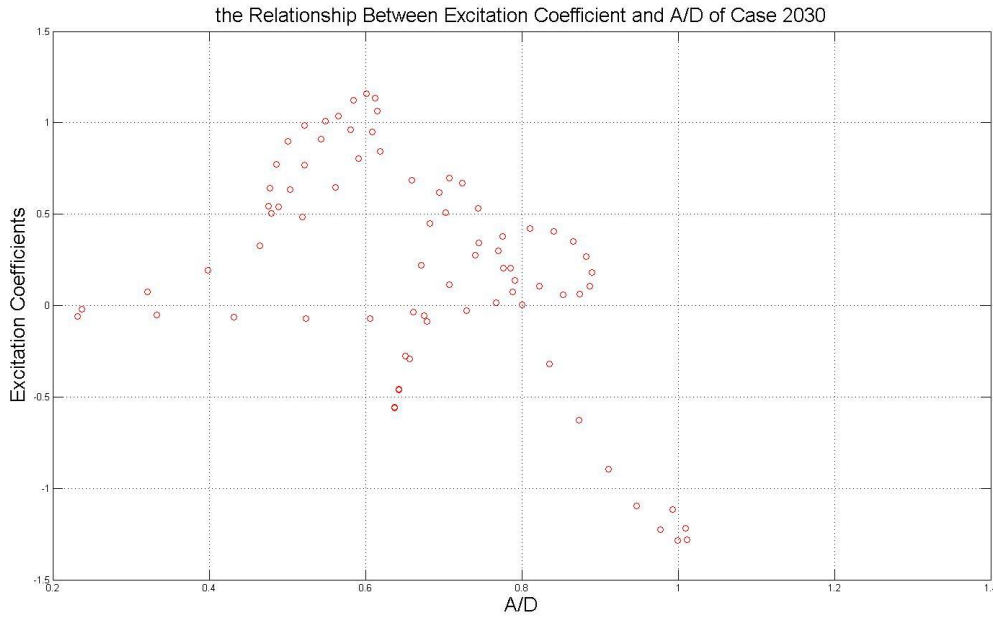


Figure 4.21: relationship between excitation and non-dimensional amplitude for $A/D > 0.2$

This figure does not fit very well with the three point figure, see figure 4.22:

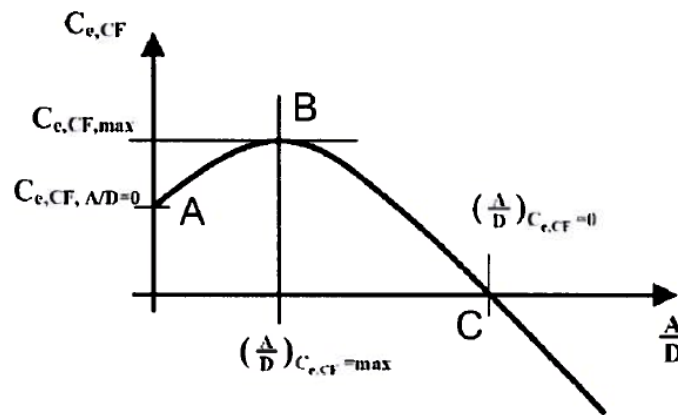


Figure 4.22: CF excitation coefficient curve defined from three points, figure from Larsen,[22]

Figure 4.22 is the built-in model in VIVAVA, it applies a set of parameters that defines the coefficient as a function of the amplitude. It simplifies the contour curves at a given non-dimensional frequency by second order polynomials. The curve is assumed to have a maximum value (horizontal tangent) at B, meaning that AB and BC can be given as two second order polynomial when the three points A, B and C are defined. This figure does not fit very well with the three point figure, this must be the effect of interaction between in-line vibration and cross-flow vibration, the phase angle between CF and IL vibration. During this analysis, we just focus on the CF response and neglect the IL response. As a result, the phase angle will take effect.

Then we plot the figure of added mass coefficient and non-dimensional amplitude along the riser, see figure 4. 23 below:

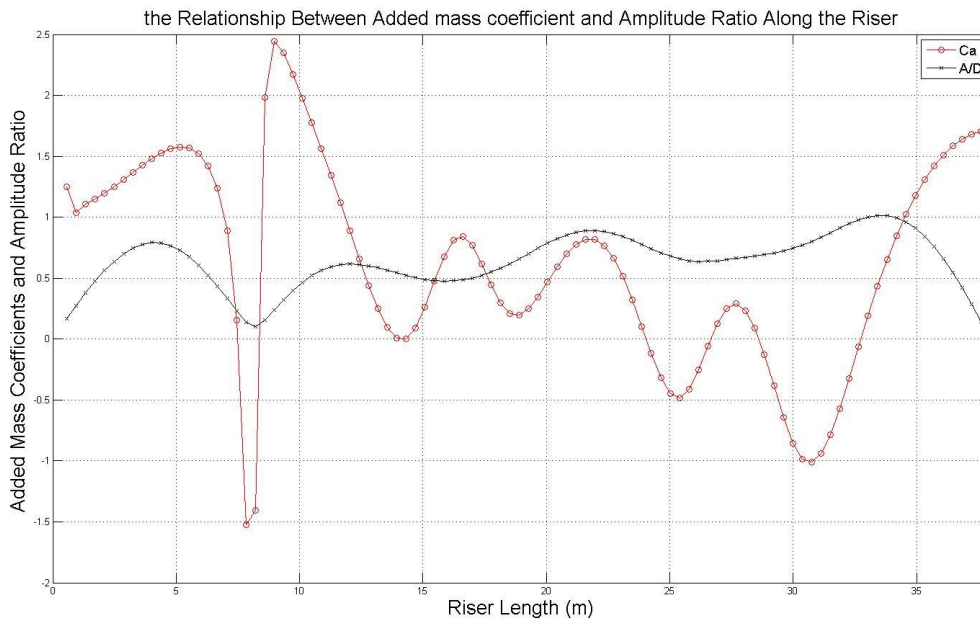


Figure 4.23: added mass coefficient and non-dimensional amplitude along the riser length

We can see at the length of 7m, the C_a has a deep drop from 2.5 to -1.5, that's because that at this point, the vibration amplitude of the riser is very small, almost zero, so even a small disturbance may cause large difference. As a result, we should neglect the data which is too low for the corresponding vibration amplitude.

4.3 Summary

In this chapter, we use inverse analysis to calculate the force coefficients for shear flow case and uniform case separately. For the shear flow case, we made the contour plots and make comparison with the results from the rotating rig test. For uniform flow cases we compare the results with the model in VIVANA:

We also tried different weighting parameters in the cost function to see the influence on the force coefficients we found the higher the parameter ,the closer the results from the invers analysis to the measured results.

Chapter 5

Comparison of Excitation Coefficients

5.1 The Venugopal's Damping Model

As we have already known, the inverse analysis can give us quite good results within the excitation range of the riser, while outside the excitation range, especially in the low reduced velocity range (close to the left end side of the riser). The results are quite unrealistically low (see figure 4.8), as we explained, it's because of the low velocity in this range, and small disturbances can cause large uncertainty. In VIVAVA, there is a damping model which is used to calculate the excitation coefficients in the damping range-the Venugopal's damping model. We should make comparison with the results from inverse analysis and the results from the damping model.

5.1.1 Dimensional Damping Coefficients.

As we said, the riser may have different excitation and damping regions depending on the actual excitation frequency, the cross-section properties and local flow velocity. [26]

The dynamic equilibrium equation for a single degree of freedom system is shown below:

$$m\ddot{x} + c\dot{x} + kx = F_v \quad (5.1)$$

If F_v is a single harmonic force, then the equation can be written as:

$$(m + am)\ddot{x} + (c_{str} + c_f)\dot{x} + kx = 0 \quad (5.2)$$

where am is the added mass and c_f is the excitation force. If c_f is negative, it's exciting the system (putting energy into the system).

Venugopal proposed three damping expressions for still water, low reduced velocity and high reduced velocity separately. The reduced velocity is give below:

$$U_R = \frac{2\pi U}{\omega D} \quad (5.3)$$

Where U is the incident velocity, D is the diameter, and ω is the frequency of cross-flow oscillation.

The damping force coefficients on a cylinder section with diameter D , oscillating with cross-flow amplitude of x_0 , frequency ω , in a fluid with density ρ , viscosity ν , and incident velocity U is given as:

Damping in Still Water:

$$c_{sw} = \frac{\omega\pi\rho D^2}{2} \left[\frac{2\sqrt{2}}{\sqrt{\text{Re}_\omega}} + k_{sw} \left(\frac{x_0}{D} \right)^2 \right] \quad (5.4)$$

Where

$$\text{Re}_\omega = \omega D^2 / \nu \quad (5.5)$$

The first part of eq 5.4 corresponds to the skin friction according to Stoke's law. The second part is the pressure-dominated force. The factor k_{sw} is a value found from curve fitting to be 0.25.

Low Reduced Velocity Damping:

$$c_1 = c_{sw} + \rho D U C_{vl} \quad (5.6)$$

The damping is increasing linearly with respect to the incident flow velocity. The coefficient C_{vl} was found to be 0.18 bases on measurements.

High Reduced Velocity Damping

$$c_2 = \rho \frac{U^2}{\omega} C_{vh} \quad (5.7)$$

This coefficient is independent of the amplitude ratio. The coefficient C_{vh} was found to be 0.2 based on the measurement.

5.1.2 Non-Dimensional Damping Coefficients.

The damping force model may be expressed in a non-dimensional way by transforming it into an equivalent lift force (with negative lift coefficient),

$$F_L(t) = \frac{1}{2} \frac{\rho D U^2 C_L \dot{x}}{\omega x_0} \quad (5.8)$$

By requiring the same energy loss per cycle using F_L we got the following relation between the dimensional force coefficient and the non-dimensional lift coefficient:

$$c_f = -\frac{1}{2} \frac{\rho D U^2 C_L}{\omega x_0} \quad (5.9)$$

And similarly, we can express in drag coefficient

$$c_f = \frac{4}{3\pi} \rho D \omega x_0 C_D \quad (5.10)$$

We will then arrive at the following results:

Damping in Still Water:

Expressed using drag coefficient $C_{D,sw}$

$$C_{D,sw} = \frac{3\sqrt{2}\pi^2}{4\sqrt{\text{Re}_w}} \frac{1}{\left(\frac{x_0}{D}\right)} + \frac{3k_{sw}\pi^2}{8} \left(\frac{x_0}{D}\right) \quad (5.11)$$

Low Reduced Velocity Damping:

Expressed using drag coefficient $C_{D,lv}$

$$C_{D,lv} = \frac{3}{8} \frac{U_r}{\left(\frac{x_0}{D}\right)} C_{vl} + C_{D,sw} \quad (5.12)$$

Expressed as lift coefficient $C_{L,lv}$

$$C_{L,lv} = \frac{-8\sqrt{2}\pi^3}{\sqrt{\text{Re}_w}} \frac{\left(\frac{x_0}{D}\right)}{U_R^2} - 4\pi^3 k_{sw} \frac{\left(\frac{x_0}{D}\right)^3}{U_R^2} - 4\pi C_{vl} \frac{\left(\frac{x_0}{D}\right)}{U_R} \quad (5.13)$$

High Reduced Velocity Damping:

Expressed using drag coefficient $C_{D,hv}$

$$C_{D,hv} = \frac{3}{16\pi} \frac{U_R^2}{\left(\frac{x_0}{D}\right)} C_{vh} \quad (5.14)$$

Expressed as lift coefficient $C_{L,hv}$

$$C_{L,hv} = -\frac{2x_0}{D} C_{vh} \quad (5.15)$$

5.2 Calculation for Non-Dimensional Damping Coefficients

From the formulas above we know that we need the non-dimensional amplitude A/D , the oscillating frequency ω and diameter D and viscosity ν .

From the data of the NDP test Case 2340 we can find the kinematic viscosity coefficient of water:

$$\nu = 1.188E-6 \quad (5.16)$$

Diameter of the riser:

$$D = 0.027m \quad (5.17)$$

Since the oscillation frequency along the riser is constant, we read from the experiment result and find the oscillating frequency is:

$$\omega = 16.755\text{rad/s} \quad (5.18)$$

Then

$$F_{osc} = 8/3 = 2.67\text{hz} \quad (5.19)$$

Since we have already calculated the non-dimensional amplitude A/D using inverse analysis, see the result in figure 5.1 below:

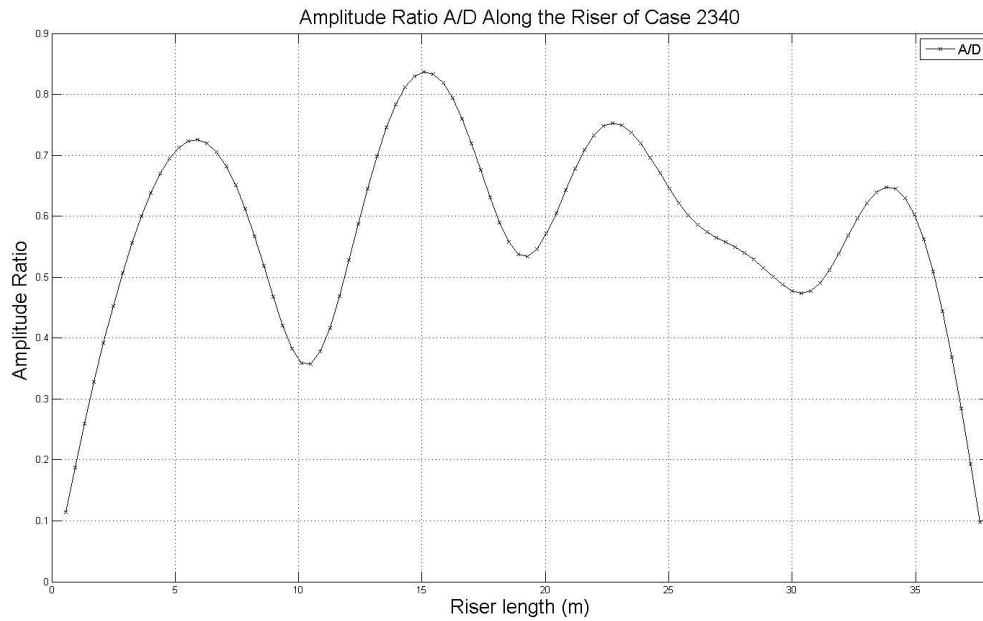


Figure 5.1: the non-dimensional amplitude A/D along the riser

Next we should plot the non-dimensional frequency \hat{f} along the riser. See the figure 5.2 below:

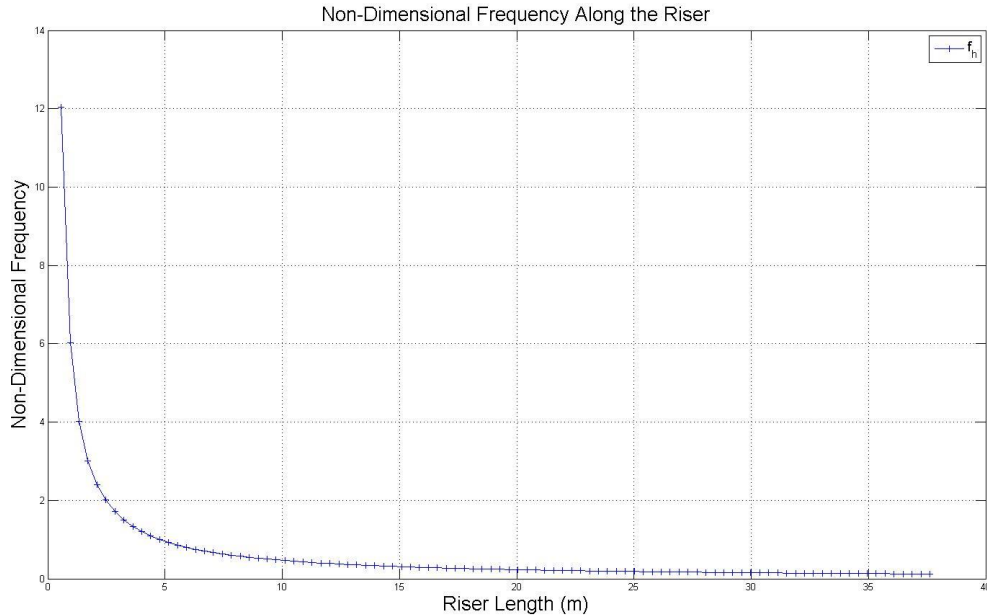


Figure 5.2: non-dimensional frequency \hat{f} along the riser

Since we know for the excitation range, the non-dimensional frequency ranges from 0.125 to 0.3 and outside this range is the damping range.

Read from the figure 5.2 above we found that in the left part of the riser, from 0m to 15.5m the \hat{f} is above 0.3, which means the riser of the section is in the damping range. From 15.5m to 38m the \hat{f} is between 0.125 and 0.3, which is in the excitation range. As a result, from the section 0 to 15.5m, we should use the Venugopal's damping model to calculate the damping force coefficient. And we should use the low reduced velocity damping formulas.

Then we can calculate and plot the damping coefficients based on the formulas above. By using Matlab, we got:

$$\text{Re}_\omega = \omega D^2 / \nu = 1.0281e + 04 \quad (5.20)$$

By using the equation 5.6, we got low reduced damping coefficients. Since the damping coefficients we got are dimensional, we have to find the non-dimensional coefficients in order to make comparison to the results we got from inverse analysis. We use the formula 5.13.

Plot the non-dimensional damping coefficients $C_{L,v}$ along the riser, see the figure 5.3 below:

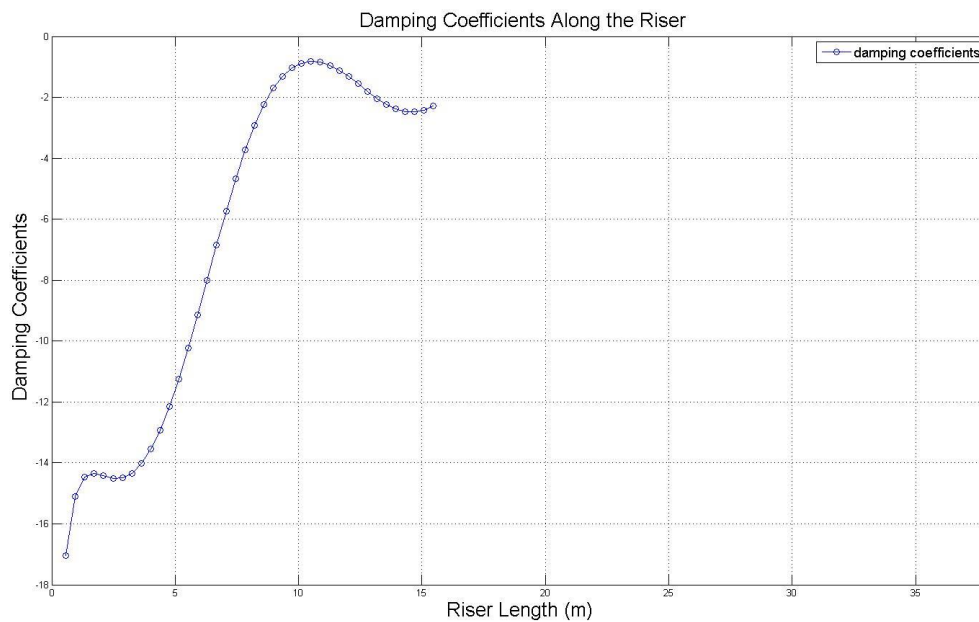


Figure 5.3: non-dimensional damping coefficients along the riser

Then we compare the non-dimensional coefficients with the result we got from inverse analysis. We plot the excitation coefficients with the non-dimensional damping coefficients together. See the figure 5.4 below:

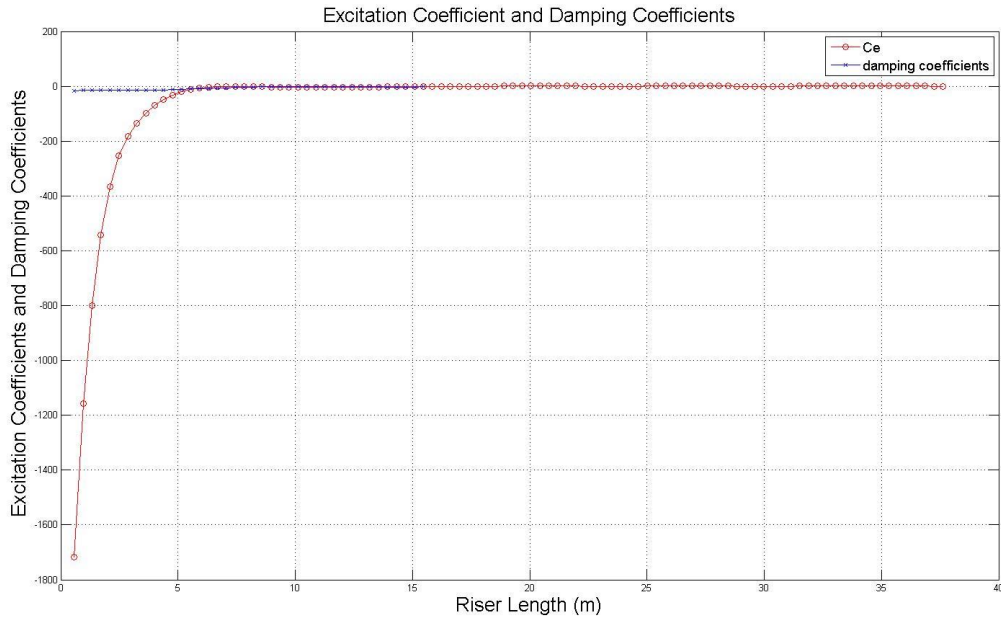


Figure 5.4: the non-dimensional damping coefficients and the excitation coefficients from inverse analysis

We zoom in to see the detail from the damping coefficients from 2 to -23 in order to see the details, see the figure 5.5 below:

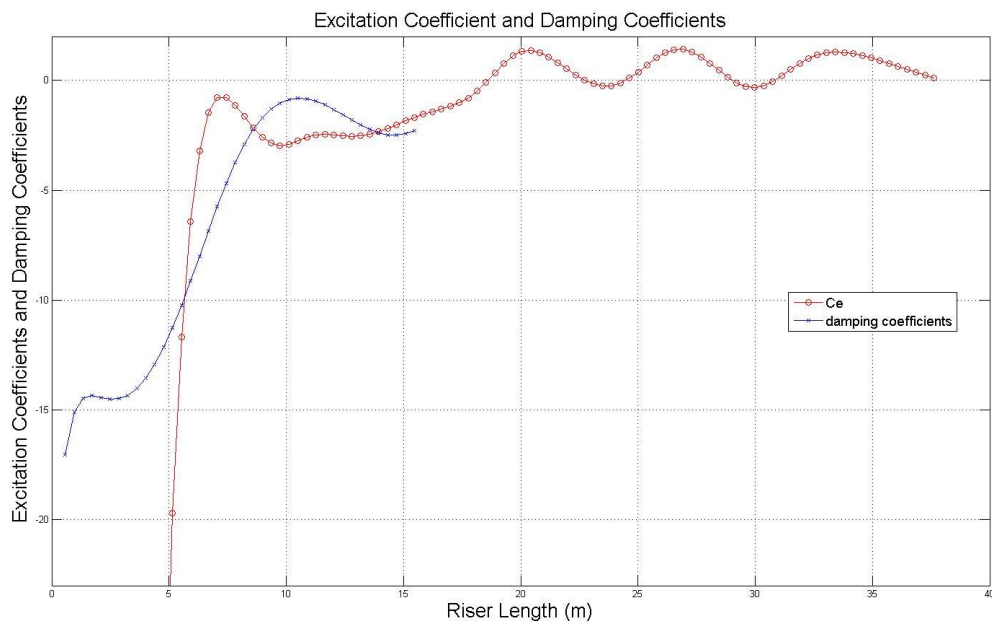


Figure 5.5: zoom in to see the details of the damping coefficients

We see from 8m to 15.5m, the excitation coefficients fits well, but from 0m to 8m the excitation coefficients are quite small, as we discussed before, when it's close to the left end of the riser, the velocity is nearly 0, which means that small turbulence will cause large difference.

As we can see from figure5.5, the results from Venugopal's damping model are more realistic.

5.3 Summary

We found the results from inverse analysis have large uncertainty when the velocity or acceleration is low.

We used the Venugopal's damping model which is used in VIVAVA to calculate the damping coefficients and find that the results are more reasonable than the inverse analysis when the frequency is outside the excitation range.

Chapter 6

Fatigue Analysis for NDP High Mode Tests

6.1 Pre-Processing of 44 NDP Test Cases

6.1.1 Introduction

Marine structures are in general subjected to dynamic loads. For risers, VIV gives a significant contribution to the fatigue damage.

We have discussed the inverse analysis method which can be used to calculate the force coefficients in Chapter 4. Next we have to some fatigue analysis to get a more profound knowledge of the fatigue damage of the risers for shear flow and uniform flow separately. Since VIVANA use band pass to process the data, we also have to find the influence of the band pass on the fatigue analysis.

In this paper, we choose 44 cases to analysis, which consist of 22 uniform flow cases and 22 shear flow cases. The maximum velocity of the cases varies from 0.3m/s to 2.2m/s. See table 6.1 below:

Table 6.1: Maximum Velocity for 44 NDP Cases

shear flow		uniform flow	
Case No.	Maximum Velocity U (m/s)	Case No.	Maximum Velocity U (m/s)
2310	0.3	2010	0.3
2320	0.4	2020	0.4
2330	0.5	2030	0.5
2340	0.6	2040	0.6

2350	0.7	2050	0.7
2360	0.8	2060	0.8
2370	0.9	2070	0.9
2380	1	2080	1
2390	1.1	2090	1.1
2400	1.2	2100	1.2
2410	1.3	2110	1.3
2420	1.4	2120	1.4
2430	1.5	2130	1.5
2440	1.6	2141	1.6
2450	1.7	2150	1.7
2460	1.8	2160	1.8
2470	1.9	2170	1.9
2480	2	2182	2
2490	2.1	2191	2.1
2500	2.2	2201	2.2
2510	2.3	2210	2.3
2520	2.4	2220	2.4

From the document- Specification for VIV predictions and Measurements-NDP 38m Riser Model [27], we can find the detailed physical properties of the riser:

Table 6.2: Detailed Property of the NDP Test Riser

Parameter	Dimension
Total length between pinned ends	38.00 m
Outer diameter	27 mm
Wall thickness of pipe	3.0 mm
Bending stiffness, EI	598.8Nm ²
Young modulus for pipe, E	3.62 E10 N/m ²
Axial stiffness, EA	5.09 E5 N
Mass (air filled), measured	0.761kg/m
Mass (water filled) estimated	0.933kg/m
Mass ratio	1.62

As we have already known, there are 24 strain gauges along the riser, as well as 8 accelerometers. The distance from the left end of the riser is shown in table 6.3:

Table 6.3: the Location of 24 Strain Gauges along the Riser

Cross-Flow strain gauges Number	Distance From Riser Top End (m)
1	2.555
2	3.084
3	3.224
4	4.155
5	6.030
6	8.609

7	8.889
8	10.285
9	13.676
10	16.452
11	16.891
12	19.997
13	20.193
14	21.393
15	22.460
16	23.165
17	25.153
18	26.254
19	28.863
20	29.365
21	31.191
22	33.005
23	36.559
24	37.322

Table 6.4: the Location of 8 Accelerometers along the Riser

Cross-Flow Accelerometer Number	Distance From Riser Top End (m)
1	4.155
2	8.609
3	13.676
4	16.891
5	21.393
6	25.153
7	28.863
8	33.005

Since we have the strain and acceleration signals from the NDP high mode test report, we can make a plot for the strain and acceleration signal separately of one test case of two output channels and make comparison. Choose case 2380 (1.0m/s shear flow) and make the plots. See the figure 6.1 and 6.2:

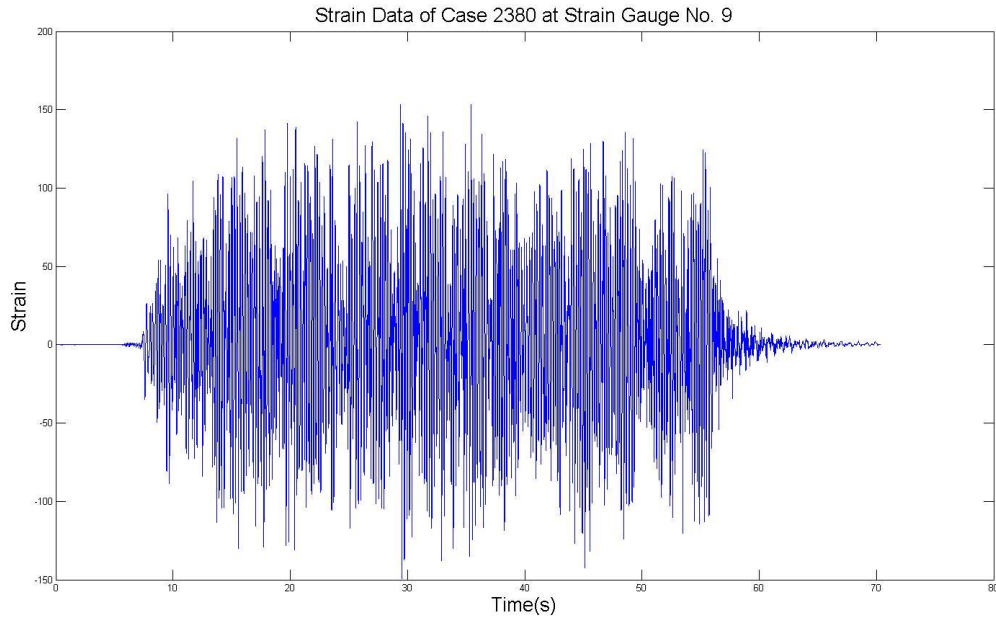


Figure 6.1: Strain of Case 2380 of Strain Gauge No.9

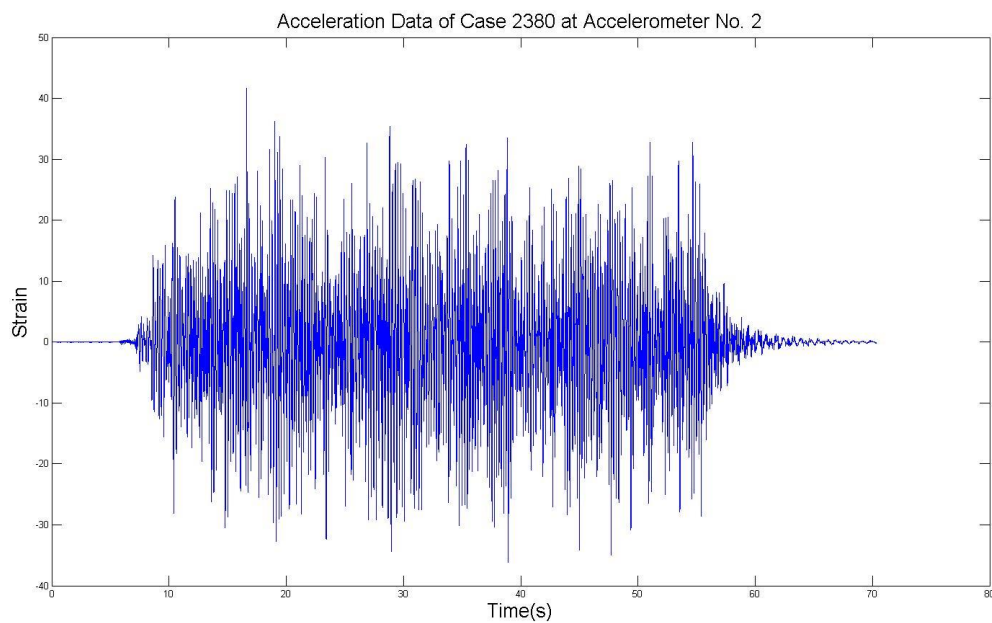


Figure 6.2: Acceleration of Case 2380 of Accelerometer No.2

See from the figures above, we can see that the strain signal and the acceleration signal of the same case share the same time range.

Before we go further we have to do some modification to the strain signals, when we check the strain signals from the experiments, it's quite obvious that there are something wrong at the strain gauge No. 21 for case 2420, 2430, 2440, 2450, 2460, 2470. Take case 2420 for example we plot the time series of the strain signals at strain gauge No. 20 and No. 21 together, see figure 6.3 below:

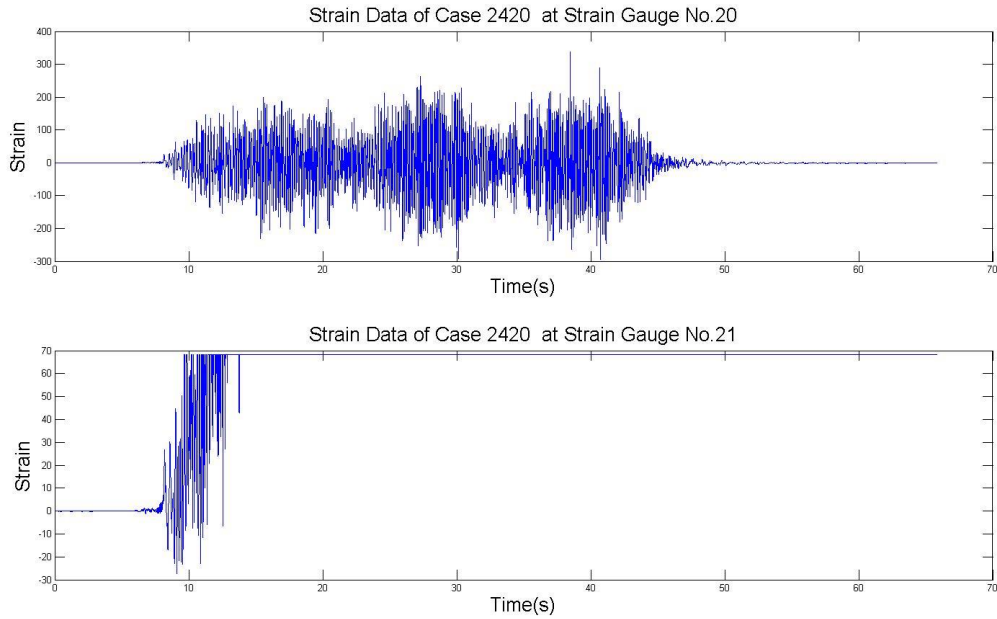


Figure 6.3: Strain of case 2420 of Strain Gauge No.20 and No.21

As we have expected, we can find it obviously that there is serious problems at strain gauge No. 21 during these experiments, while the strain signals from strain gauge No. 20 is quite reasonable. There are similar mistakes for other cases. In order to remove the mistakes introduced by the strain gauge No. 21, we decided not to use the experimental results at strain gauge No. 21 from case 2420 to 2470.

In order to make full use of the data and without introducing high uncertainty, we should define the time range we choose to use from the start time t_1 to the end time t_2 , since the time range of the strain and acceleration signal for the same case are the same, we can define t_1 and t_2 from strain signal only. Take shear flow case 2380 for example, we choose the strain signal from $t_1=13s$ to $t_2=54s$, and neglected the data outside this range, then re-plot it, see figure 6.4 below:

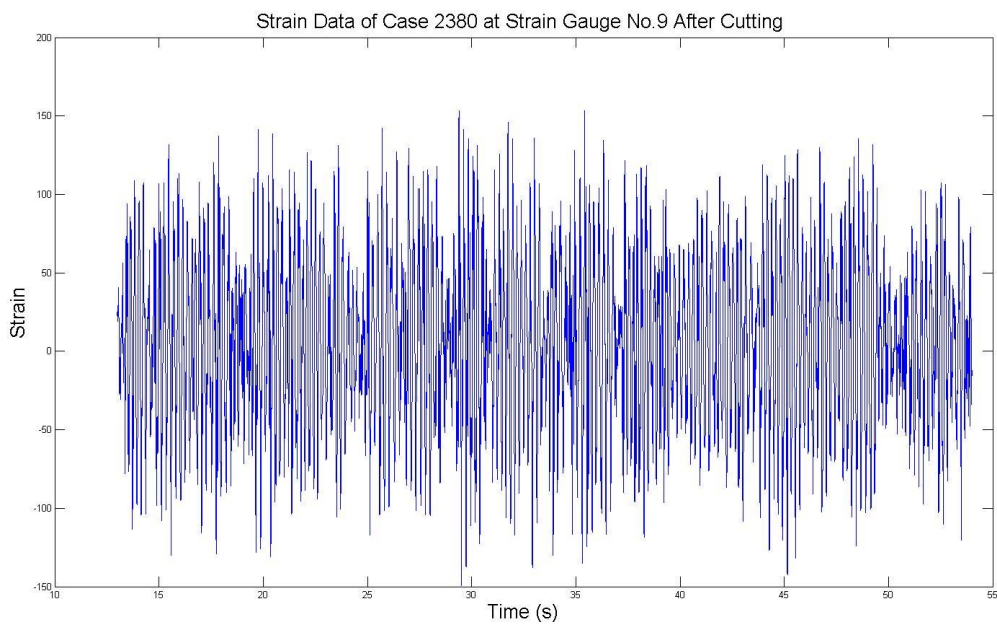


Figure 6.4: Strain Selected Between t1 and t2 of Case 2380 of Strain Gauge No. 9

From figure 6.4 we can see that we choose the range of the data which can represent the flow cases quite well and neglect the starting data and ending data which have large uncertainties.

Since the velocity for each case is different, the time ranges we choose to use are different as well. We have to define the t1 and t2 for all the 44 cases, see table 6.5 below:

Table 6.5: start time t1 and end time t2 for 44NDP cases

shear flow			uniform flow		
Case No.	t1(s)	t2(s)	Case No.	t1(s)	t2(s)
2310	11	170	2010	15	166
2320	10	128	2020	16	129
2330	10	104	2030	15	103
2340	11	87	2040	21	96
2350	9.2	75	2050	40	102
2360	9.8	65	2060	14	68
2370	10	58	2070	13	62
2380	13	54	2080	14	57
2390	10	50	2090	20	59
2400	10	45	2100	16	52
2410	11	43	2110	11	45
2420	13	41	2120	49	79
2430	11	39	2130	11	39
2440	12	37	2141	10	36
2450	12	35	2150	13	37
2460	10	34	2160	11.5	34
2470	11	32	2170	12.5	32
2480	11	31	2182	12	30
2490	13	30	2191	25	41
2500	11	31	2201	14	32
2510	11	29	2210	12	29
2520	11	29	2220	12	28

6.1.2 Band Pass Filtering of the Experiment Data

In this thesis, we will do the fatigue analysis not only in the total frequency range, but also in the $1 \times \omega$ frequency component range and the $3 \times \omega$ frequency component range.

Before that, we have to find out the dominant frequency of each case. First we must plot the spectrum for the strain of each case. Choose case 2380 for example, using Fourier transform for the strain signals of strain gauge 9 and plot the strain spectrum, see figure 6.5 below:

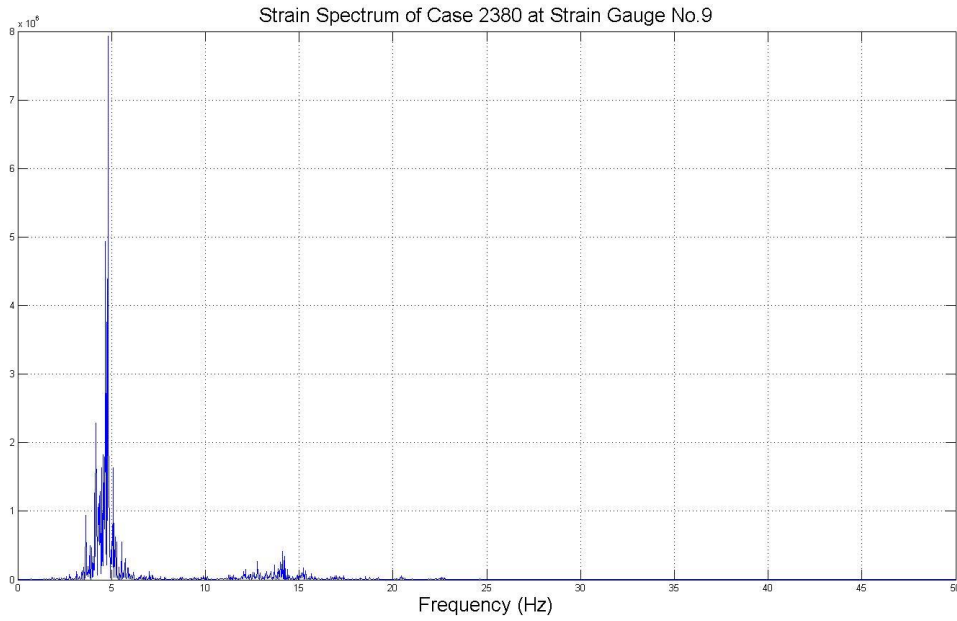


Figure 6.5: Spectrum of Strain Signal of case 2380 of Strain Gauge No.9

We can see it clearly that there are two peaks of the frequencies, the first peak is higher than the other, the frequency of the first peak is the dominant frequency, we represent it with ω , and for case 2380 ω is about 4.7 Hz. The frequency of the second peak is about 14.1 Hz, which is 3 times of the dominant frequency.

Then we should find out if the dominant frequency for strain signals and acceleration signals for the same case are the same, see figure 6.6 below:

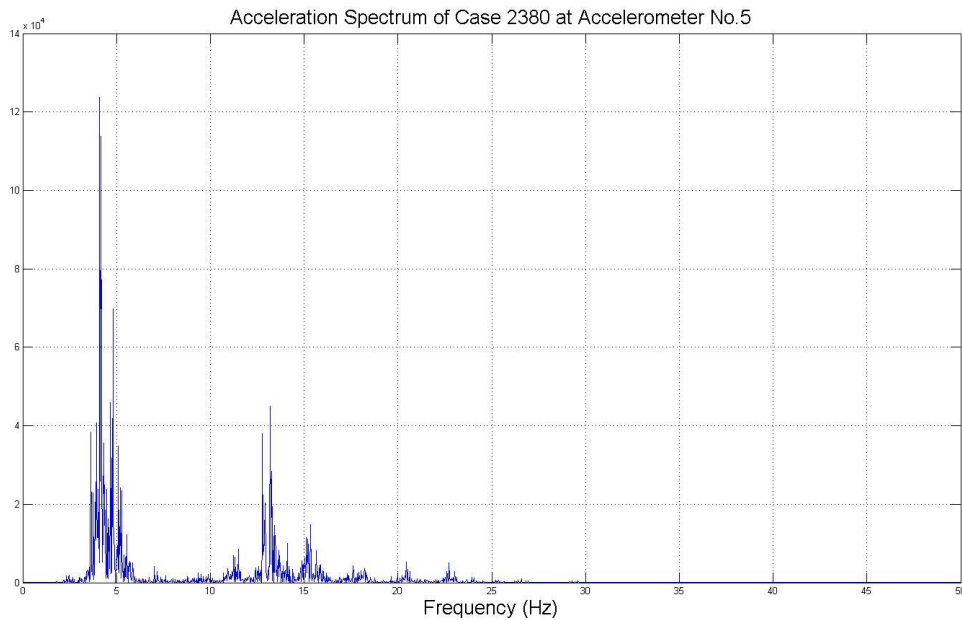


Figure 6.6: Spectrum of Acceleration Signal of case 2380 of Accelerometer No.5

We can see it clearly that the spectrum of the strain and the acceleration are quite similar to each other. And the dominant frequencies for strain signal and acceleration signal are the same.

Then we can get the dominant frequencies for all the 44 cases by reading the strain spectrum only, see table 6.6 below:

Table 6.6: the Dominant frequency for 44 NDP Cases

shear flow		uniform flow	
case	w(Hz)	case	w(Hz)
2310	1.5	2010	1.9
2320	2.1	2020	2.5
2330	2.4	2030	2.8
2340	2.7	2040	3.4
2350	3.4	2050	4.3
2360	4	2060	4.5
2370	4.2	2070	4.9
2380	4.7	2080	5.8
2390	5	2090	6.1
2400	5.6	2100	6.8
2410	6.4	2110	7.1
2420	6.9	2120	7.4
2430	7.1	2130	8.1
2440	7.7	2141	8.5
2450	7.9	2150	9.1
2460	8.1	2160	9.3
2470	8.5	2170	9.8
2480	9	2182	10.5
2490	9.4	2191	11.25
2500	9.8	2201	11.4
2510	10.8	2210	12
2520	11	2220	12.5

After defining the dominant frequency of each case, we can now do the total, $1 \times \omega$ and $3 \times \omega$ band pass filtering for the data. Take case 2380 for example, by using the strain signal from strain gauge 9, we can filter it in three different ways.

1. The total band pass filtering

We filter the data from 0.5ω to 3.5ω , ω is the dominant frequency which is 4.7 Hz, so the data we use is between 2.35 and 16.45 Hz . See figure 6.7 below:

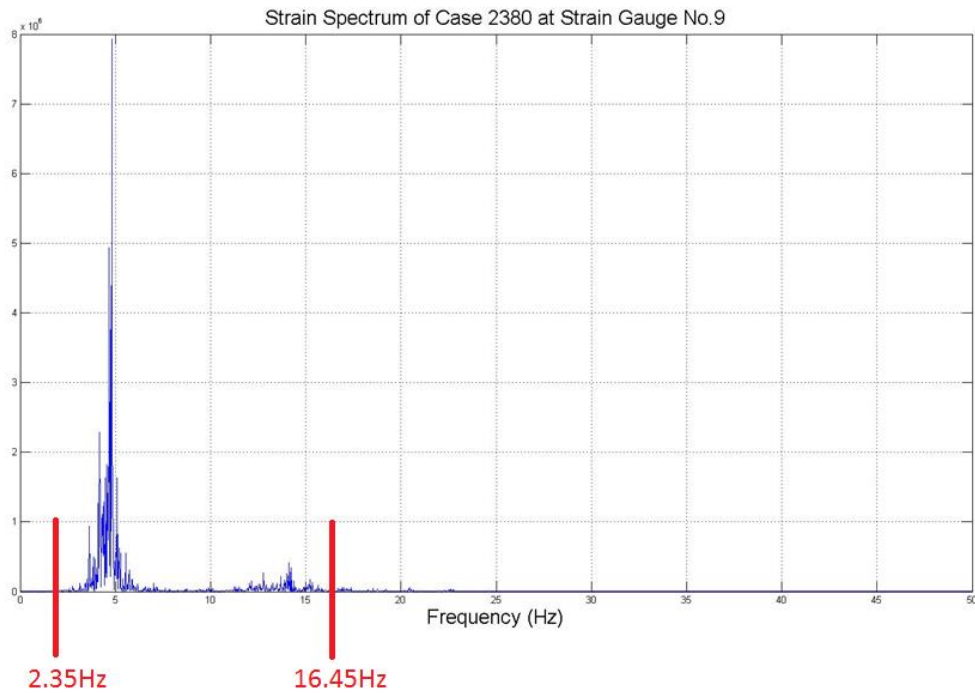


Figure 6.7: Total Band Pass of Case 2380 of Strain Gauge No.9

2. The $1 \times \omega$ band pass filtering

We only use the data of the first peak. Filter the data from 0.5ω to 1.5ω , for this case it means from 2.35Hz to 7.05 Hz, see figure 6.8 below:

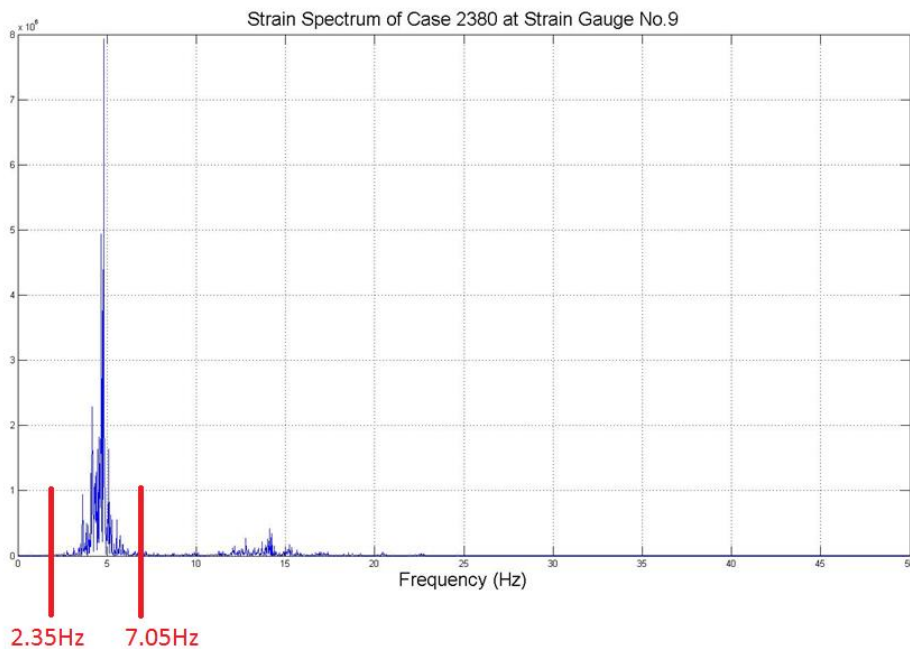


Figure 6.8: $1 \times \omega$ Band Pass of Case 2380 of Strain Gauge No.9

3. The $3 \times \omega$ band pass filtering,

We only use the data of the second peak, Filter the data from 2.5ω to 3.5ω , for this case it means from 11.75Hz to 16.45 Hz, see figure 6.9 below:

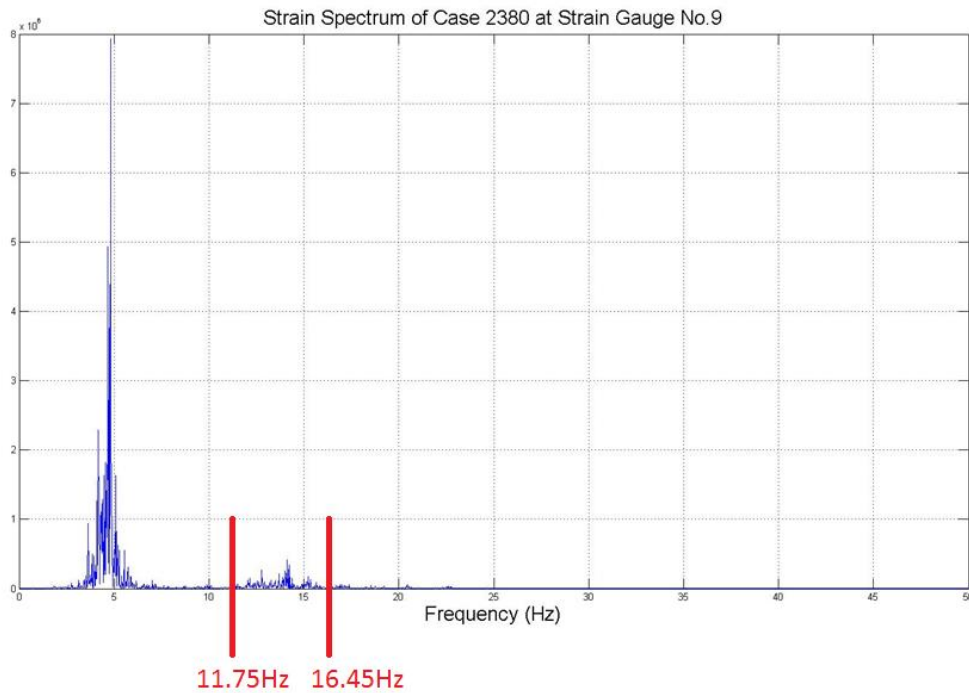


Figure 6.9: $3\times\omega$ Band Pass of Case 2380 of Strain Gauge No.9

Since we have already got the dominant frequency for all the 44 cases, we can easily define the frequency range for the total analysis, $1\times\omega$ analysis and $3\times\omega$ analysis for each case. See table 6.7 and 6.8 below:

Table 6.7: the Frequency Ranges for Total, $1\times\omega$ and $3\times\omega$ band pass filtering for 22 Shear Flow Cases

Case No.	shear flow					
	total band pass		1w band pass		3w band pass	
	0.5w(Hz)	3.5w(Hz)	0.5w(Hz)	1.5w(Hz)	2.5w(Hz)	3.5w(Hz)
2310	0.75	5.25	0.75	2.25	3.75	5.25
2320	1.05	7.35	1.05	3.15	5.25	7.35
2330	1.2	8.4	1.2	3.6	6	8.4
2340	1.35	9.45	1.35	4.05	6.75	9.45
2350	1.7	11.9	1.7	5.1	8.5	11.9
2360	2	14	2	6	10	14
2370	2.1	14.7	2.1	6.3	10.5	14.7
2380	2.35	16.45	2.35	7.05	11.75	16.45
2390	2.5	17.5	2.5	7.5	12.5	17.5
2400	2.8	19.6	2.8	8.4	14	19.6
2410	3.2	22.4	3.2	9.6	16	22.4
2420	3.45	24.15	3.45	10.35	17.25	24.15
2430	3.55	24.85	3.55	10.65	17.75	24.85
2440	3.85	26.95	3.85	11.55	19.25	26.95
2450	3.95	27.65	3.95	11.85	19.75	27.65

2460	4.05	28.35	4.05	12.15	20.25	28.35
2470	4.25	29.75	4.25	12.75	21.25	29.75
2480	4.5	31.5	4.5	13.5	22.5	31.5
2490	4.7	32.9	4.7	14.1	23.5	32.9
2500	4.9	34.3	4.9	14.7	24.5	34.3
2510	5.4	37.8	5.4	16.2	27	37.8
2520	5.5	38.5	5.5	16.5	27.5	38.5

Table 6.8: the Frequency Ranges for Total, $1 \times \omega$ and $3 \times \omega$ Band Pass for 22 Uniform Flow Cases

uniform flow						
case	total band pass		1w band pass		3w band pass	
	0.5w(Hz)	3.5w(Hz)	0.5w(Hz)	1.5w(Hz)	2.5w(Hz)	3.5w(Hz)
2010	0.95	6.65	0.95	2.85	4.75	6.65
2020	1.25	8.75	1.25	3.75	6.25	8.75
2030	1.4	9.8	1.4	4.2	7	9.8
2040	1.7	11.9	1.7	5.1	8.5	11.9
2050	2.15	15.05	2.15	6.45	10.75	15.05
2060	2.25	15.75	2.25	6.75	11.25	15.75
2070	2.45	17.15	2.45	7.35	12.25	17.15
2080	2.9	20.3	2.9	8.7	14.5	20.3
2090	3.05	21.35	3.05	9.15	15.25	21.35
2100	3.4	23.8	3.4	10.2	17	23.8
2110	3.55	24.85	3.55	10.65	17.75	24.85
2120	3.7	25.9	3.7	11.1	18.5	25.9
2130	4.05	28.35	4.05	12.15	20.25	28.35
2141	4.25	29.75	4.25	12.75	21.25	29.75
2150	4.55	31.85	4.55	13.65	22.75	31.85
2160	4.65	32.55	4.65	13.95	23.25	32.55
2170	4.9	34.3	4.9	14.7	24.5	34.3
2182	5.25	36.75	5.25	15.75	26.25	36.75
2191	5.63	39.38	5.63	16.88	28.13	39.38
2201	5.7	39.9	5.7	17.1	28.5	39.9
2210	6	42	6	18	30	42
2220	6.25	43.75	6.25	18.75	31.25	43.75

6.2 Calculation of Non-Dimensional Amplitude and Stress along the Riser

6.2.1 Non-Dimensional Amplitude Analysis

Before the fatigue analysis, we have to study the non-dimensional amplitude A/D along the riser from the experimental data of accelerometers. This A/D is actually the root mean square

of the amplitude of the riser cross flow displacements, here we use A/D to represent the Y_{rms} / D . Y is the cross flow displacement of the riser.

Since we have 8 accelerometers along the riser, we have the acceleration signal, we can get the displacement by double integration. For the cross flow acceleration signals along the riser, we can also band pass the signal in total frequency range, the $1 \times \omega$ band pass frequency range and the $3 \times \omega$ band pass filtering frequency range. As we know, the strain signal and the acceleration signal share the same critical frequency ω , we can band pass the acceleration signal just like the strain signal.

We can see it clearly the effect of the response amplitude with and without band pass. Select case 2380, we choose the acceleration signal at the 4th accelerometer, we plot the displacement of the accelerometer for total band pass, with $1 \times \omega$ band pass, and with $3 \times \omega$ band pass together, see figure 6.10 below:

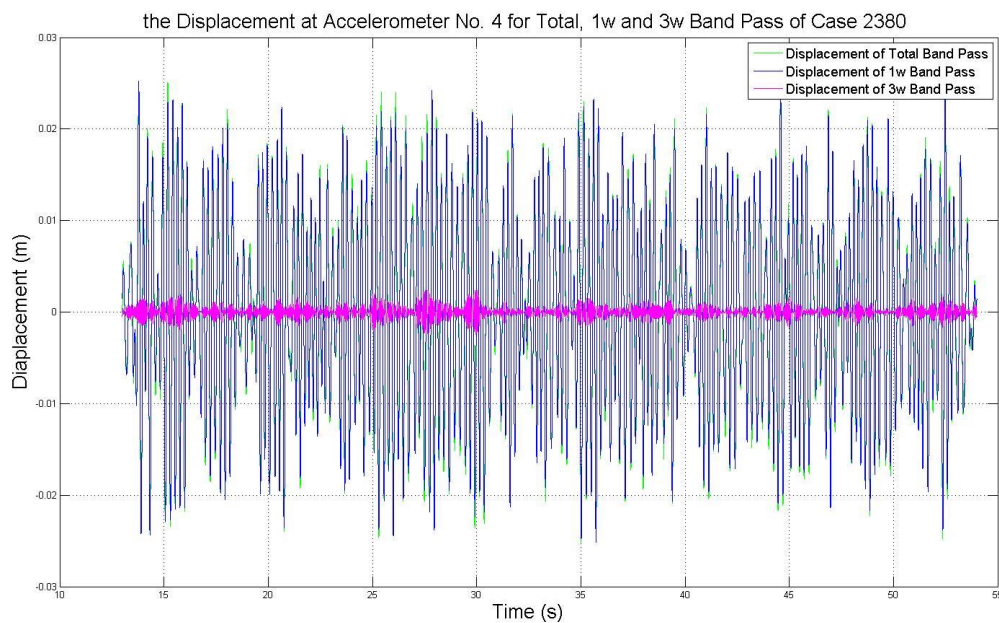


Figure 6.10: the Displacement of Accelerometer No.4 of Case 2380 of Total, $1 \times \omega$ and $3 \times \omega$ Band Pass

If we zoom in, we can see the details.

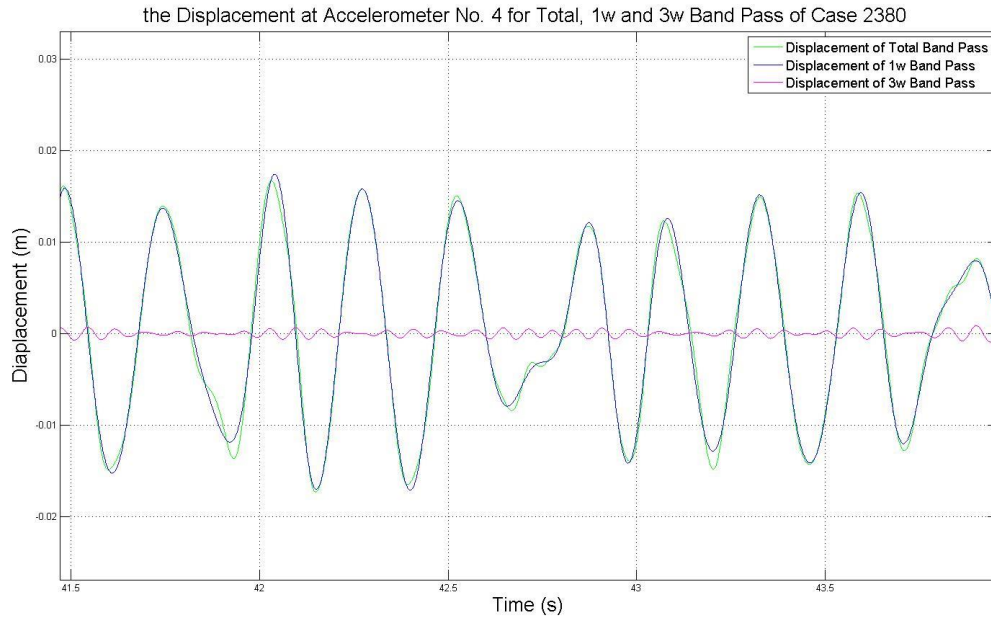


Figure 6.11: the Displacement of Accelerometer No.4 of Case 2380 of Total, $1 \times \omega$ and $3 \times \omega$ Band Pass in detail

See from the figures above, we can find that there are no significant difference between total and $1 \times \omega$ band pass filtering. But we can see the difference when we zoom in. After $1 \times \omega$ band pass filtering the higher order displacement is filtered out. While after $3 \times \omega$ band pass filtering, the displacement have big differences with the total band pass filtering.

It's easy to explain because see from the spectrum plot, we can see that most of the energy is concentrated around the critical frequency ω , while around the $3 \times \omega$ range, the energy is small. So when we get displacements after double integration, we can see that the amplitude of total displacement has no big difference with $1 \times \omega$ amplitude but is much larger than the $3 \times \omega$ band pass amplitude.

Then, we can plot the A/D along the riser at 8 accelerometers, plot the A/D with total, $1 \times \omega$ and $3 \times \omega$ band pass together. For case 2380 and 2080, see figures 6.12 and 6.13 below:

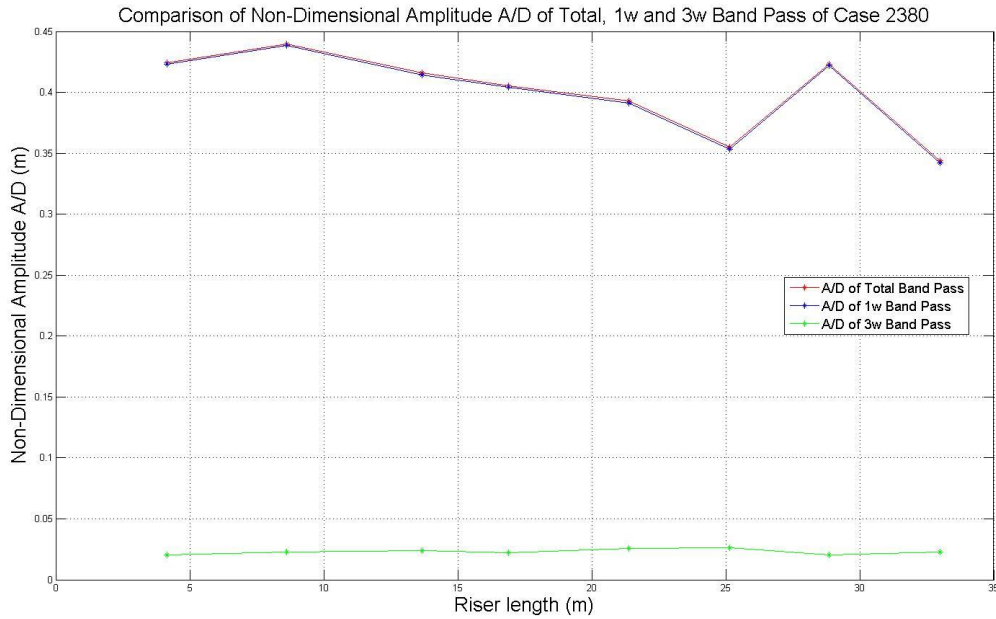


Figure 6.12: Non-Dimensional Amplitude A/D of Total, $1 \times \omega$ and $3 \times \omega$ Band Pass of case 2380

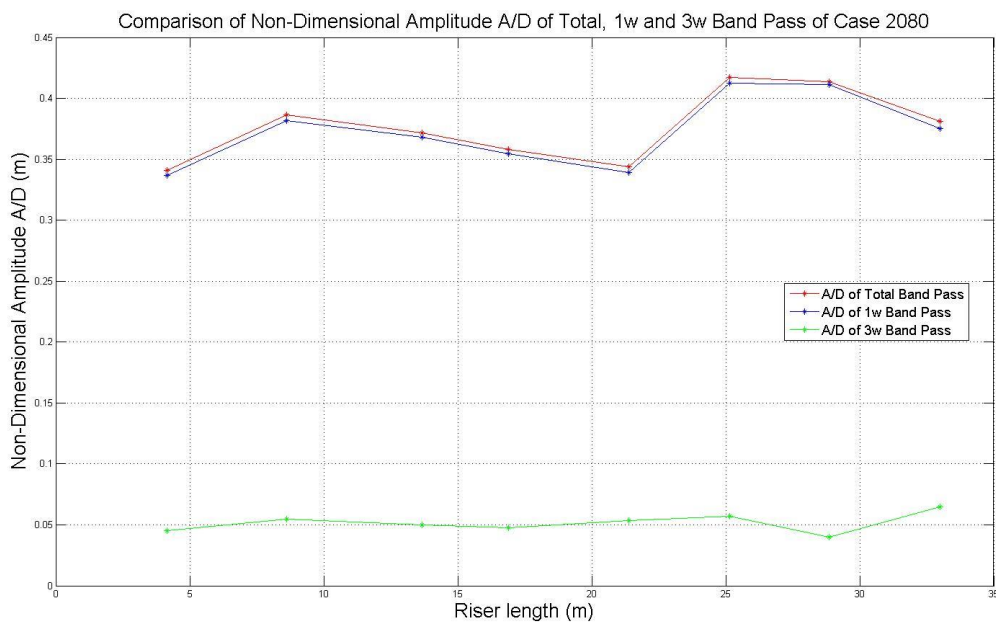


Figure 6.13: Non-Dimensional Amplitude A/D of Total, $1 \times \omega$ and $3 \times \omega$ Band Pass of case 2080

See from the figures above, we can find that as we have expected, the total non-dimensional amplitude A/D is a little higher than that of the $1 \times \omega$ band pass. And they are both much higher than the results from $3 \times \omega$ filtering.

Since we have only 8 accelerometers along the riser, the curve we got is too rough to see the detail.

6.2.2 Standard Deviation of Stress of NDP tests

After the non-dimensional amplitude analysis, we go on to do the stress analysis of the riser

Since we get the strain signals along the riser for the 44 cases, we can get the stress easily.

We get the standard deviation of stresses along the risers. Take case 2380 and 2080 for example, we can get the stress signals from the strain signals of the 24 strain gauges, see figures 6.14 and 6.15 below:

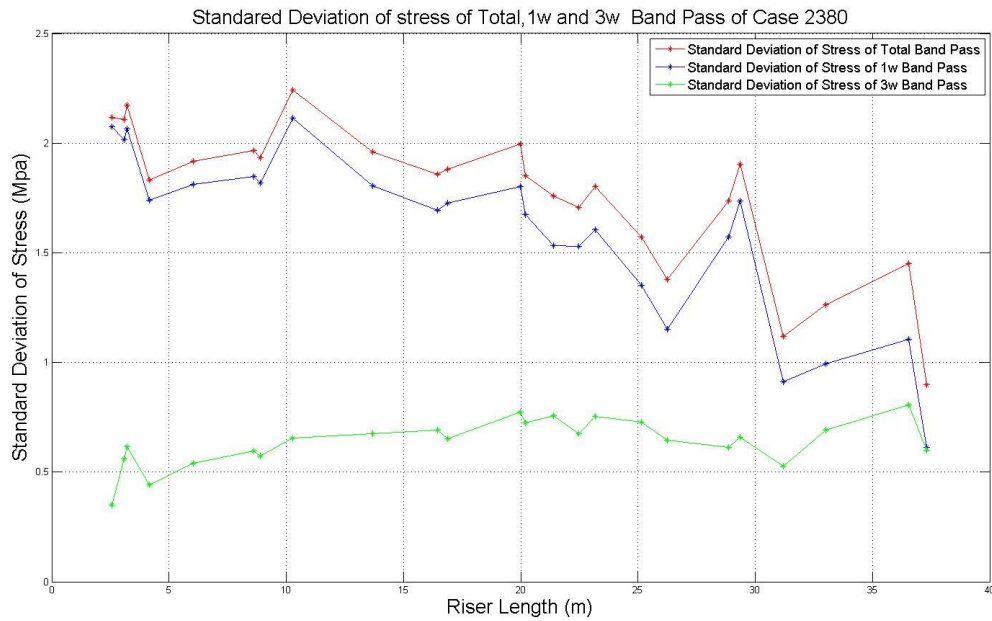


Figure 6.14: Standard Deviation of Stress of Total, $1 \times \omega$ and $3 \times \omega$ Band Pass along the Riser of Case 2380

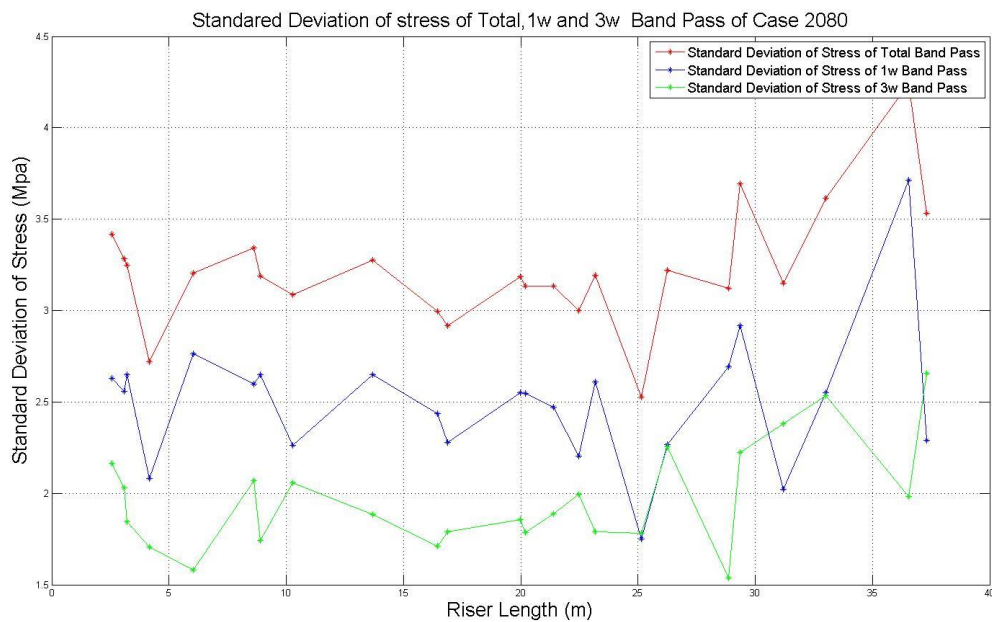


Figure 6.15: Standard Deviation of Stress of Total, $1 \times \omega$ and $3 \times \omega$ Band Pass along the Riser of Case 2080

See from figure 6.14 to 6.15, we can see that for shear flow case and uniform case, the $1 \times \omega$ band pass gives a large contribution to the stress along the riser, and larger than the contribution from $3 \times \omega$ band pass, which is different from the annual cumulative fatigue damage.

6.3 Calculation of Annual Cumulative Fatigue Damage along the Riser

6.3.1 SN Curve

After defining the frequency range for the cases, we can do the fatigue analysis to get the cumulative damage now.

For the NDP 38m riser model test, we use the SN curve which is give in the Specification for VIV Predictions and Measurements-NDP 38m Riser Model [27]. See table 6.9 below:

Table 6.9: SN Curve Used for Fatigue Analysis

Parameter	Value
S-N curve	DNV F2 single slope $\log \bar{a} = 11.63; m = 3.0$
SCFs	1.0 everywhere
Notes: 1. $\log(N) = \log \bar{a} - m \cdot \log(s)$, where N is the predicted number of cycles to failure under stress range S (Mpa) m is the inverse slope of the SN curve log used in the notation is log to the base 10	

6.3.2 Rain Flow Counting Method

Rain flow counting is designed to count reversals in accordance with the material's stress-strain response. The principle may be illustrated by the strain history shown in figure 6.16 and the corresponding stress-strain path. The individual cycle 2-3-2' does not affect the remainder of the stress-strain history. Each time the hysteresis loop is closes, a cycle count is made. The method is illustrated for a more complicated strain history in figure 6.17.

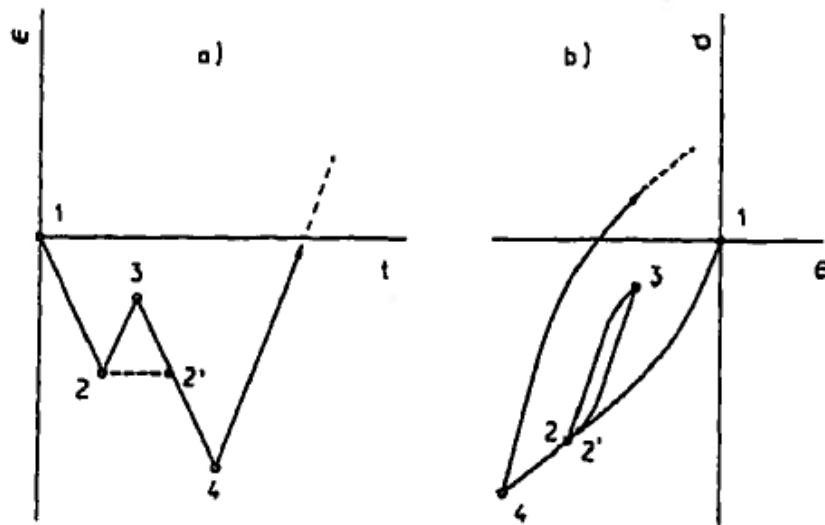


Figure 6.16: Part of a strain history (a) and the stress-strain response (b) of a material being subjected to this history. Note that the small cycle 2-3-2' forms a closed hysteresis loop within the large range 1-4, the latter being undisturbed by the interruption.[28]

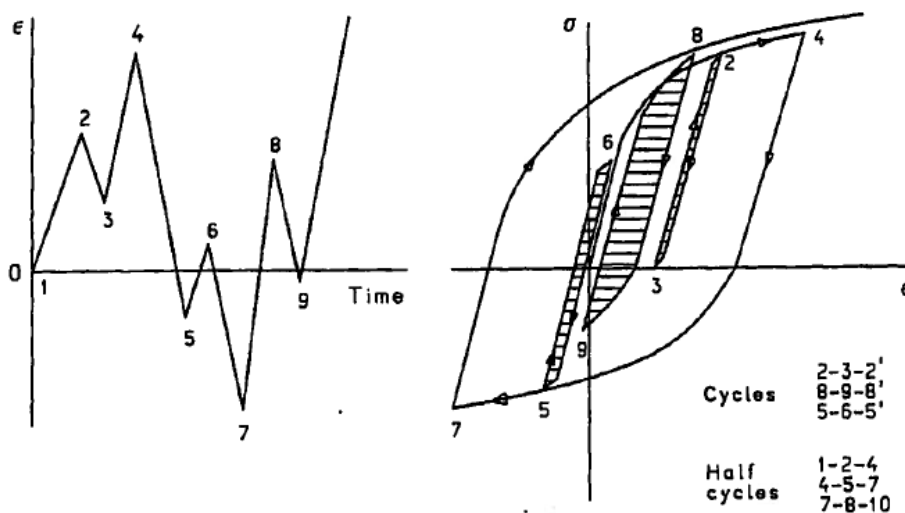


Figure 6.17: A more complicated strain history (a) and the corresponding stress-strain response (b). The rain flow counting method counts small cycles within large cycles similar to the way closed hysteresis loops are formed. The cycle count is thus reflecting the way in which the material responding.[28]

6.3.3 Miner Summation

Fatigue design of welded structures is based on constant amplitude SN data. A marine structure, however, will experience a load history of a stochastic nature.

The development of fatigue damage under stochastic or random loading is in general termed cumulative damage. Miner summation has proved to be no worse than any other method, and much simpler.

The basic assumption in the Miner summation method is that the ‘damage’ on the structure per load cycle is constant at a given stress range and equal to

$$D = \frac{1}{N} \quad (6.1)$$

Where N is the constant amplitude endurance at the given stress range. In a constant amplitude test, this leads to the following failure criterion

$$D_f \geq 1 \quad (6.2)$$

With the failure criterion given by equation 6.2, the procedure of calculating Miner summation is shown in figure 6.18 below:

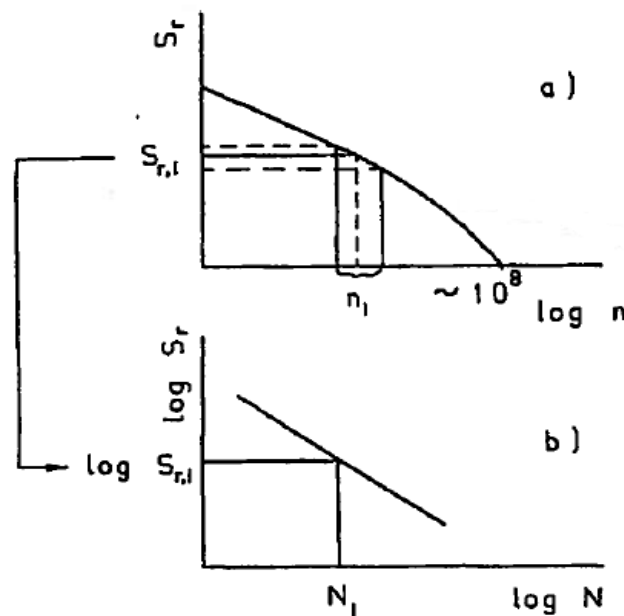


Figure 6.18: the Miner summation for one particular stress block with stress range exceeding diagram (a) and SN curve (b).[28]

In this thesis, we are calculating the annual cumulative damage for 44 cases. We calculate the annual cumulative fatigue damage at 24 strain gauges along the riser for each case.

See from table 6.5, the time of each test we use ranges from t_1 to t_2 , the annual cumulative fatigue damage means that we repeat this test interval for one year long and get the cumulative damage.

6.3.4 Total, $1 \times \omega$ and $3 \times \omega$ Frequency Component Fatigue Damage

We can now get the results of each case at the location of 24 strain gauges for total, $1w$ and $3w$ annual cumulative fatigue damage.

In order to make sure my calculation method is correct, we can compare my results with the results from literature- 38m_Riser_Case_Data_VIVANA to see if my calculation method is correct.

See the figures 6.19 below, we choose case 2080 and 2380 separately and plot the results presently with the results from the literature together, see the figures 6.19 to 6.20 below:

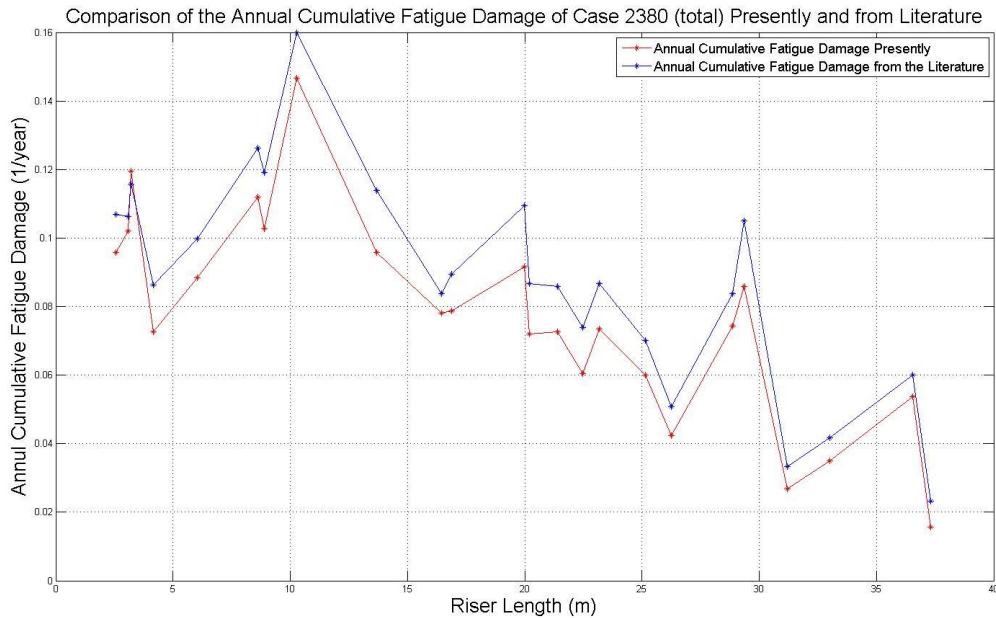


Figure 6.19: Total Annual Cumulative Fatigue Damage of Case 2380 presently and from literature

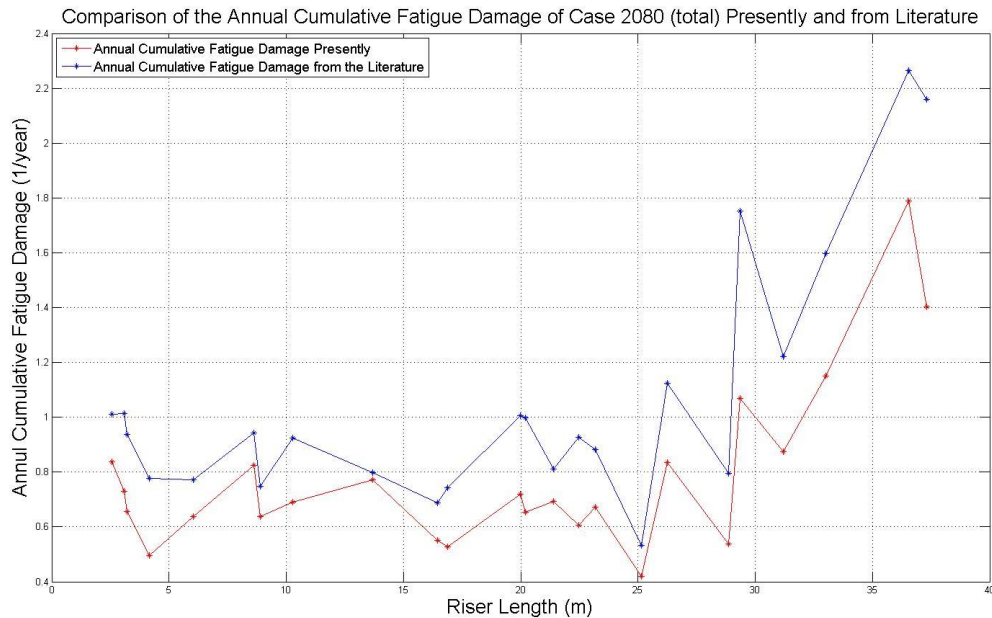


Figure 6.20: Total Annual Cumulative Fatigue Damage of Case 2080 presently and from literature

We can see from the results presently and the results from literature have the same trends, and the value is quite close to each other, and the results presently is a little lower than the results from literature which means that the results we got is a more conservative than the previous result.

Using the same method, we can compare the $1 \times \omega$ band pass annual cumulative damage result presently with the results from the literature. Since the $1 \times \omega$ band pass annual cumulative damage results from the literature is only available for the uniform flow, we can compare the results for the case 2080 only, see figure 6.21 below:

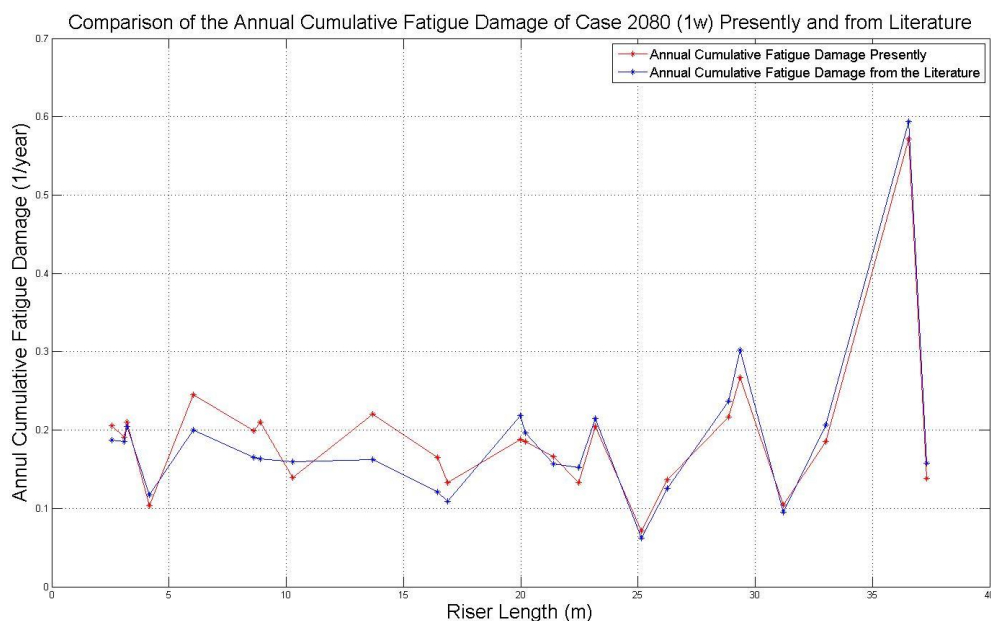


Figure 6.21: $1 \times \omega$ Annual Cumulative Fatigue Damage of Case 2080 presently and from literature

See from the figure above, the results from the S-N curve and the measurements are quite close to each other after $1 \times \omega$ band pass filtering. And some of the annual cumulative damage at the location of the strain gauges along the riser presently are large than the results from the literature, while others are lower, which is different from the total damage cases.

6.3.5 Difference of Total, $1 \times \omega$ and $3 \times \omega$ Fatigue Damage

Then we can see the difference of the fatigue damage for the total analysis and after $1 \times \omega$ filtering and $3 \times \omega$ filtering, we analyzed total 44 cases, see appendix A.1 and A.2. Here we only choose case 2380 and case 2080, we can see the difference between the annual cumulative fatigue damage, see figures 6.22 and 6.23 below:

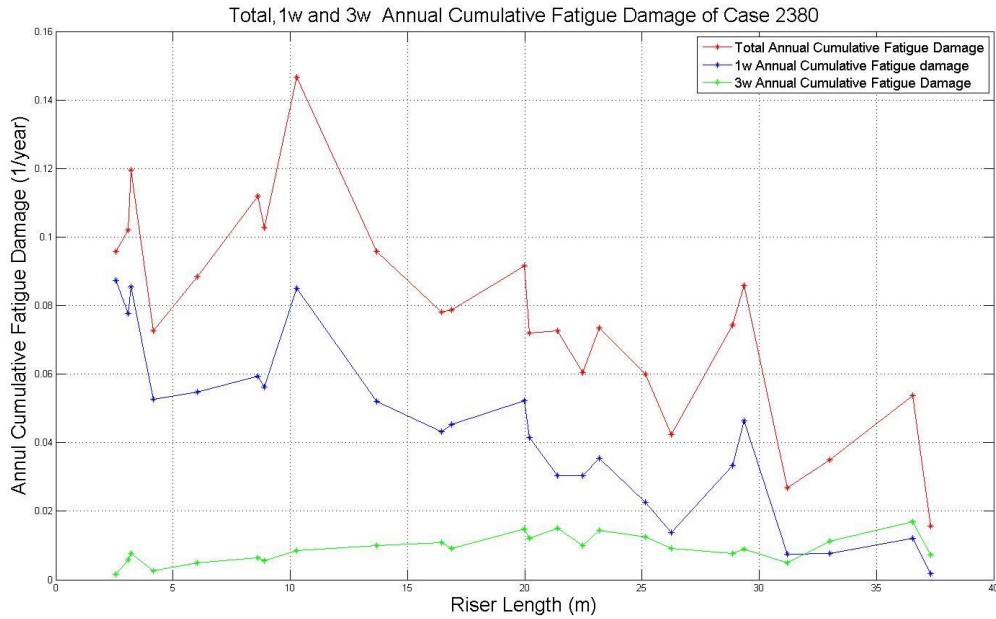


Figure 6.22: Annual Cumulative Fatigue Damage of Case 2380 of Total, $1 \times \omega$ and $3 \times \omega$ Band Pass

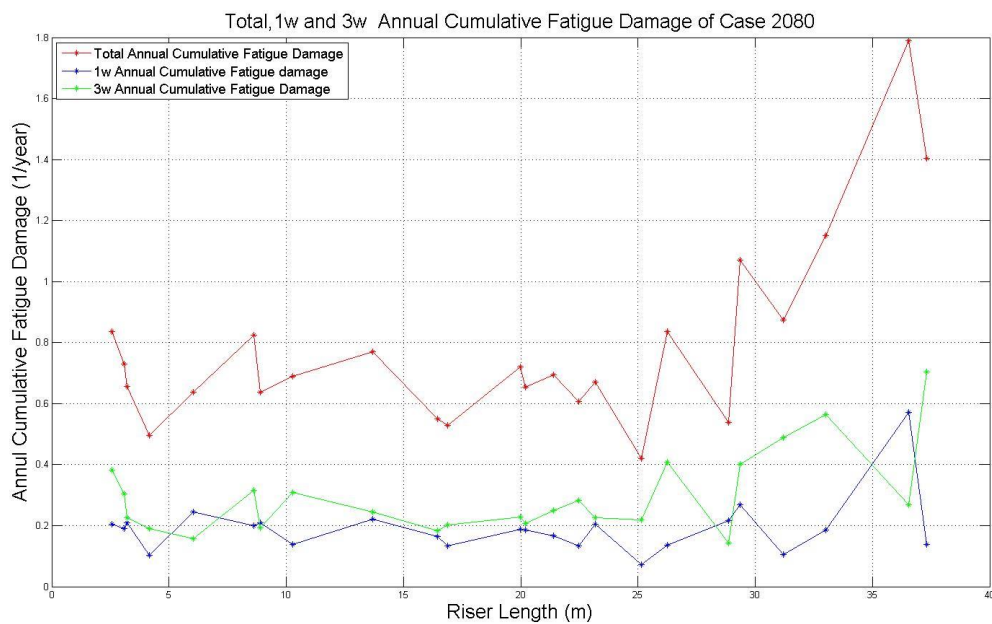


Figure 6.23: Annual Cumulative Fatigue Damage of Case 2080 of Total, $1 \times \omega$ and $3 \times \omega$ Band Pass

See from the figures above, we can find that the fatigue damage of total fatigue damage is larger than the $1 \times \omega$ and $3 \times \omega$ annual cumulative fatigue damage, for shear flow case 2380, the $1 \times \omega$ annual cumulative fatigue damage is larger than $3 \times \omega$ annual cumulative fatigue damage, except when it comes close to the right end of the riser, when the velocity is small. While for the uniform flow case 2080, the $1 \times \omega$ annual cumulative fatigue damage is almost the same with the $3 \times \omega$ annual cumulative fatigue damage along the riser.

6.3.6 Ratio of Fatigue Damage of Total, $1 \times \omega$ and $3 \times \omega$ Frequency Component

In order to see it clearly, we calculate the ratio of $1 \times \omega$ annual cumulative fatigue damage and $3 \times \omega$ annual cumulative fatigue damage with the total annual cumulative fatigue damage at the location of each strain gauge and plot the results along the riser for each case to see if there is any trend.

See the formulas below:

$$Rat_{1 \times \omega} = \frac{fat_{1 \times \omega}}{fat_{tot}} \quad (6.3)$$

$$Rat_{3 \times \omega} = \frac{fat_{3 \times \omega}}{fat_{tot}} \quad (6.4)$$

Then we can get $Rat_{1 \times \omega}$ and $Rat_{3 \times \omega}$ for each case. Then plot them together, see appendix B.1 and B.2. Neglect the data of the case 2420 to 2470 at the strain gauge No. 21. Take case 2080 and 2380 for example:

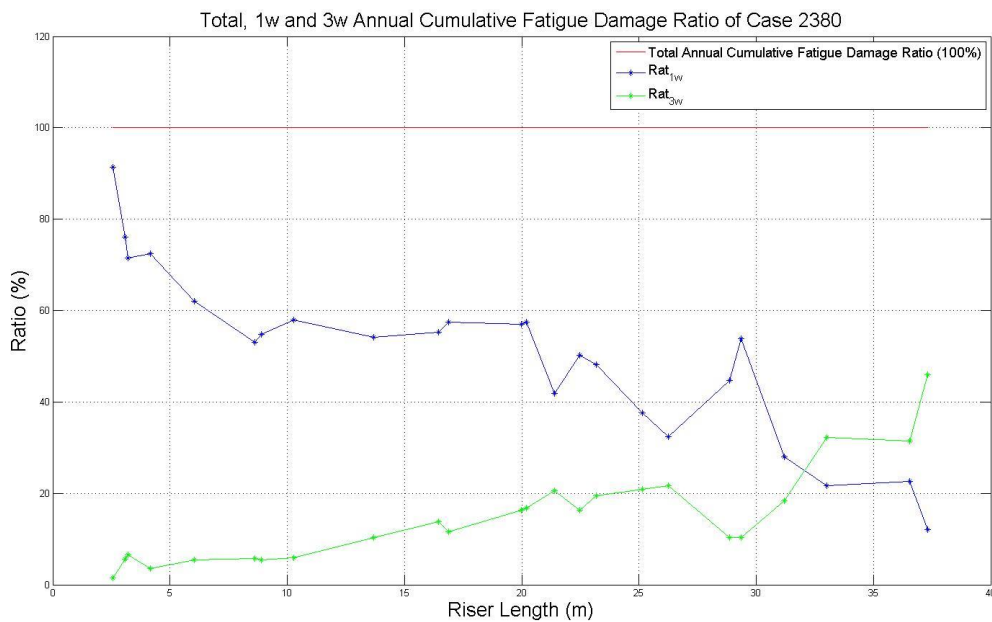


Figure 6.24: the Ratio of Annual Cumulative Fatigue Damage of Case 2380 of Total, $1 \times \omega$ and $3 \times \omega$ Band Pass

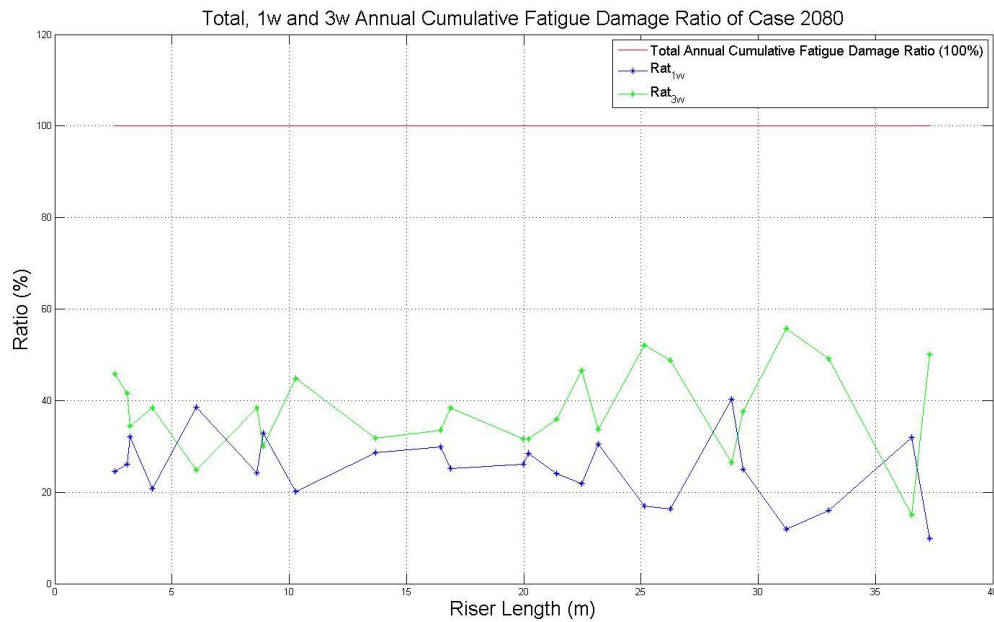


Figure 6.25: the Ratio of Annual Cumulative Fatigue Damage of Case 2080 of Total, $1 \times \omega$ and $3 \times \omega$ Band Pass

See the figures 6.24 and 6.25 above, for shear flow cases, we can see that when the velocity is large (close to the left part of the riser), the ratio of $1 \times \omega$ cumulative damage is dominant but decreasing, while the ratio of $3 \times \omega$ annual cumulative fatigue damage is increasing, when the velocity is small (close to the right part of the riser), the ratio of $3 \times \omega$ annual cumulative fatigue damage is dominant.

For uniform cases, things are different. The ratio of $3 \times \omega$ annual cumulative fatigue damage is dominant for most part of the riser, especially in the middle part of the riser. For some cases like case 2050, $3w$ cumulative damage is dominant almost along the whole riser.

From the results we know that the $3 \times \omega$ also gives a large contribution to the fatigue damage to the riser, especially for the uniform flow cases, which can't be neglected.

6.3.7 Contour plots for the Ratio of Fatigue Damage of Total, $1 \times \omega$ and $3 \times \omega$ Frequency Component

Since we got the results for the $Rat_{1 \times \omega}$ along the riser for 44 cases (appendix B.1 and B.2), we can then make the contour plots for shear flow cases and uniform flow cases separately. Since VIVANA only use the data after $1 \times \omega$ filtering, in this part we only focus on the $Rat_{1 \times \omega}$ and make the contour plots.

For shear flow cases, we use the results of the 22 cases, and make the contour plots, see the figure 6.26, 6.27 below:

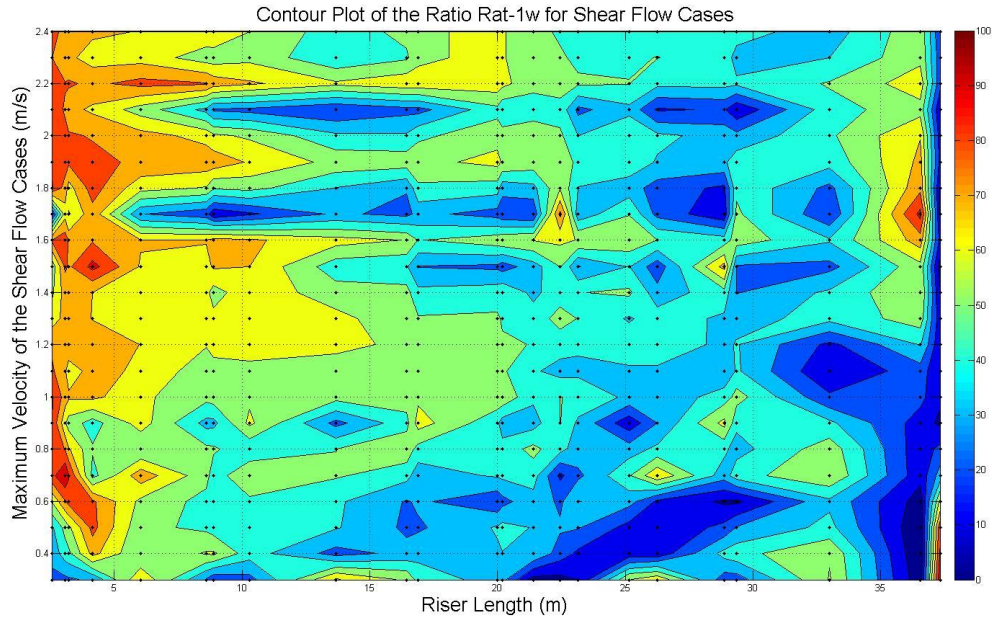


Figure 6.26: Contour Plot of Rat_{1w} for 22 Shear Flow Cases

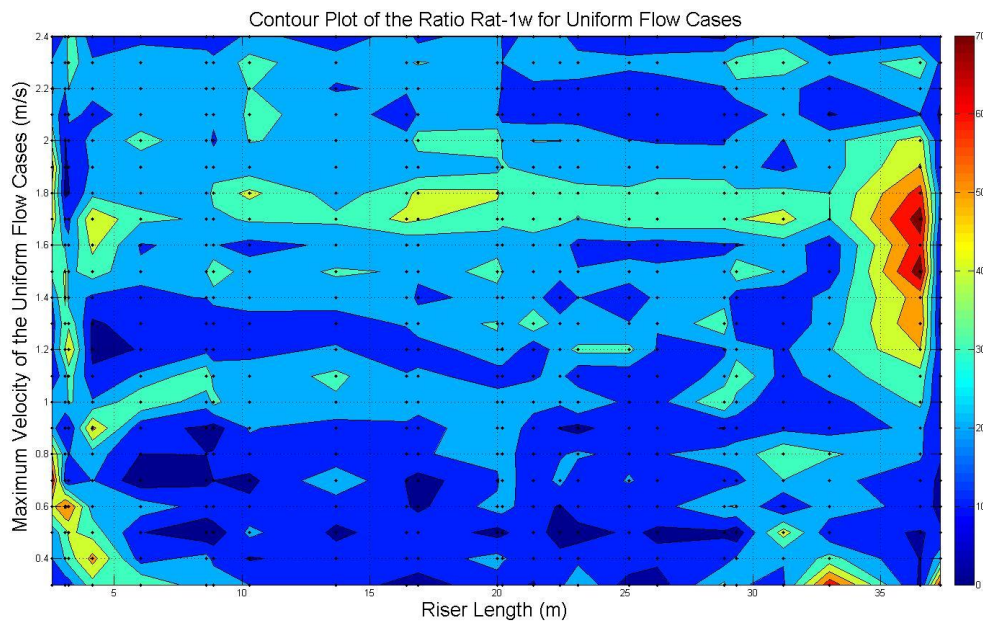


Figure 6.27: Contour Plot of Rat_{1w} for 22 Uniform flow Cases

When making the contour plots for shear flow cases, we neglect the data at the No.21 strain gauge of the riser in order to avoid mistakes.

See from the contour plots 6.26 and 6.27 above, we can find that for shear flow cases, the larger the current speed of the riser, the large Rat_{1w} is.

For different cases, with the increasing of the maximum velocity of the current speed, the Rat_{1w} at the same location of the riser also increases. But there are two cases which seems

different, for the cases with maximum velocity 2.1m/s and 1.7m/s, the increasing of the $Rat_{1\times\omega}$ along the riser are not obvious.

For the uniform flow cases, the $Rat_{1\times\omega}$ seems quite stable along the riser, and the $Rat_{1\times\omega}$ close to both ends are a little larger than the $Rat_{1\times\omega}$ in the middle of the riser. And with the increasing of the maximum velocity of different cases, the $Rat_{1\times\omega}$ at the same location of the riser also increases.

6.3.8 Average Value and Standard Deviation of the Ratio of Fatigue Damage of Total, $1\times\omega$ and $3\times\omega$ Frequency Component

Then we can plot the average value and standard deviation of $Rat_{1\times\omega}$ for shear flow cases and for uniform flow cases separately, remember to get rid of the error values of strain gauge No. 21 from case 2420 to case 2470. See figures 6.28 to 6.29 below:

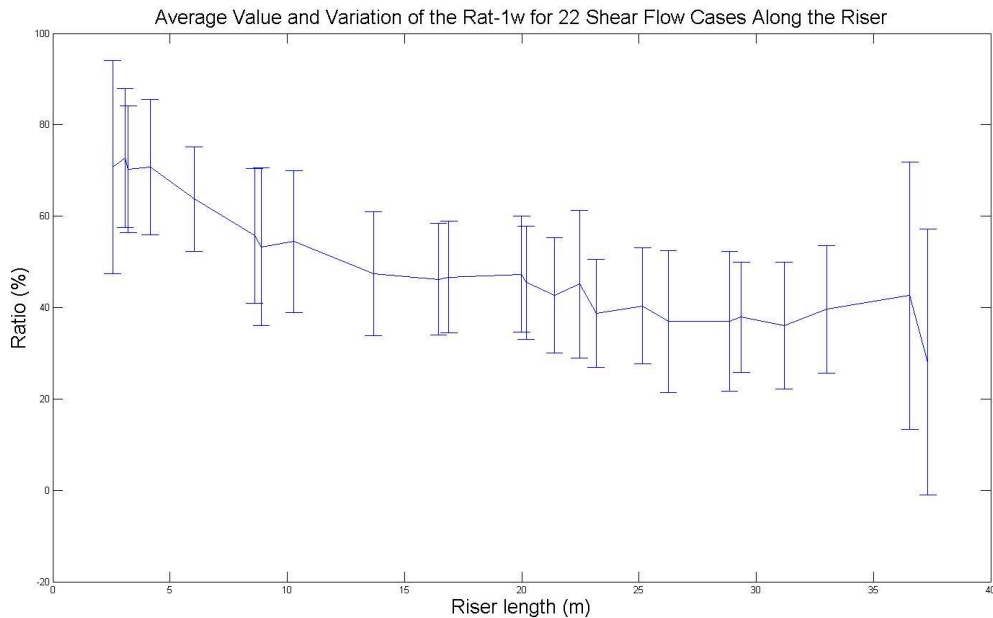


Figure 6.28: the Average Value and Standard Deviation of $Rat_{1\times\omega}$ of 22 Shear Flow Cases

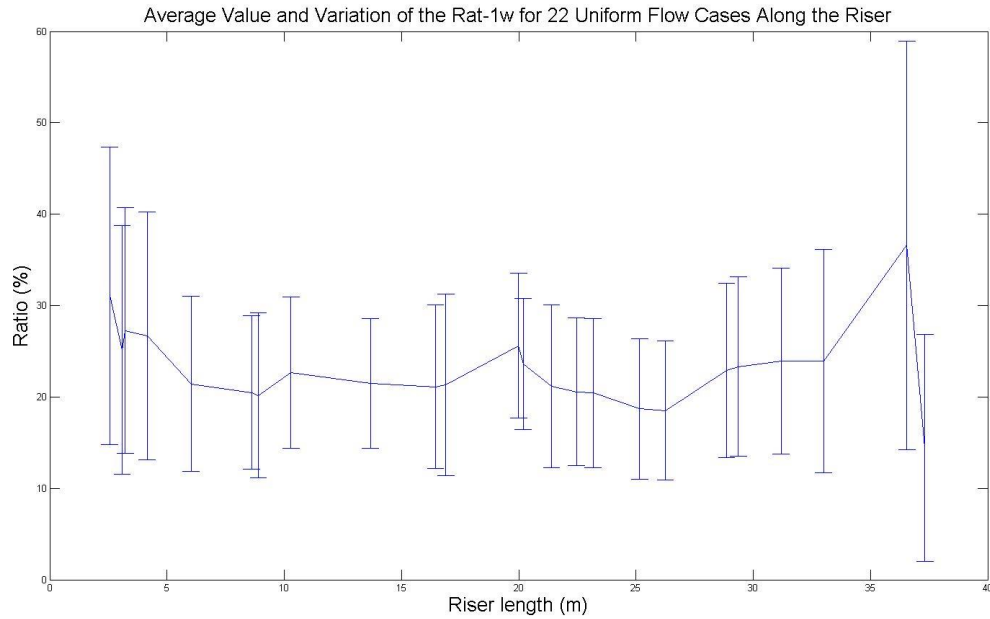


Figure 6.29: the Average Value and Standard Deviation of $Rat_{1 \times \omega}$ of 22 Uniform Flow Cases

See from figure 6.28 and 6.29, we can see that for shear flow cases, the v takes up about 30% to 70% of the total annual cumulative fatigue damage, the larger the velocity, the larger the $Rat_{1 \times \omega}$, and the standard deviation is about 40% along the riser.

For uniform flow cases, we can see that the $Rat_{1 \times \omega}$ takes up about 20% to 35% of the total annual cumulative fatigue damage, and the standard deviation is about 20%.

Since VIVANA uses the $1 \times \omega$ band pass method to do the fatigue analysis, we should multiply a safety factor ranges from 1.43 to 3.3 for shear flow cases, and 2.86 to 5 for uniform cases to get the real fatigue damage.

6.3.9 Influence of Different SN Curve on the Results of the Fatigue analysis

In order to see the influence of different SN curves on the fatigue analysis results, here we use a new SN curve. See table 6.10 below:

Table 6.10: New SN Curve Used for Fatigue Analysis

Parameter	Value
S-N curve	DNV F2 single slope $\log \bar{a} = 15.01$; $m = 4.0$
SCFs	1.0 everywhere
Notes:	
1. $\log(N) = \log \bar{a} - m \cdot \log(s)$, where	
N is the predicted number of cycles to failure under stress range S (Mpa)	
m is the inverse slope of the SN curve	
log used in the notation is log to the base 10	

Using the new SN curve above, we can get a totally new result of the annual cumulative fatigue damage for total, $1 \times \omega$ annual cumulative fatigue damage and $3 \times \omega$ annual cumulative fatigue damage for the 44 cases.

Similarly, we can calculate the can $Rat_{1 \times \omega}$ along the riser for all the cases. Make the new contour plots for the shear flow and uniform flow cases separately. See figures 6.30 and 6.31 below:

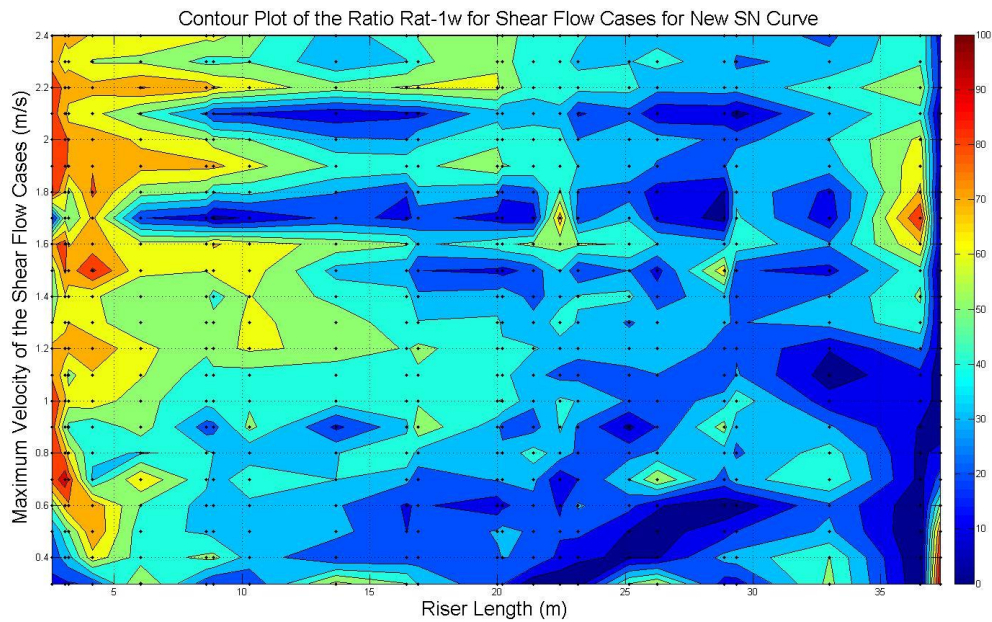


Figure 6.30: Contour Plot of $Rat_{1 \times \omega}$ of 22 Shear Flow Cases of New SN Curve

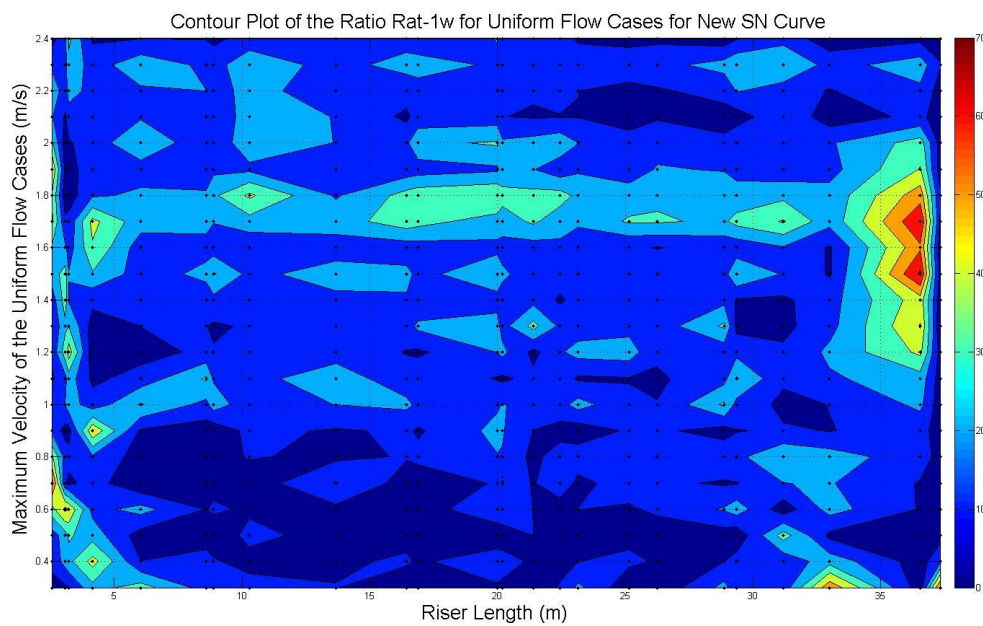


Figure 6.31: Contour Plot of $Rat_{1 \times \omega}$ of 22 Uniform Flow Cases of New SN Curve

We can find that when we use the new SN curve, the $Rat_{1 \times \omega}$ are decreasing along the risers.

Then we can plot the average value and standard deviation of $Rat_{1 \times \omega}$ for shear flow cases and for uniform flow cases separately, see figures 6.32 to 6.33 below:

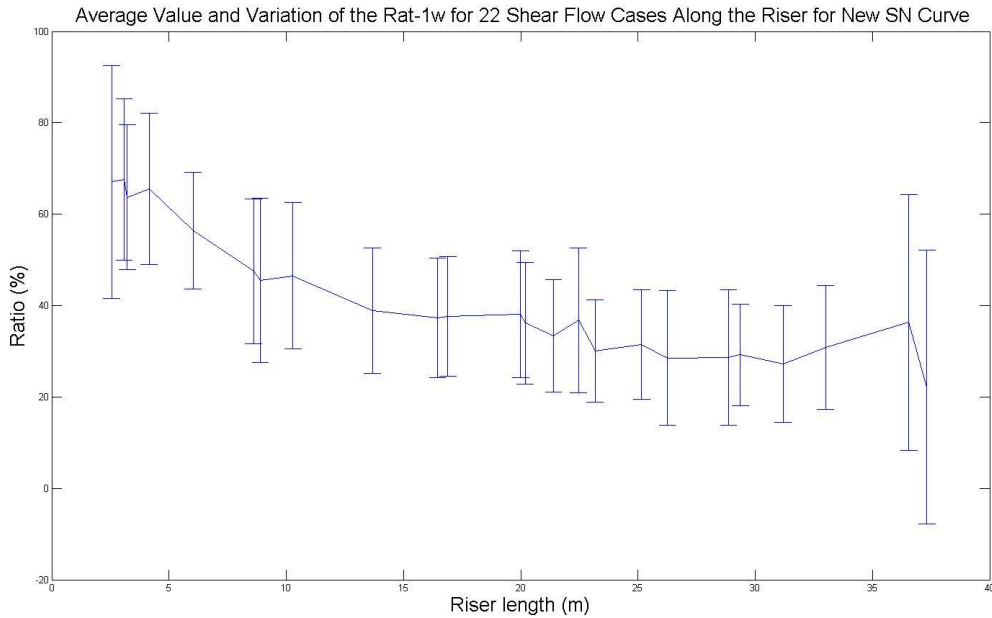


Figure 6.32: the Average Value and Standard Deviation of $Rat_{1 \times \omega}$ of 22 Shear Flow Cases of New SN Curve

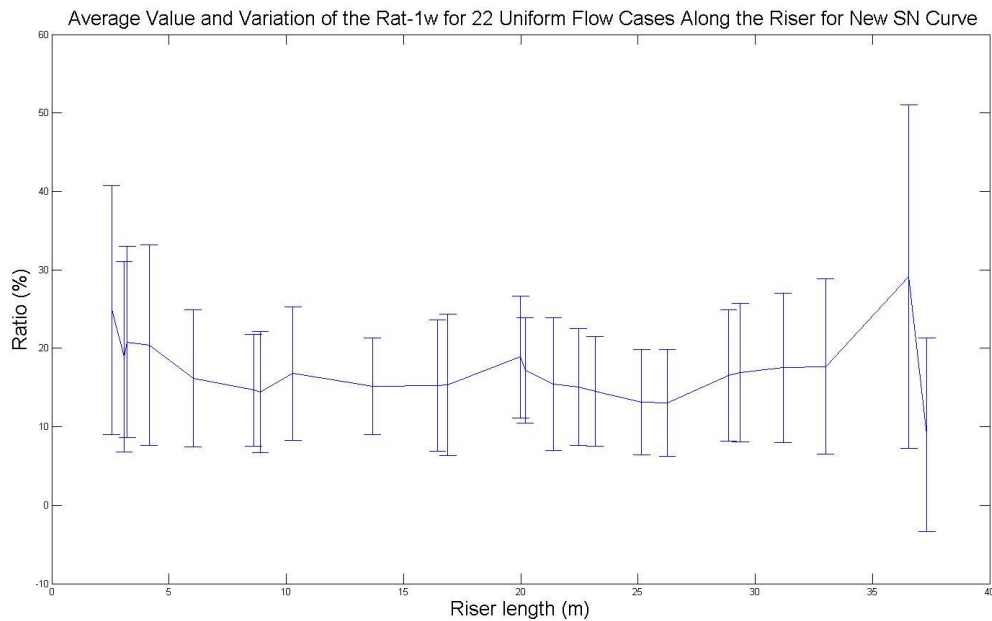


Figure 6.33: the Average Value and Standard Deviation of $Rat_{1 \times \omega}$ of 22 Uniform Flow Cases of New SN Curve

We can find that the average and standard deviation values for the $Rat_{1 \times \omega}$ for the new SN curve is a little lower than that of the old SN curve

See from figure 5.23 to 5.26 we can find that for different SN curve, the contour plot and average value of $Rat_{1\times\omega}$ are a little different from the previous SN curve, $Rat_{1\times\omega}$ becomes lower, for shear flow cases, $Rat_{1\times\omega}$ ranges from 25% to 65%, for uniform flow cases, it ranges from 15% to 30% , but the trend keeps the same.

Although the annual cumulative fatigue damage changes a lot, the ratio changes a little.

6.4 Summary

In this chapter, we analyzed 44 NDP cases including 22 uniform cases and 22 shear flow cases. We pre-process the data to choose the length of the signal we use and get the spectrum of each case to get the dominant frequency and filtered the data in three different ways, the total band pass filtering, the $1\times\omega$ band pass filtering and $3\times\omega$ band pass filtering.

We calculated the non-dimensional amplitude and standard deviation of the stress for one cases, and we can see the $1\times\omega$ band pass filtering doesn't change the amplitude very much, while the $3\times\omega$ band pass filtering changes a lot.

Then we calculated the annual cumulative fatigue damage of the cases, we found the fatigue from the $3\times\omega$ frequency component are as important as those from $1\times\omega$ frequency component. And for the different cases, the ratio of the $1\times\omega$ frequency component fatigue also changes. Even for the same case, the ratio at different position on the riser are different.

Chapter 7

Conclusions

7.1 Summary of Present Work

The present work focuses on using inverse analysis method to estimate hydrodynamic force/coefficient from VIV experiments of bare risers in shear/uniform flow and improves the understanding of CF VIV response and fatigue damage of the risers .

We used the inverse analysis method based on optimal control theory, and use this method on the data obtained from NDP tests of sheared flow and uniform flow cases separately. For the sheared flow case, we made the contour plot of the excitation coefficient and added mass coefficient and make comparison with the results from rotating rig tests. For the uniform flow case, we present the relation between excitation coefficient and non-dimensional amplitude and make comparison with the excitation coefficient model used in VIVANA. We found by using the inverse analysis method we can get the force coefficients easily. And the accuracy is also good in the excitation frequency range.

Then we compare the excitation coefficients from inverse analysis with the results from the damping model used in VIVANA-the Venugopal's damping model, we found the excitation coefficients outside the excitation frequency range will have large uncertainties which the Venugopal's damping model gave more reasonable results.

Then we analyzed 44 NDP tests including shear flow cases and uniform flow cases to calculate the annual cumulative fatigue damage. We find the influence on the displacements and the standard deviation of stress along the riser for total, $1 \times \omega$ and $3 \times \omega$ frequency. Then we found the the $1 \times \omega$ and $3 \times \omega$ fatigue damage all contribute to the total fatigue damage a lot. And the we found the parameters which can be used to get the total fatigue damage from the $1 \times \omega$ fatigue damage. For the different cases, the ratio of the $1 \times \omega$ frequency component fatigue also changes. Even for the same case, the ratio at different position on the riser are different.

7.2 Recommendation of Future Work

Improved inverse analysis algorithm: Based on the experience from the present work, the following recommendations are proposed for future work:

In the inverse analysis part, we just use two cases, one for shear flow and the other for uniform flow. In the future we should use more cases.

Improved modeling of the force coefficient database: From the inverse analysis of the uniform flow case we see that the excitation coefficient and non-dimensional amplitude don't fit the three point model very well, which means the phase between IL and CF displacement may be introduced as an additional parameter. We can also try to identify a general force coefficient model based on the inverse analysis of various test data.

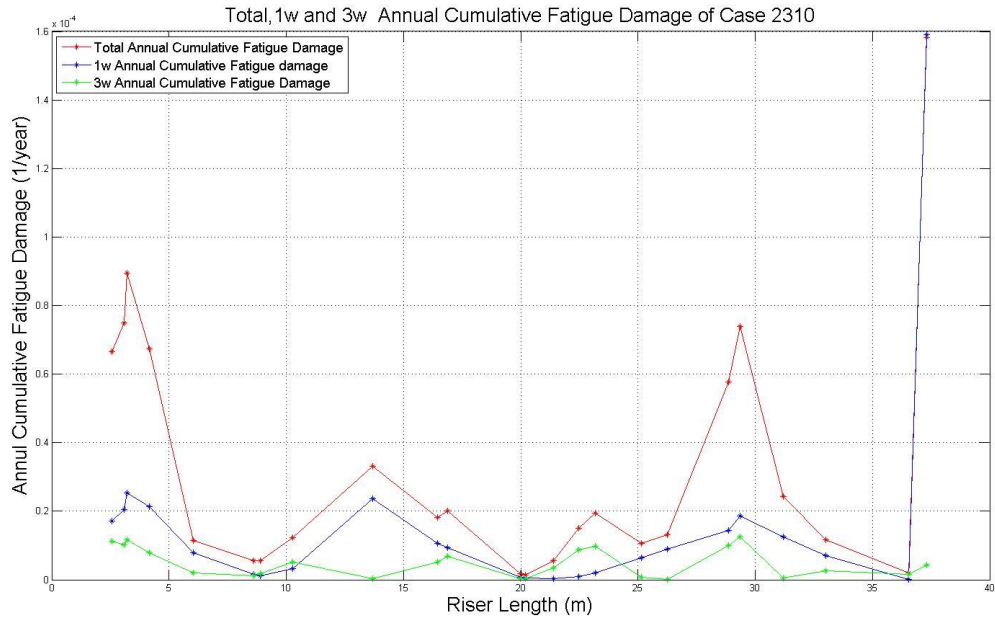
IL force coefficients: The influence of the IL response seems to have a large influence, in the present work, we analyze the CF response individually. While in this project, we can find that in some cases, the IL response is also an important issue. In the future work, we can include the effect of IL response, for example, the non-dimensional IL amplitude and phase angle between the IL and CF response.

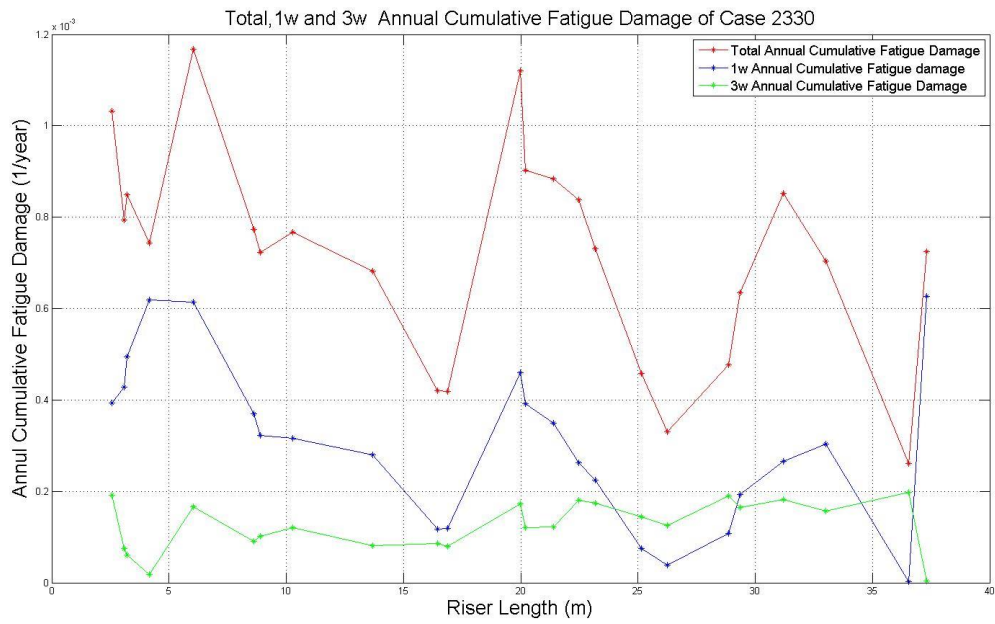
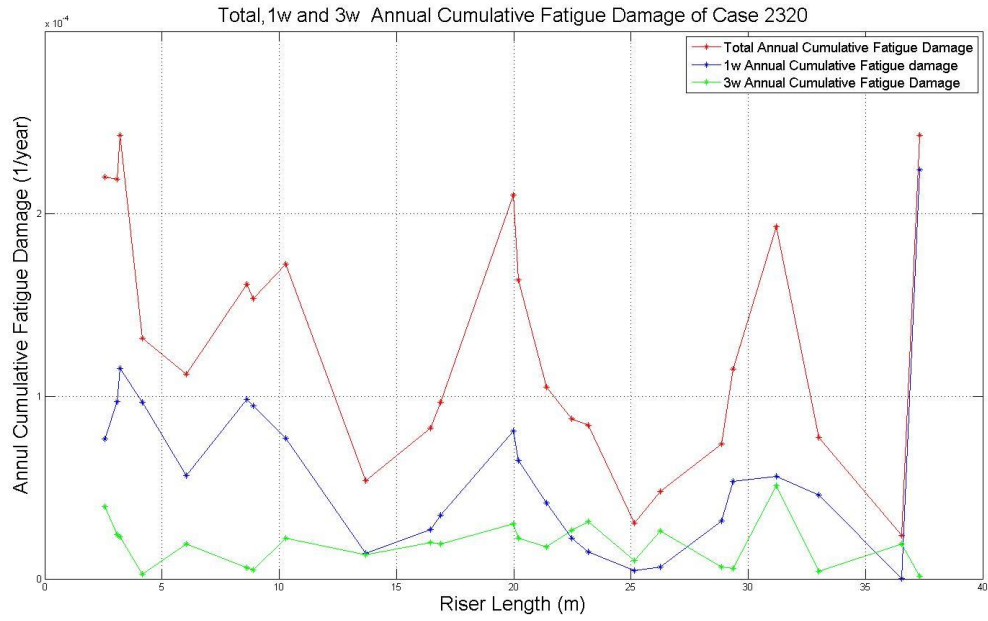
We just analyze the ratio of the annual cumulative fatigue damage between $1 \times \omega$ band pass and total band pass, in the future work, we can also calculate the ratio between $3 \times \omega$ band pass and total band pass to see if there are any similar trends.

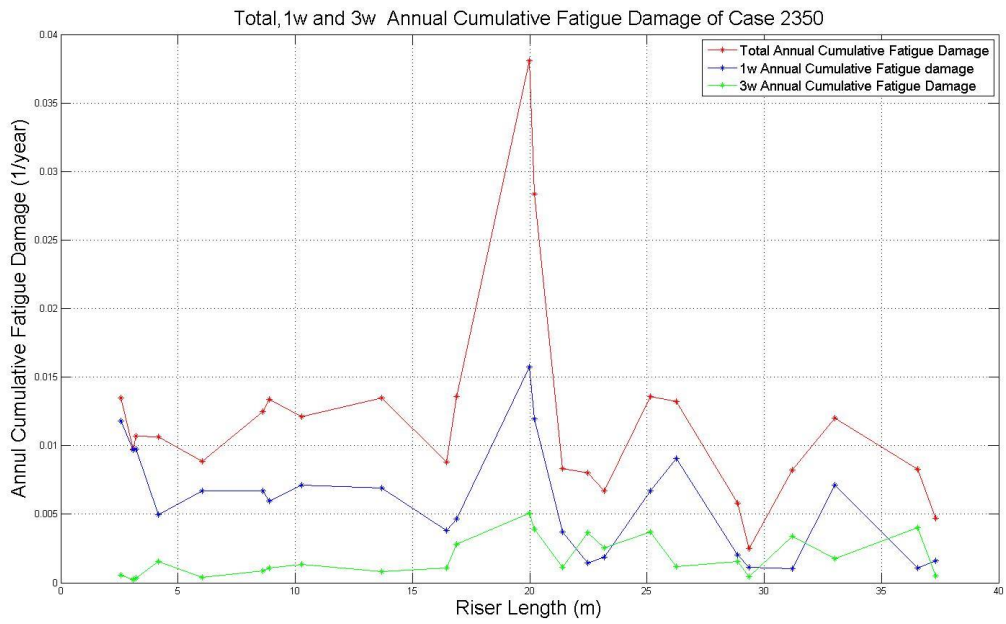
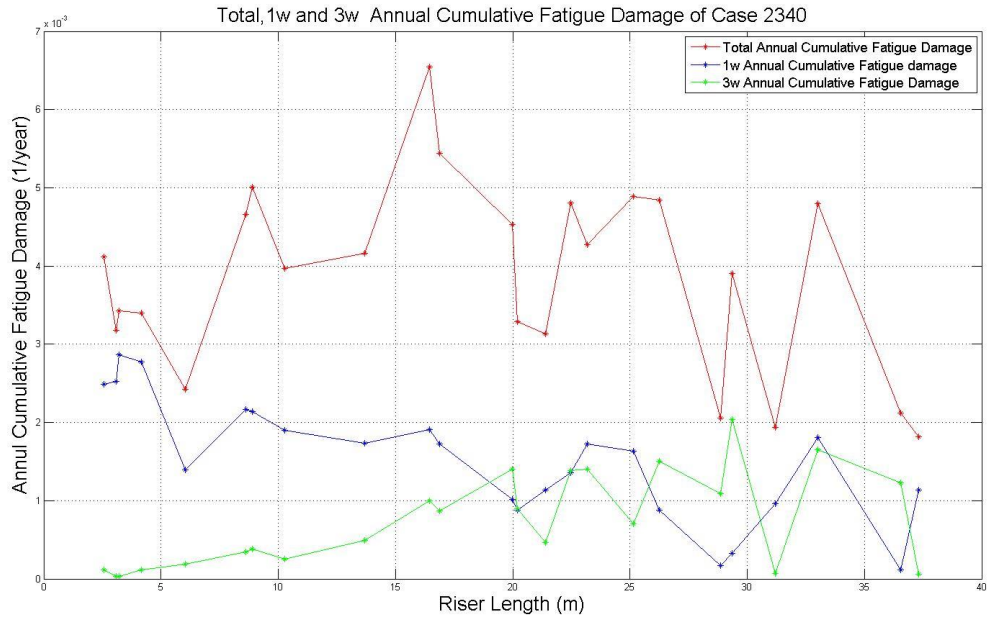
Appendix A

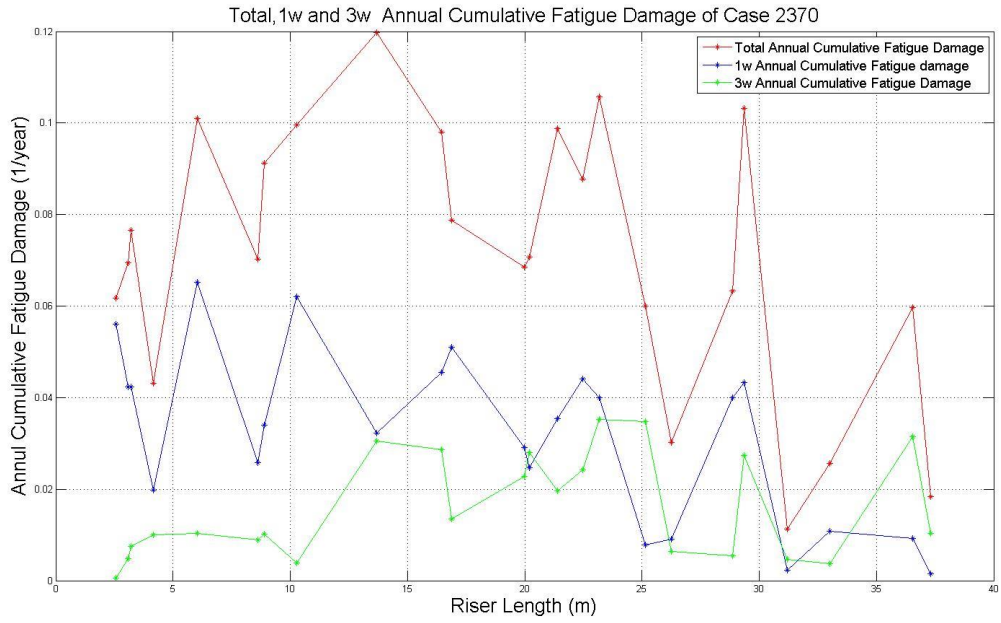
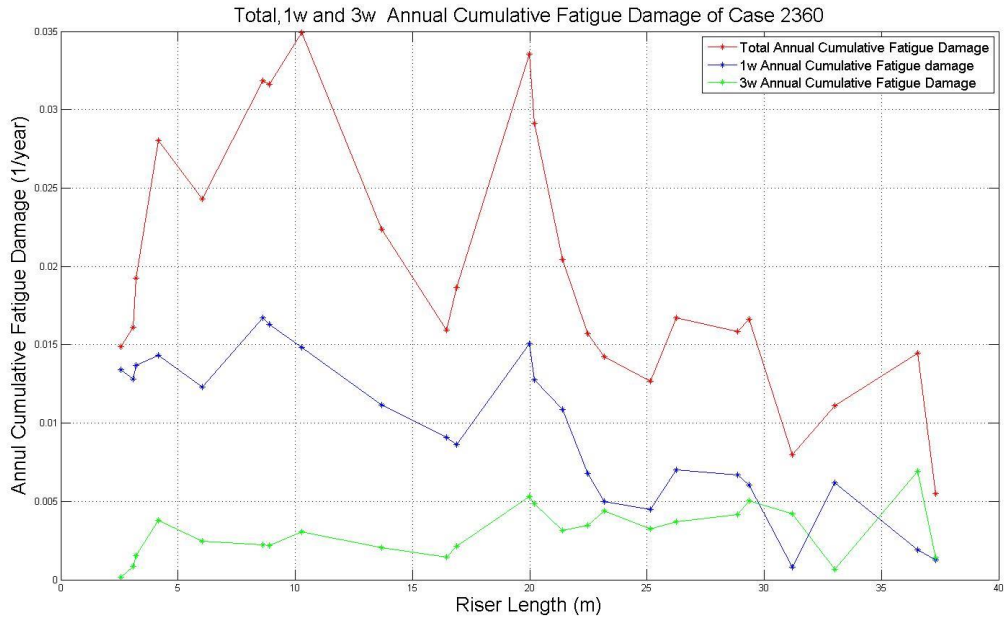
Annual Cumulative Fatigue Damage Results of NDP Tests

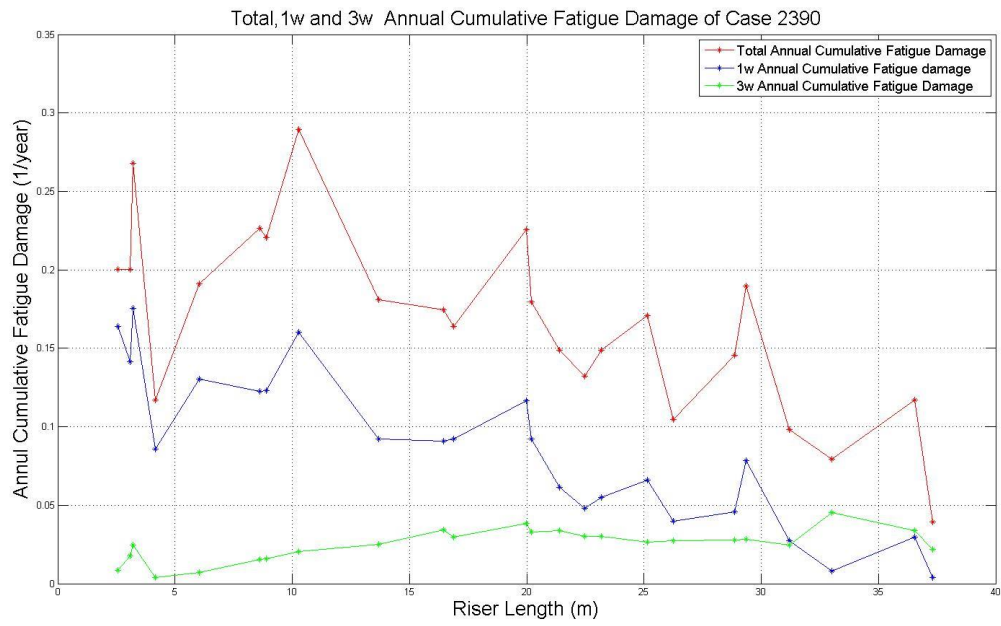
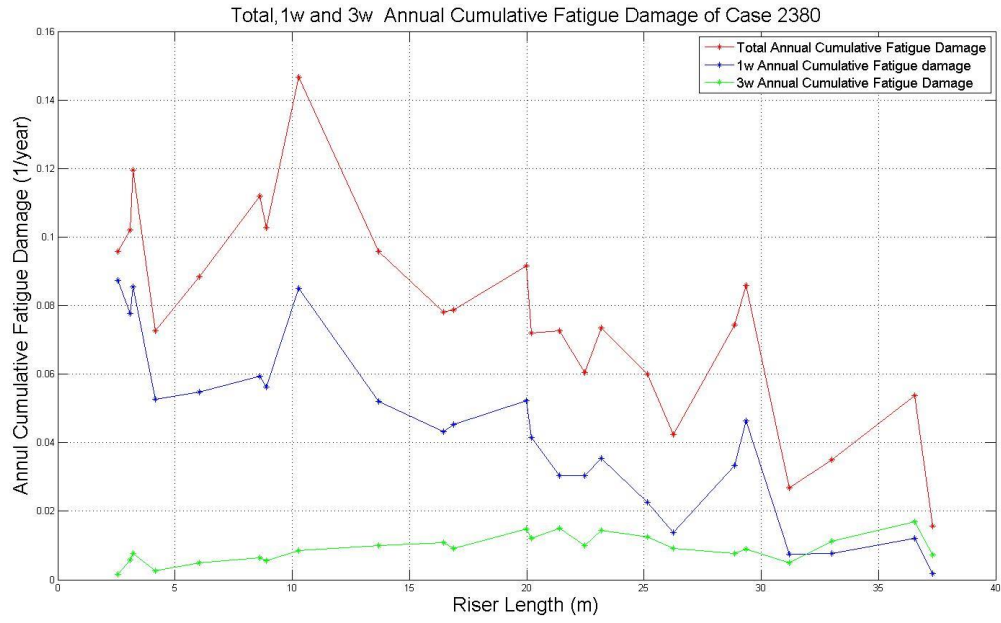
A.1 Comparison of Annual Cumulative Fatigue Damage Results for Total, $1 \times \omega$ and $3 \times \omega$ Frequency Component for Shear Flow Cases

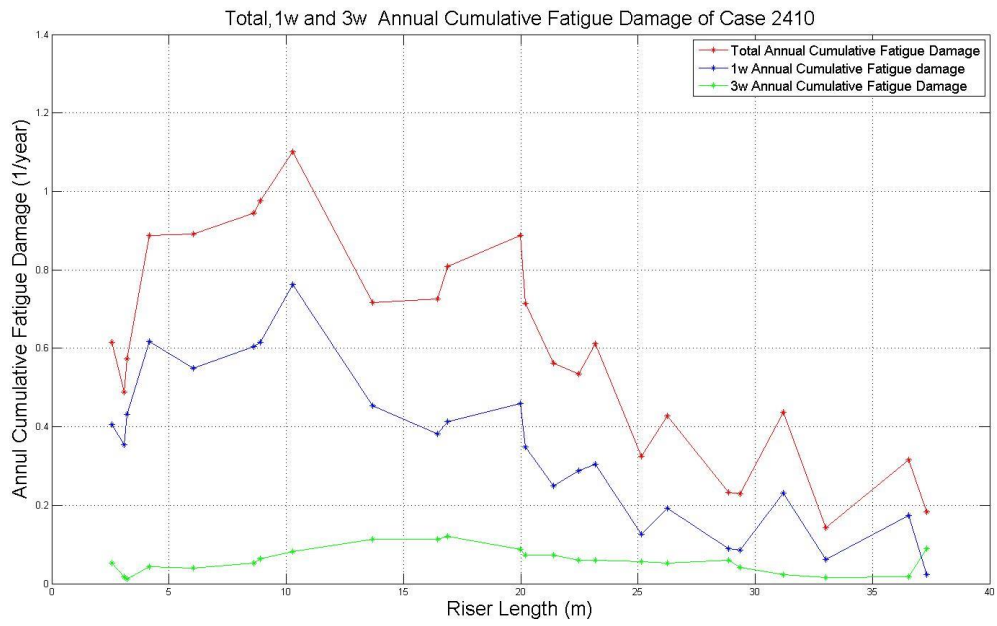
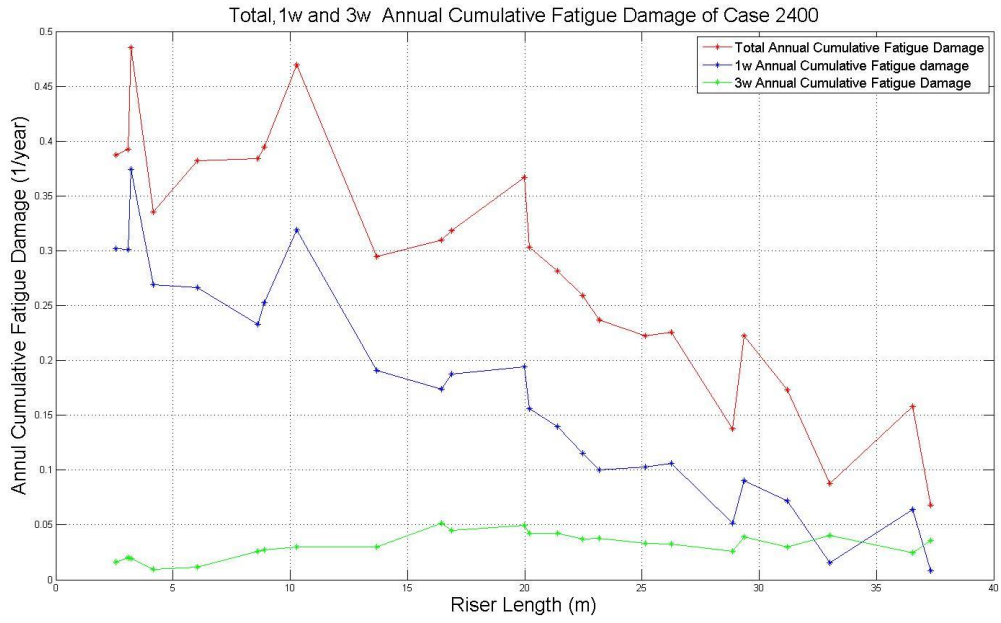


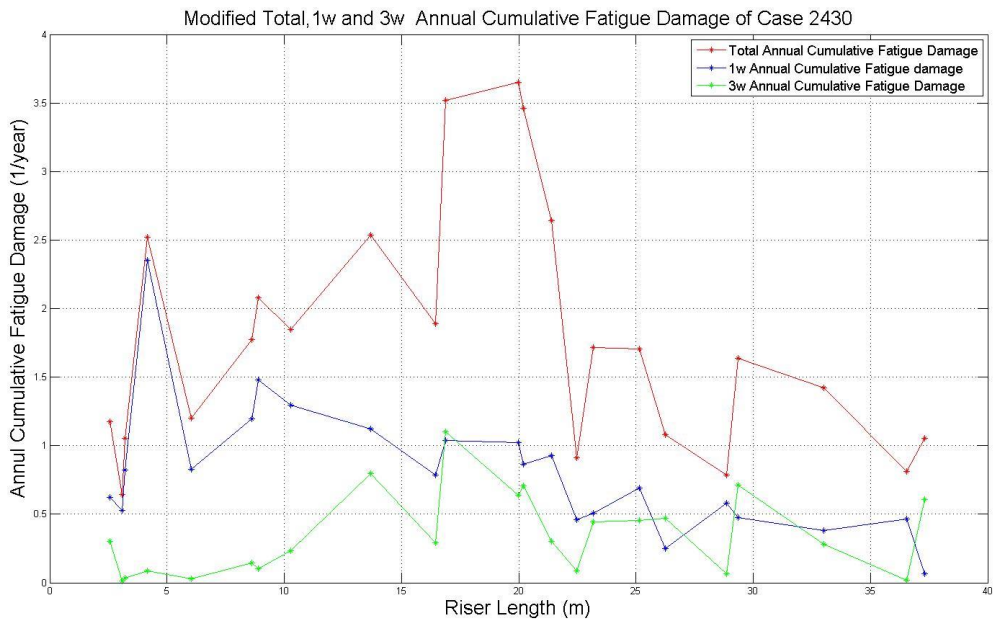
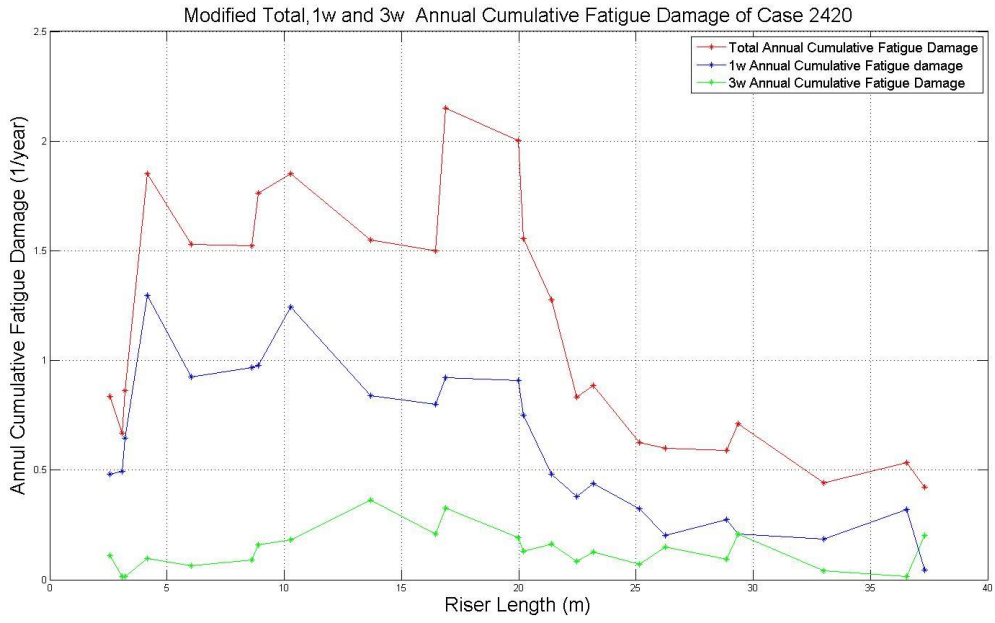


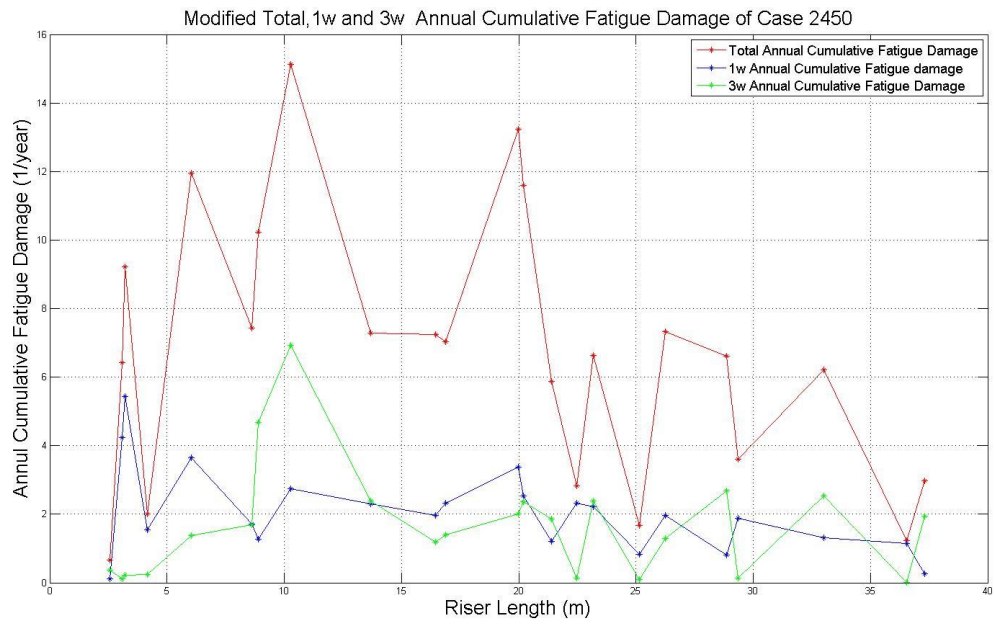
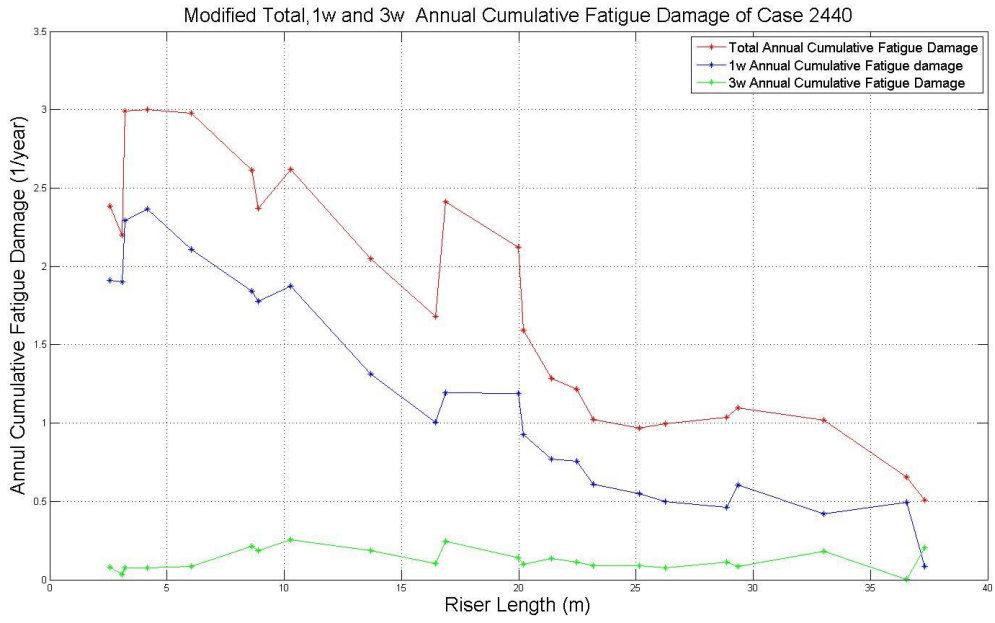


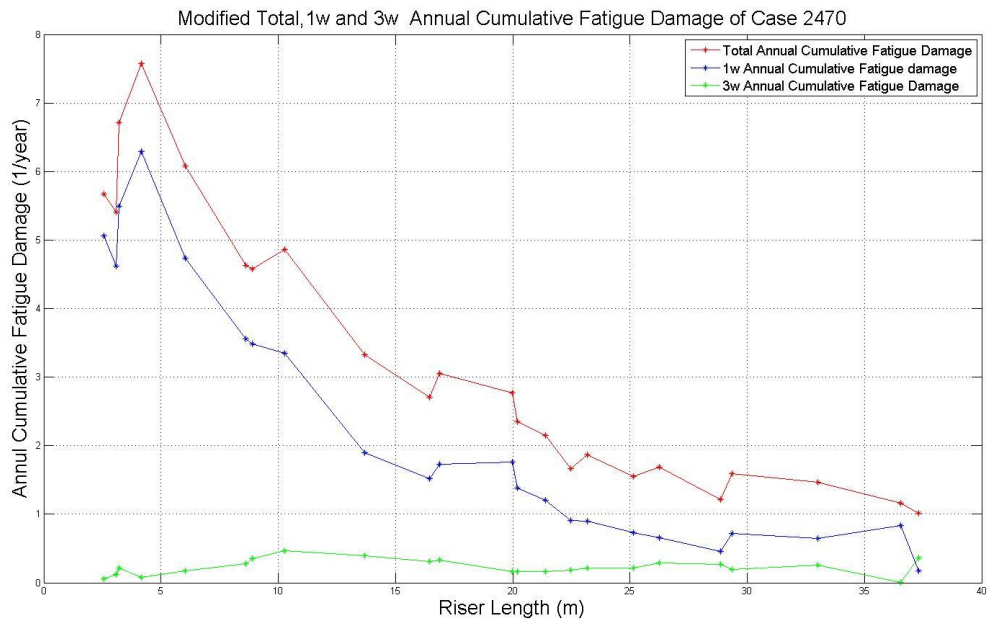
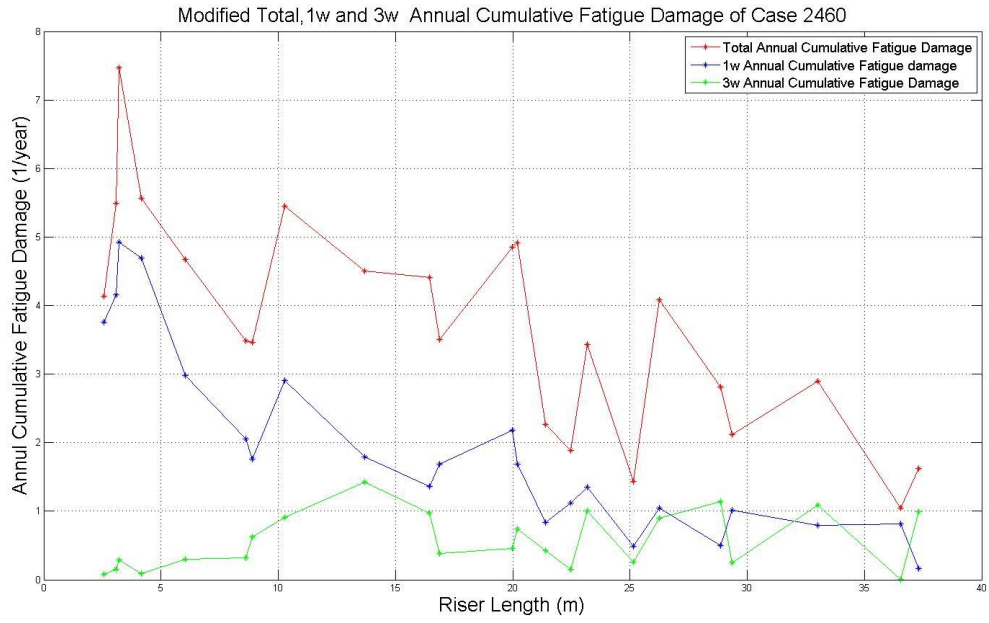


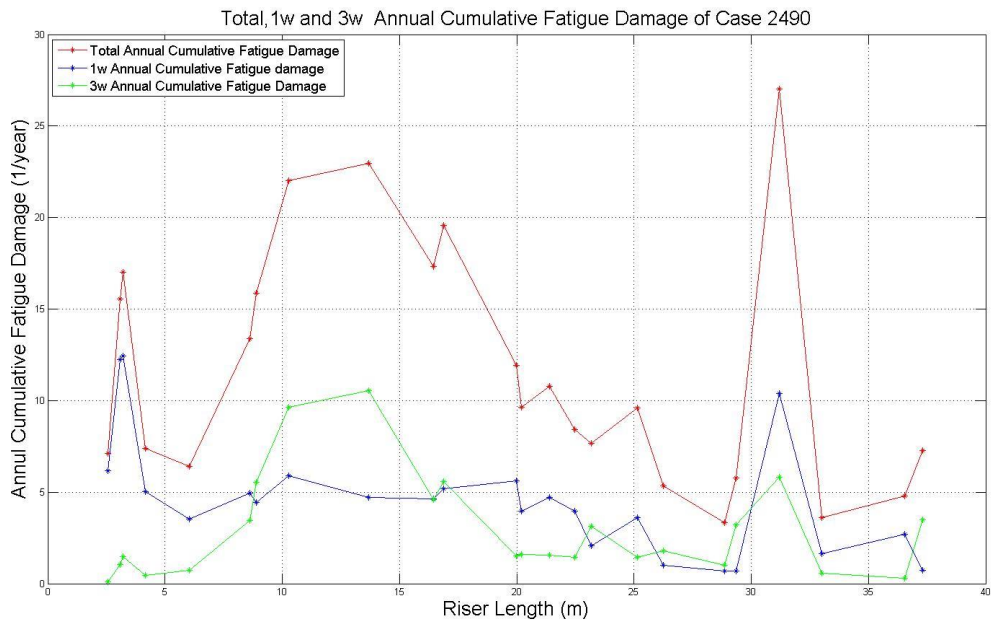
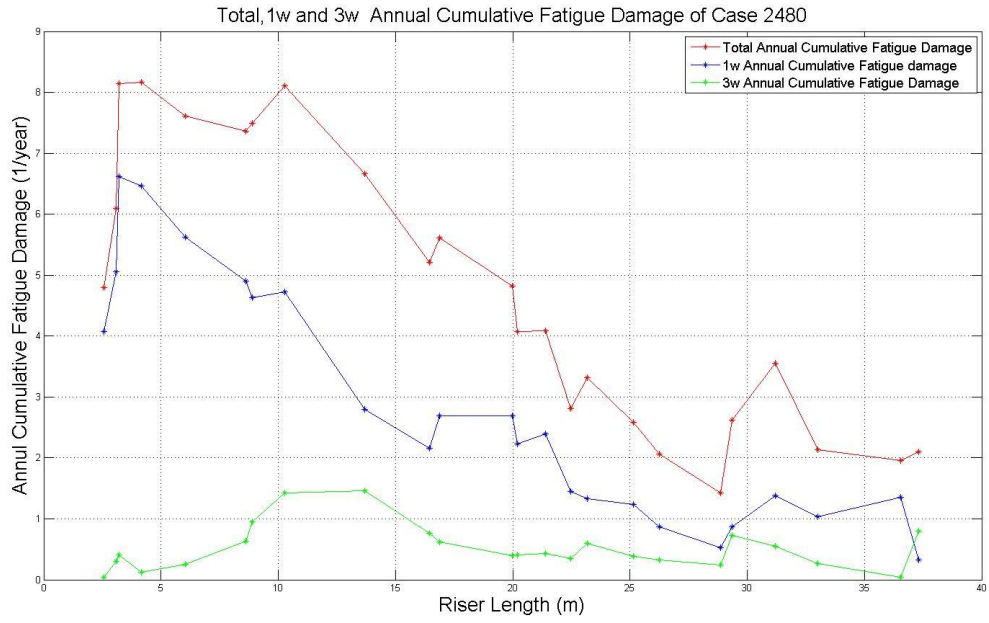


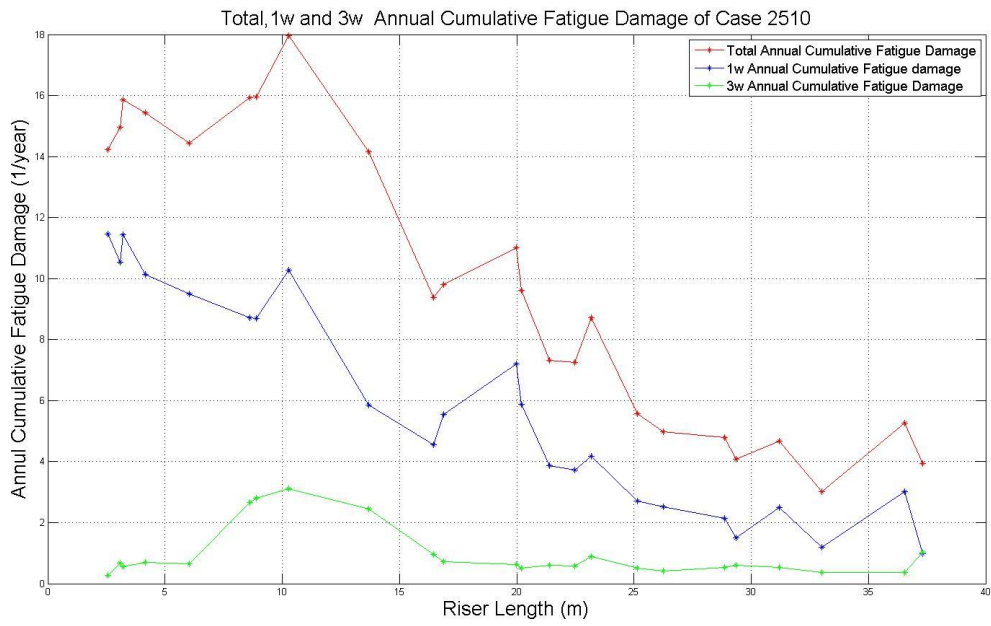
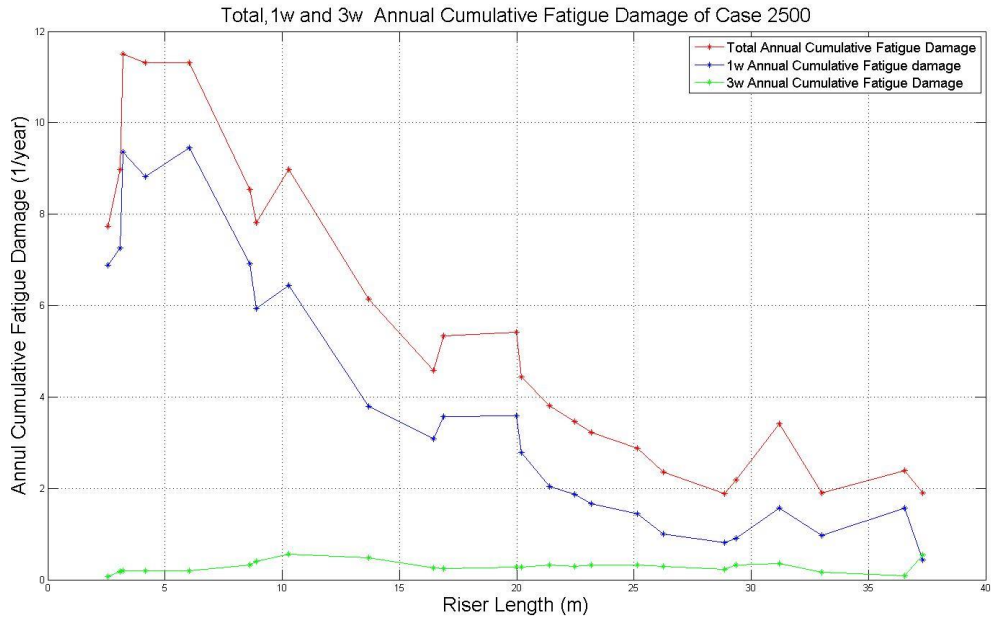


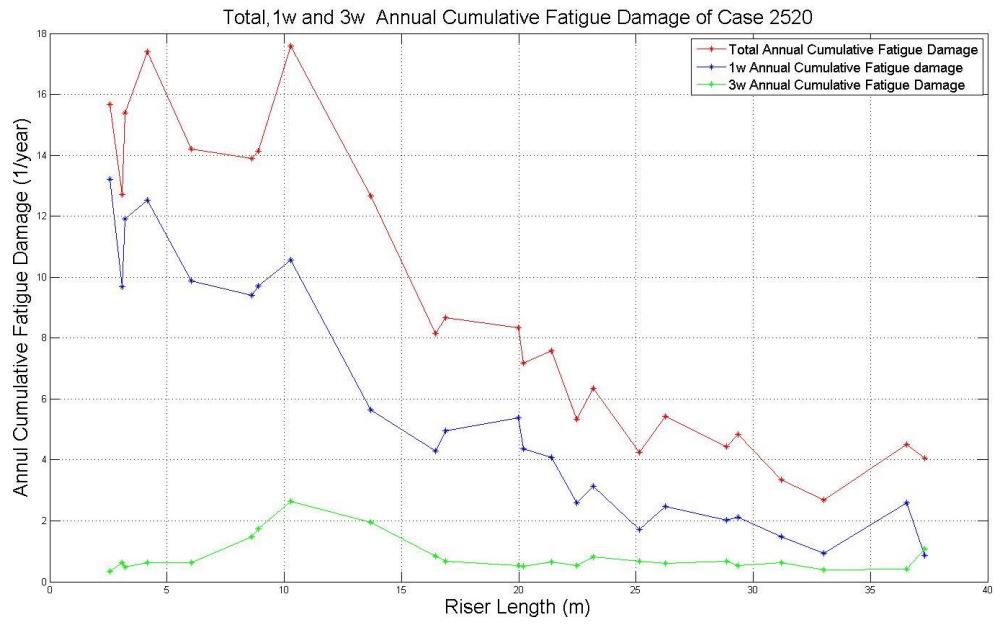




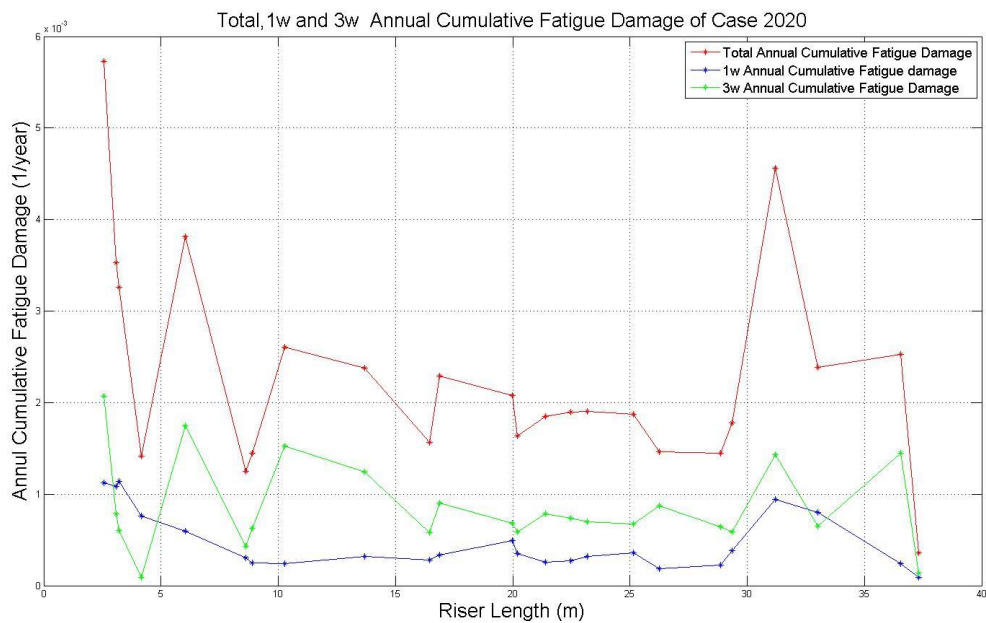
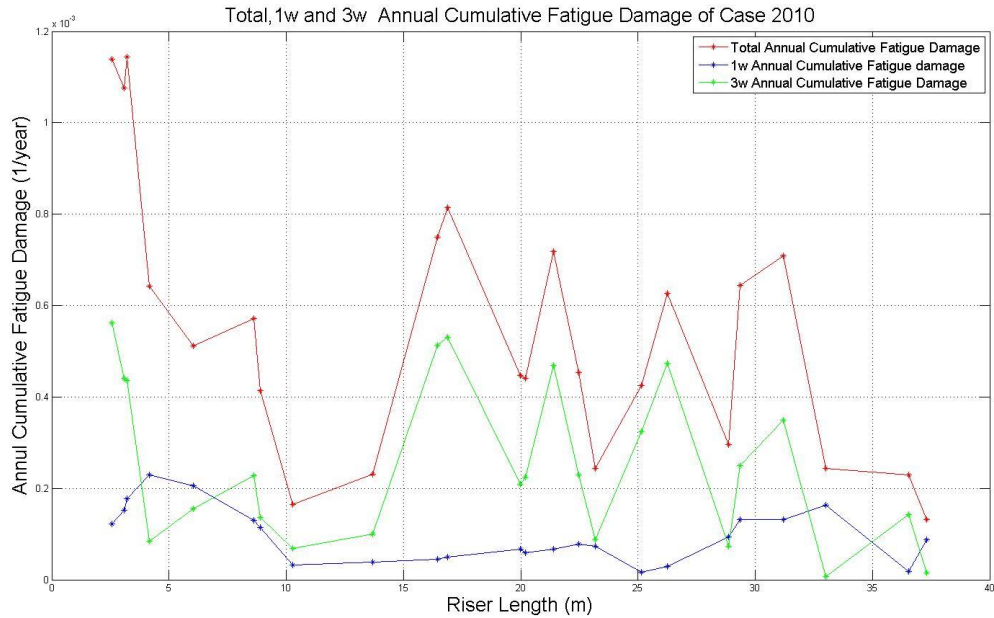


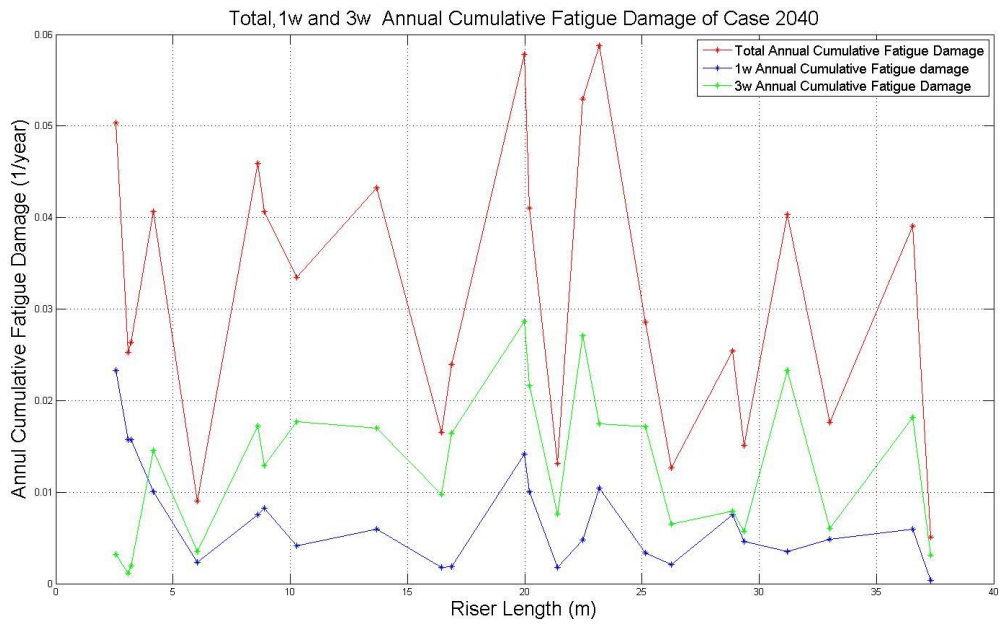
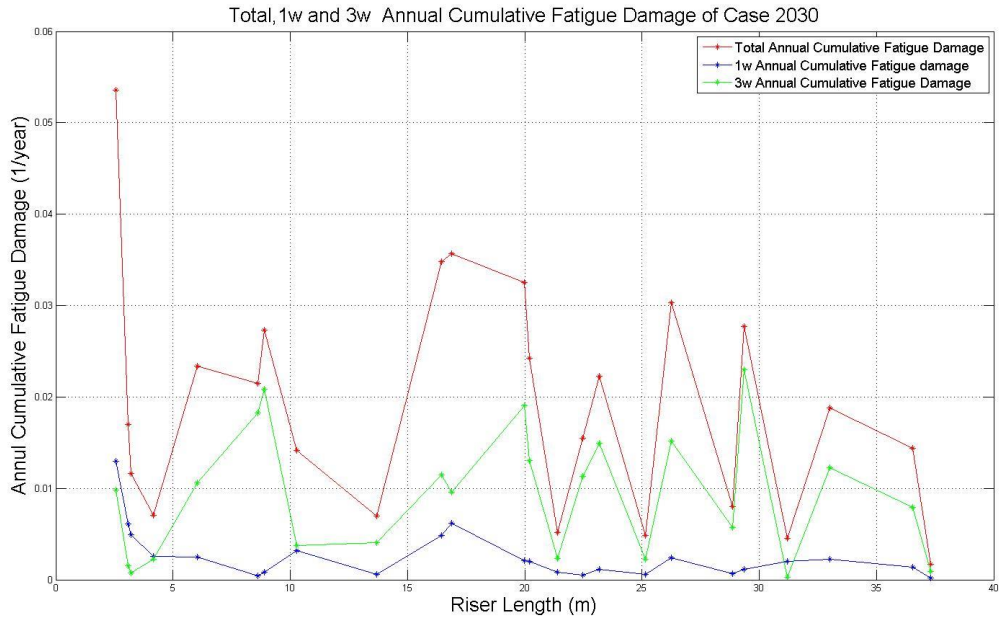


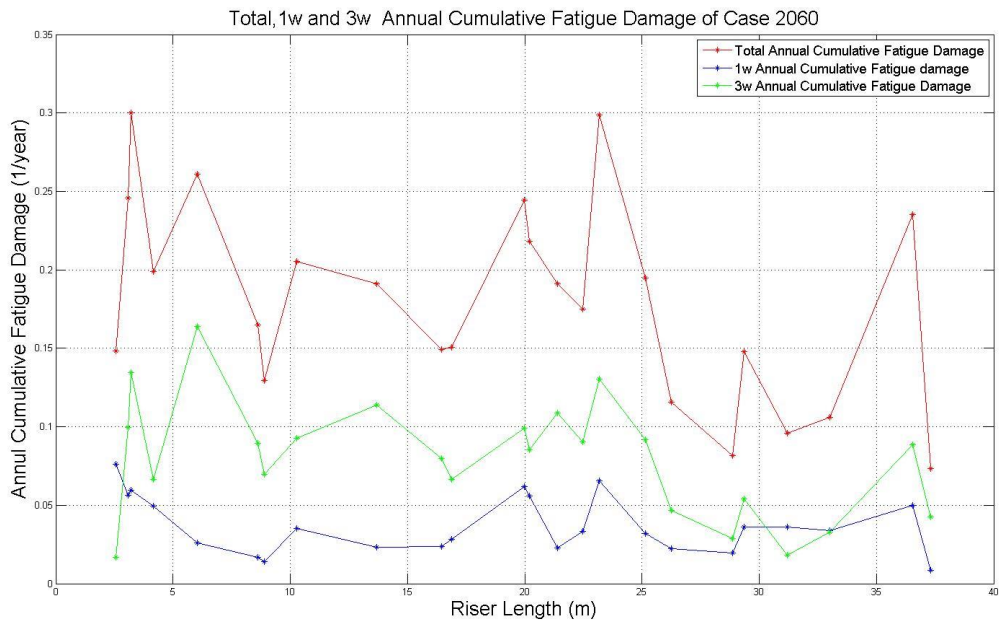
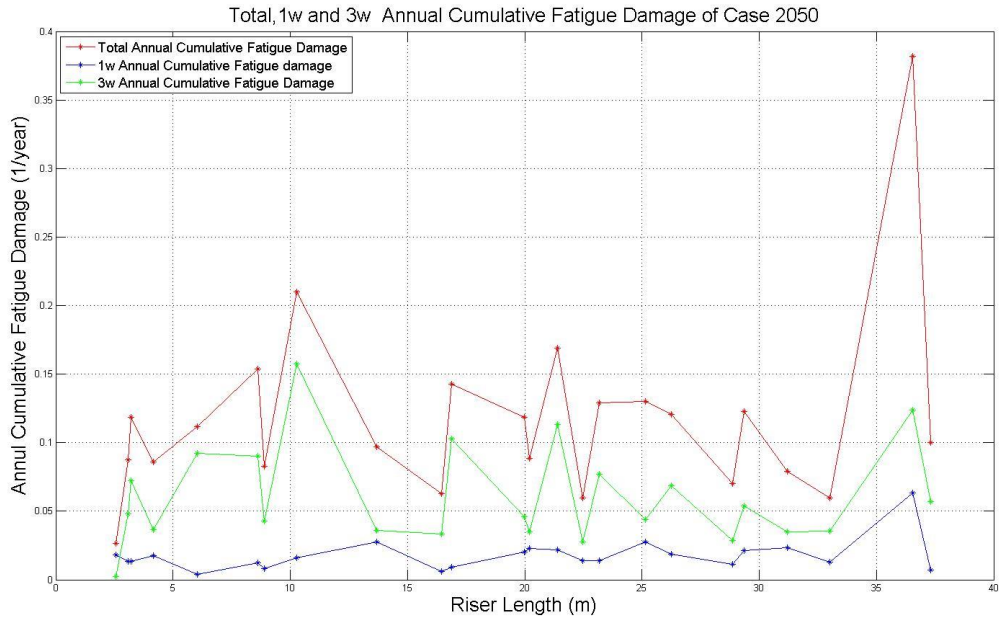


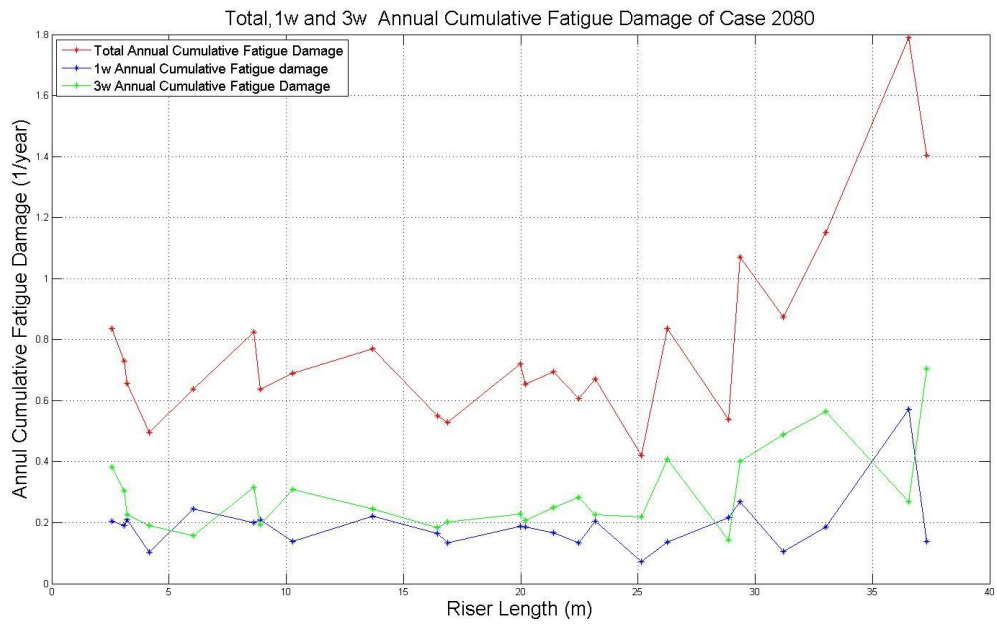
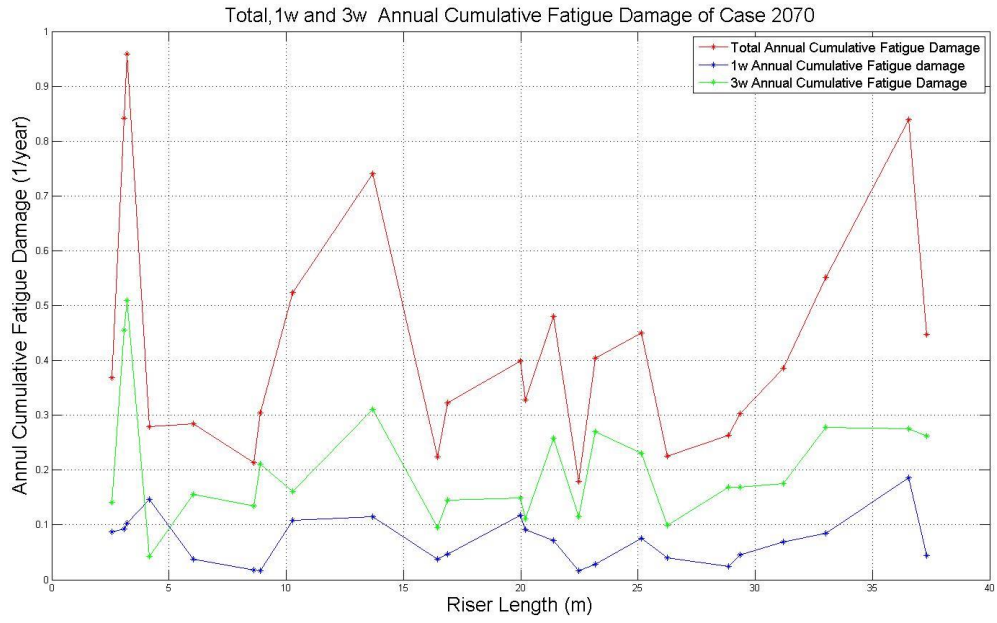


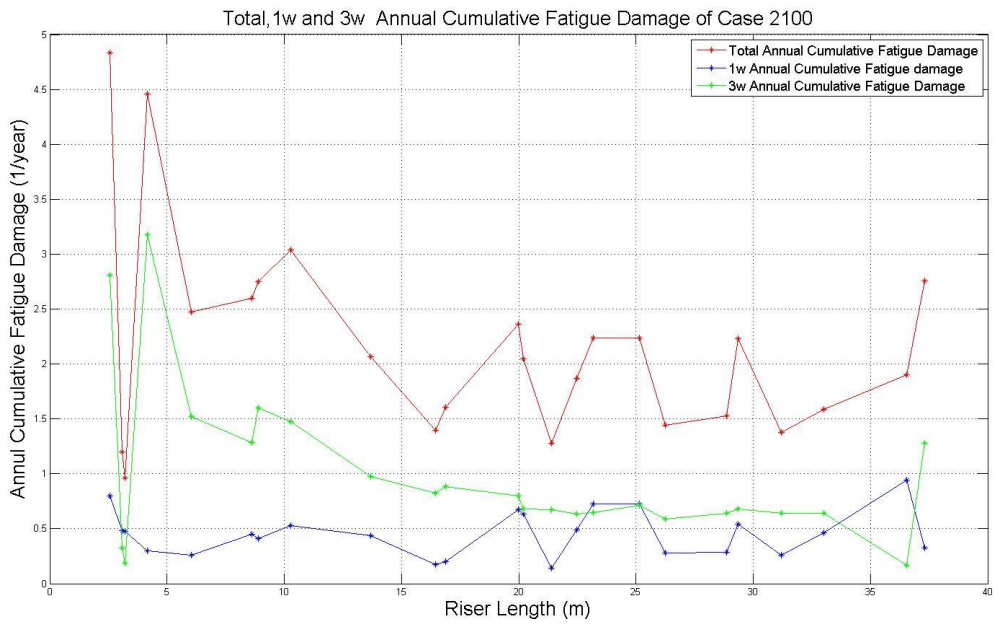
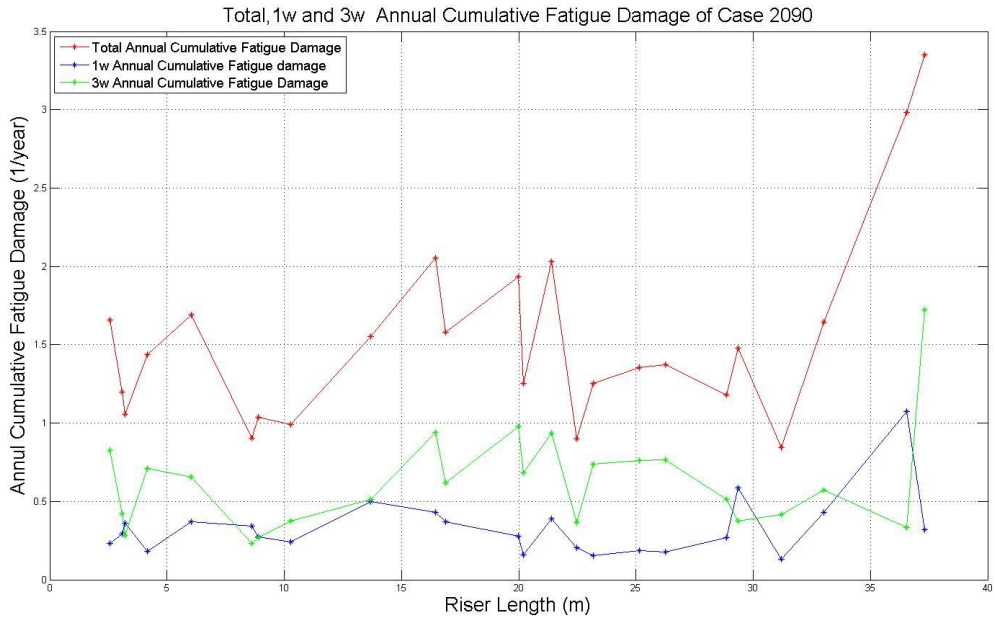
A.2 Comparison of Annual Cumulative Fatigue Damage Results for Total, $1 \times \omega$ and $3 \times \omega$ Frequency Component for Uniform Flow Cases

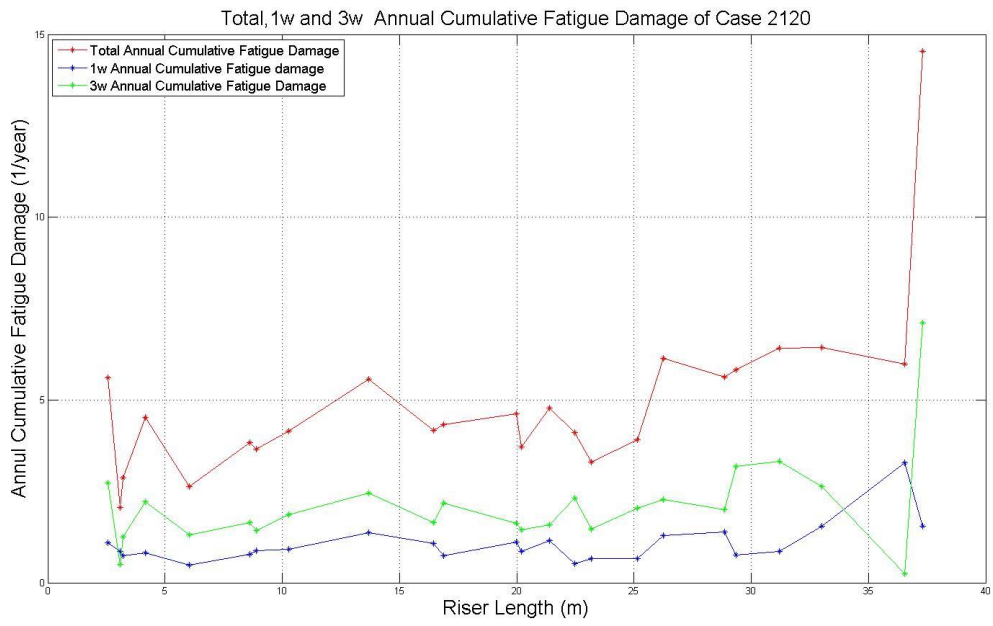
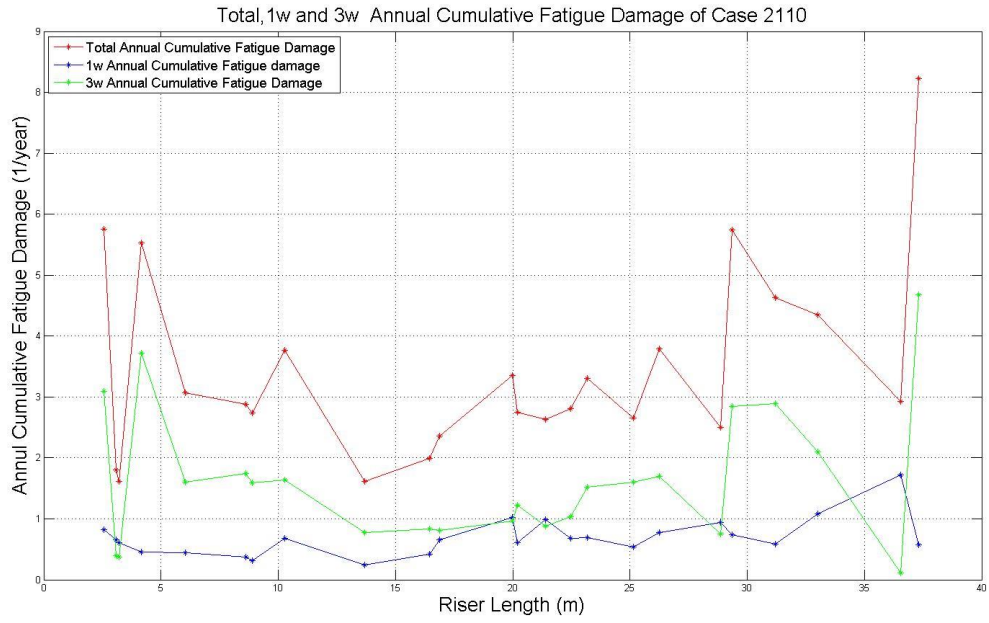


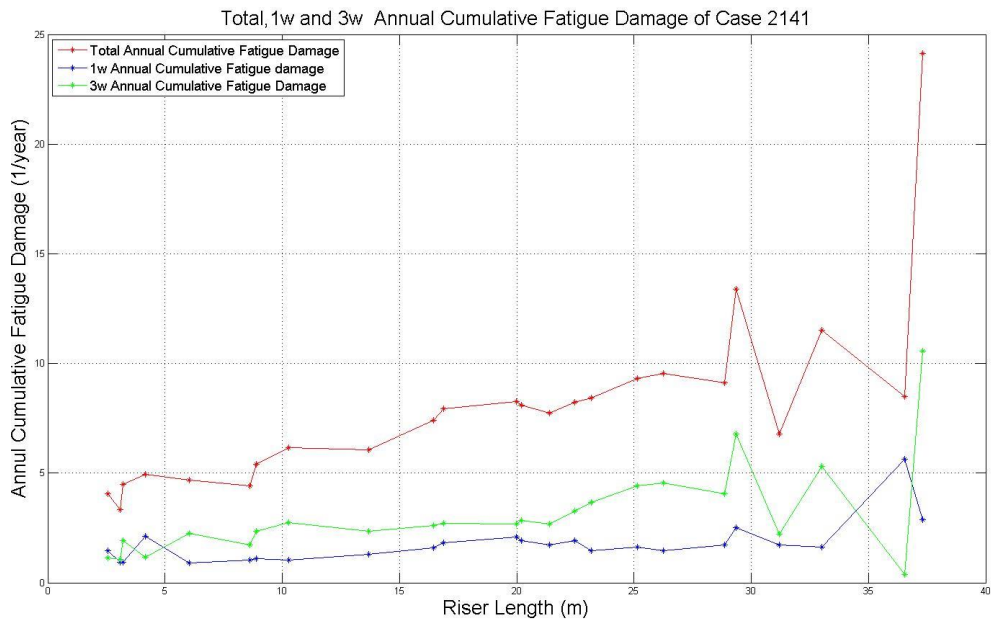
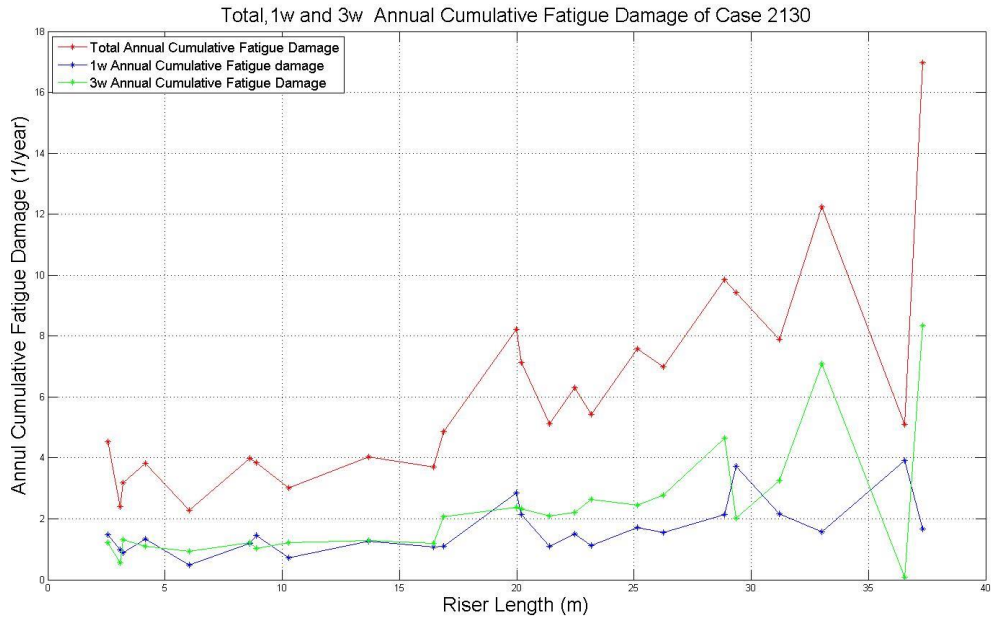


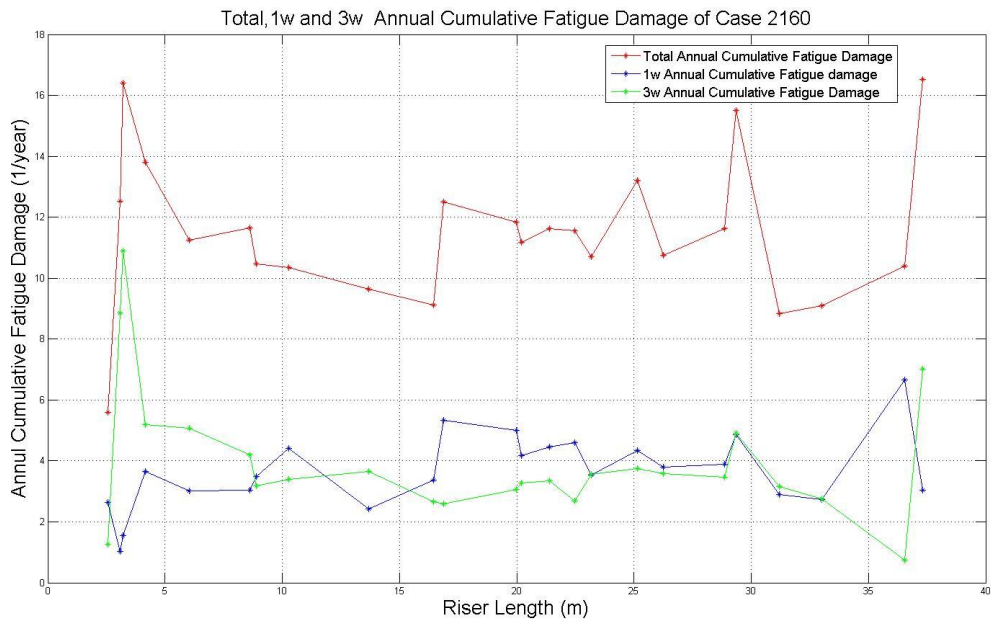
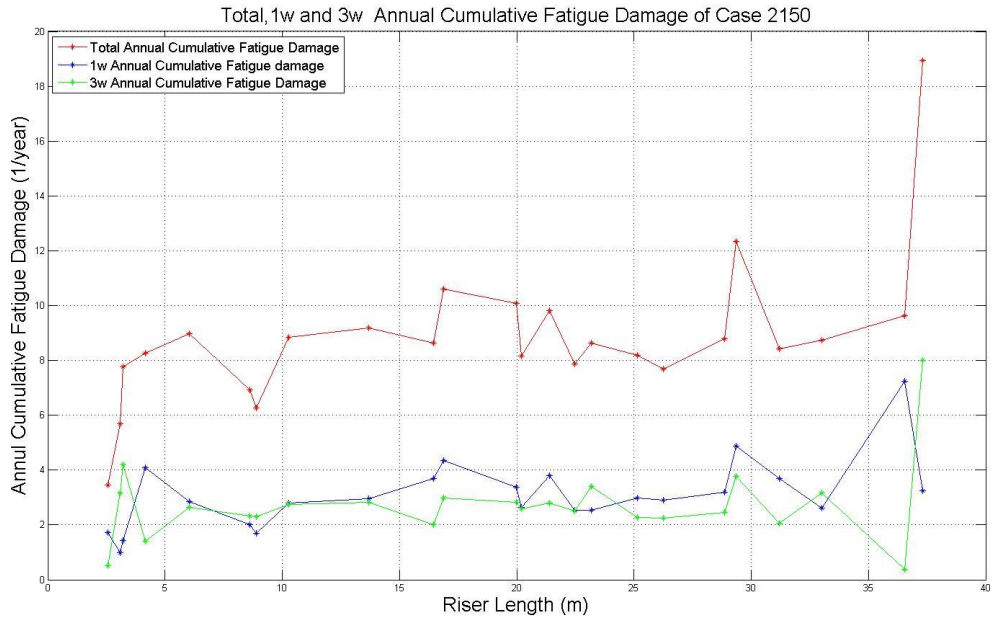


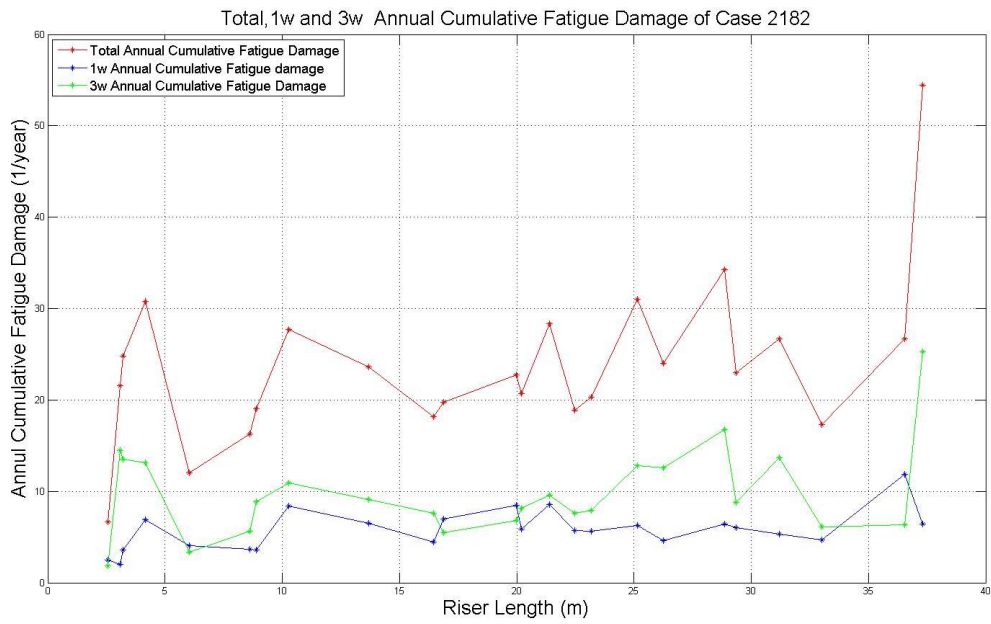
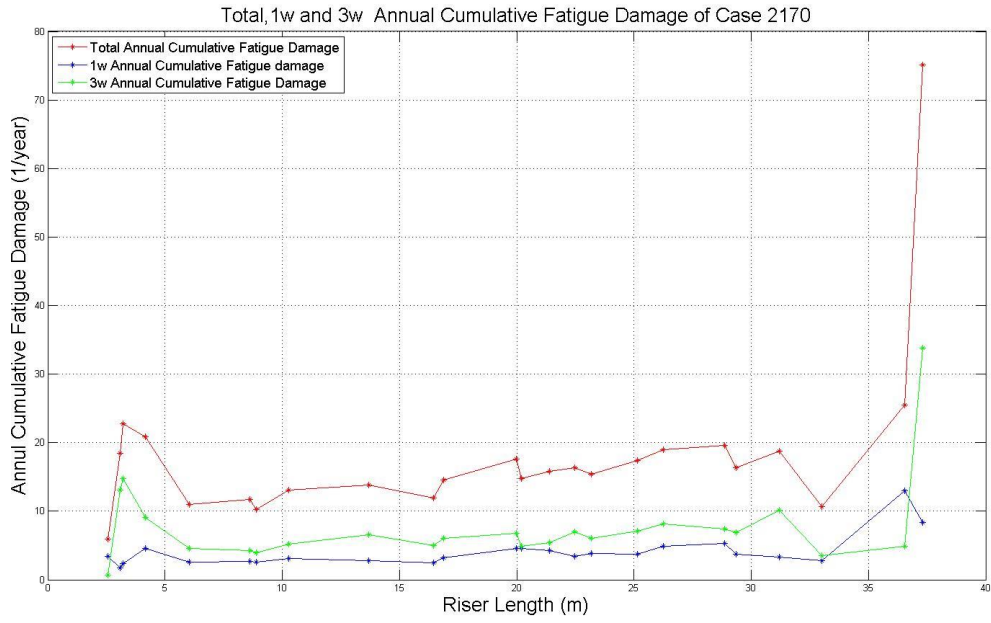


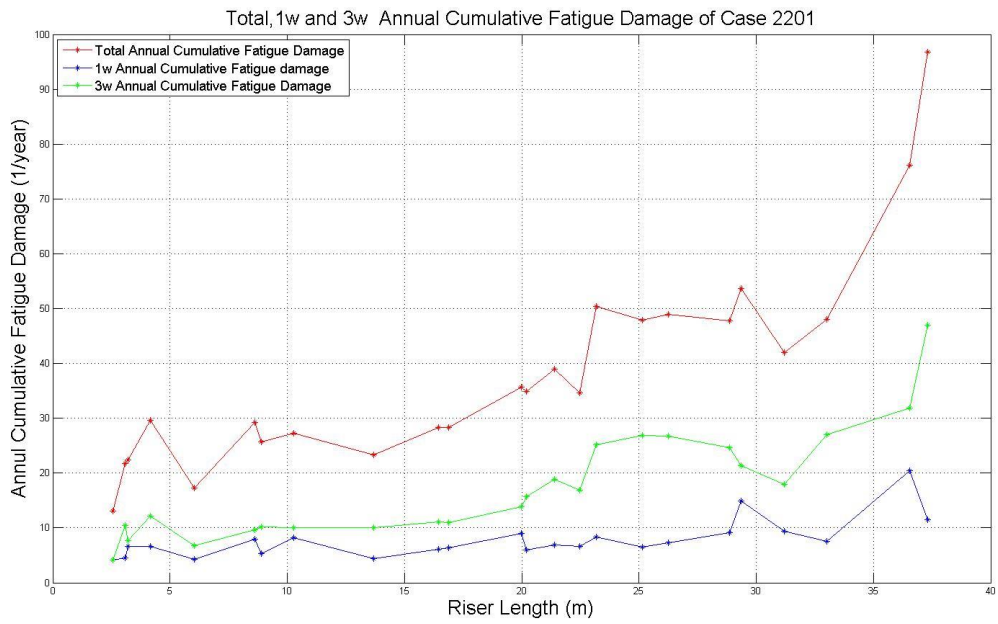
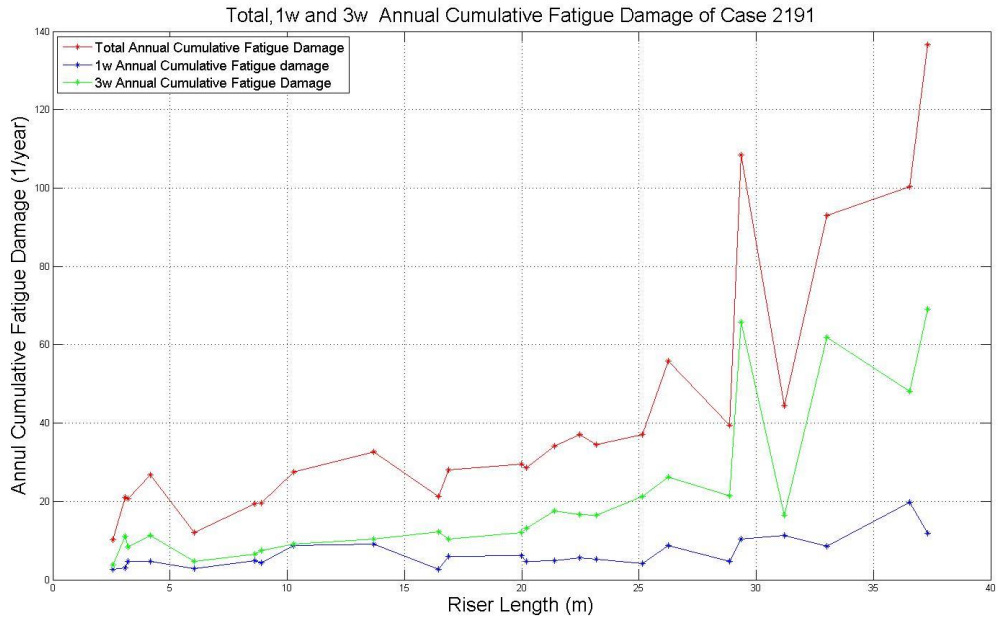


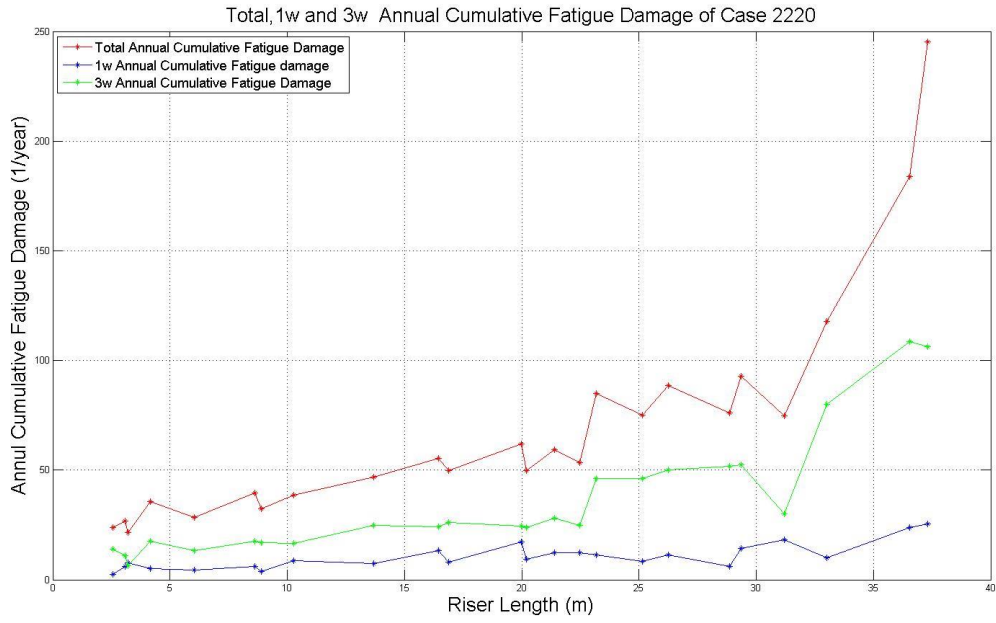
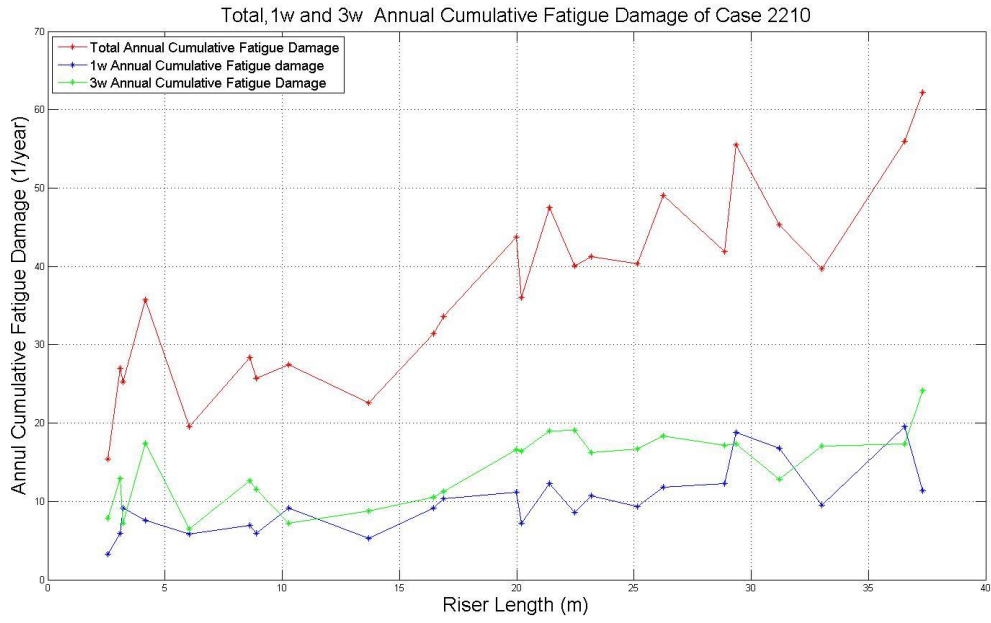








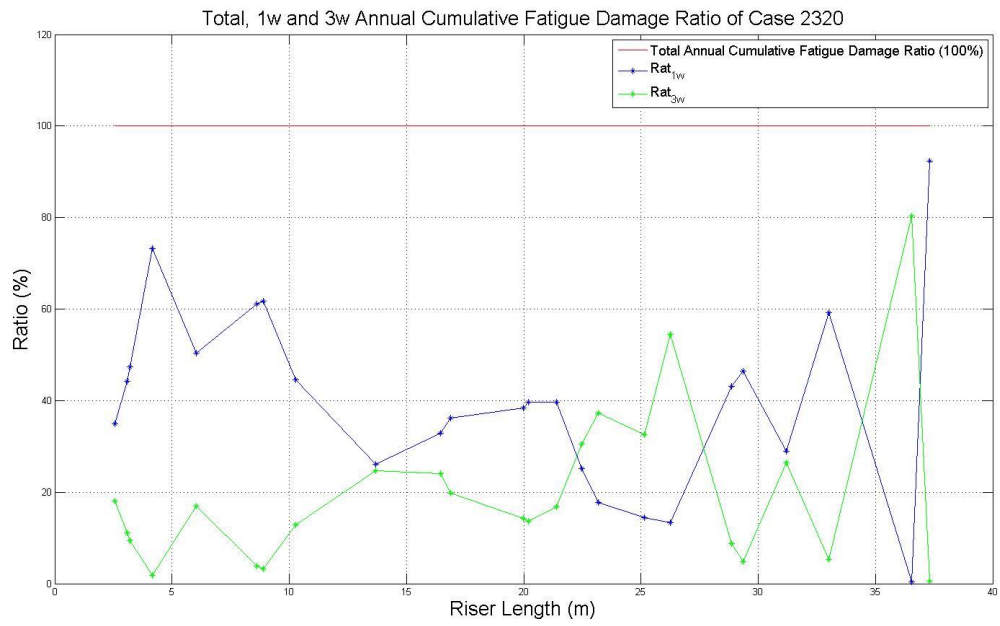
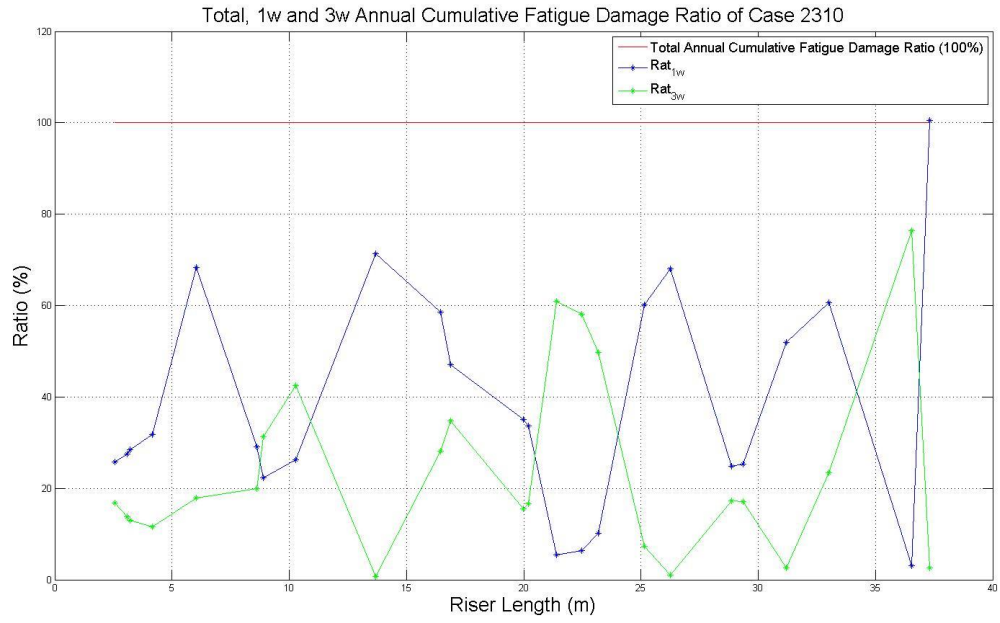


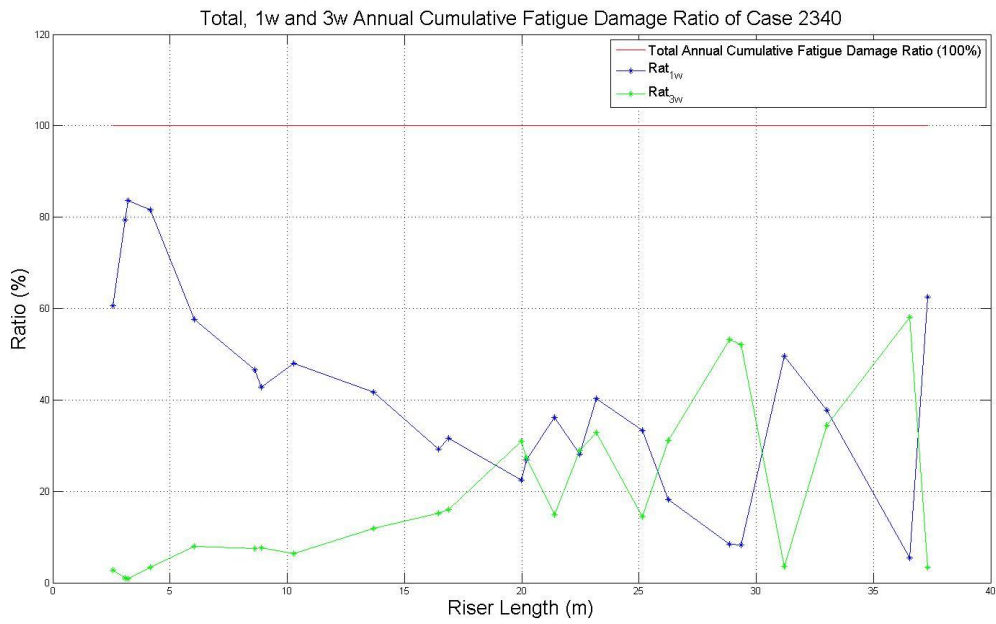
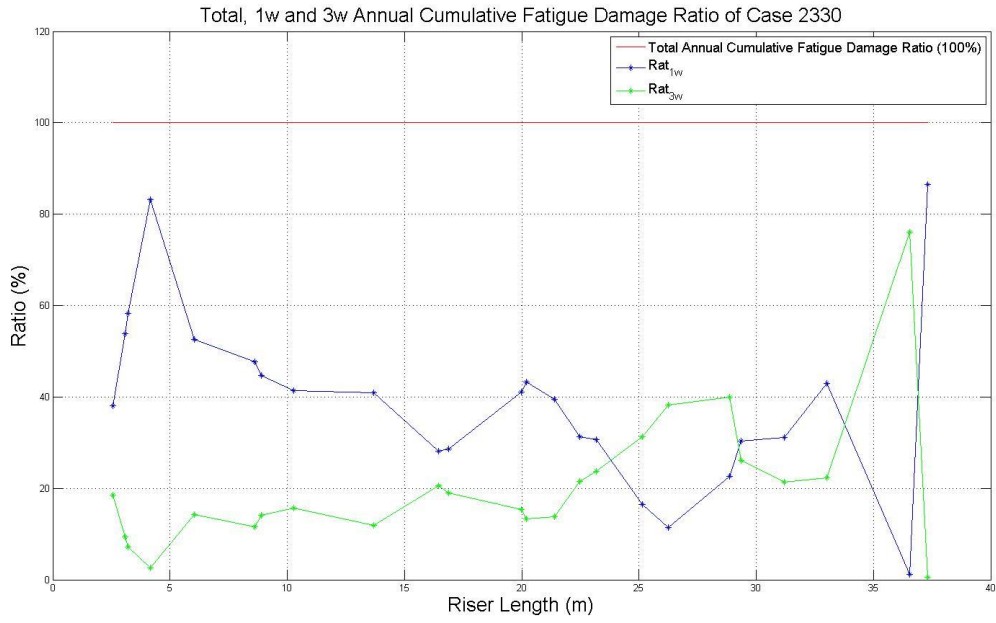


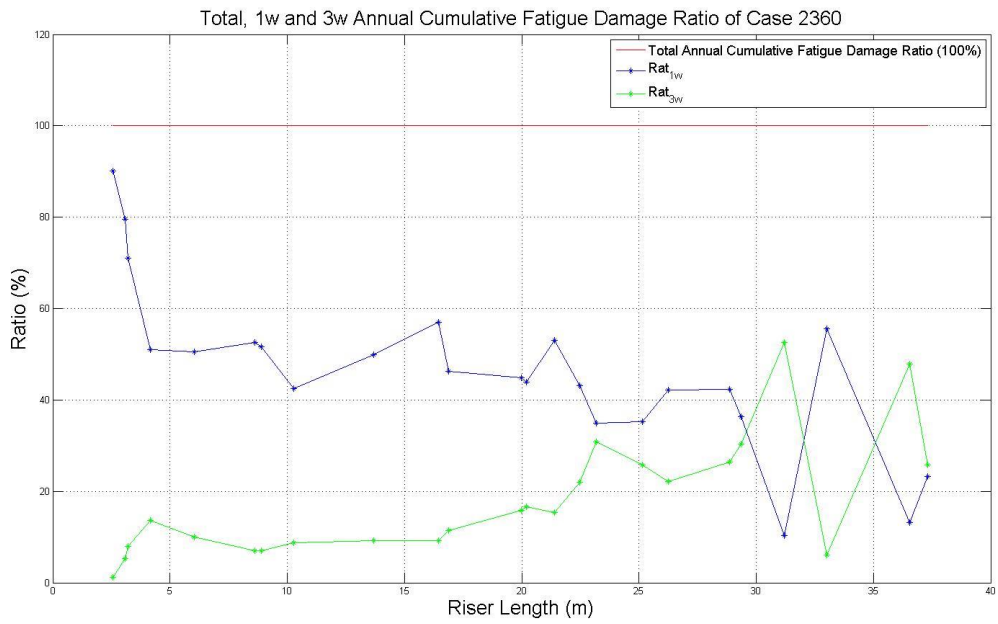
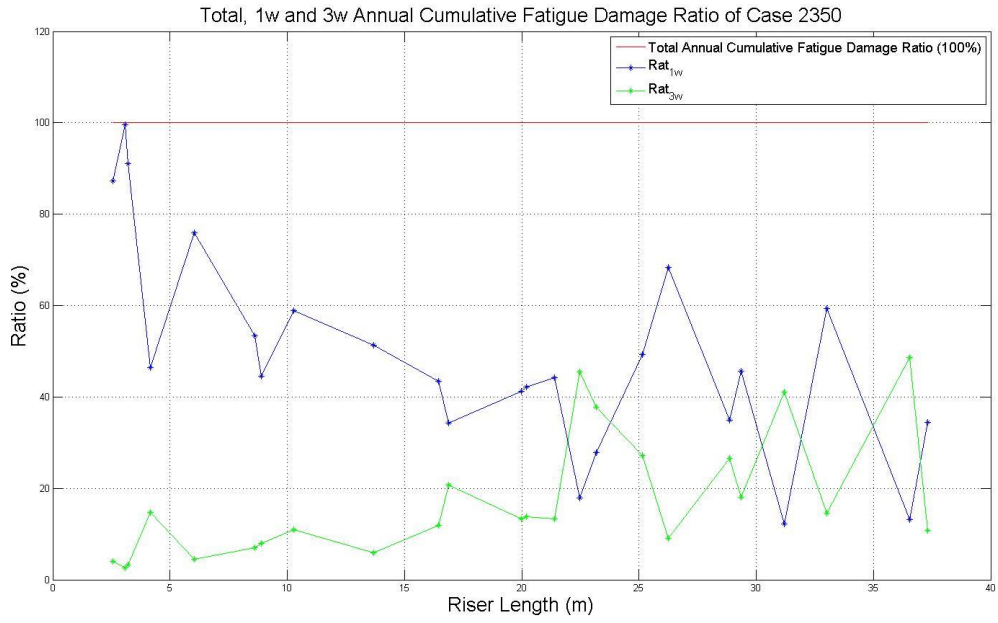
Appendix B

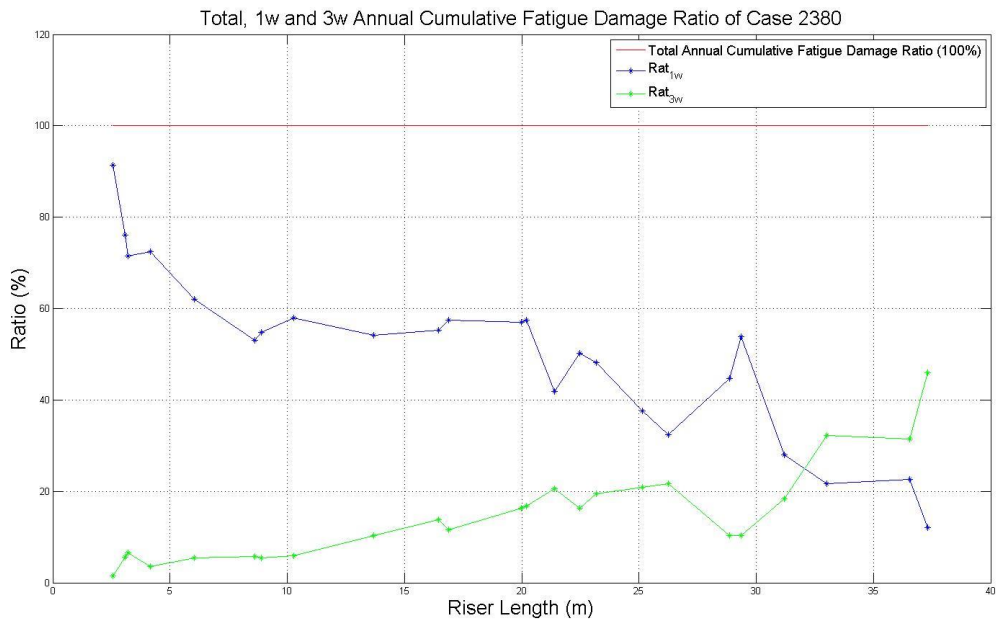
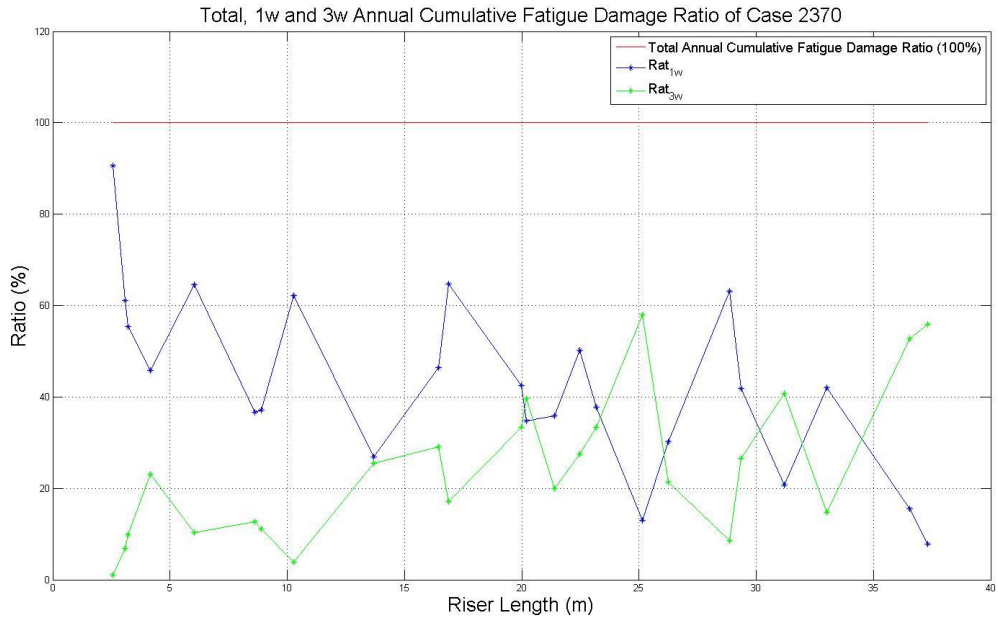
Annual Cumulative Fatigue Damage Results of NDP Tests

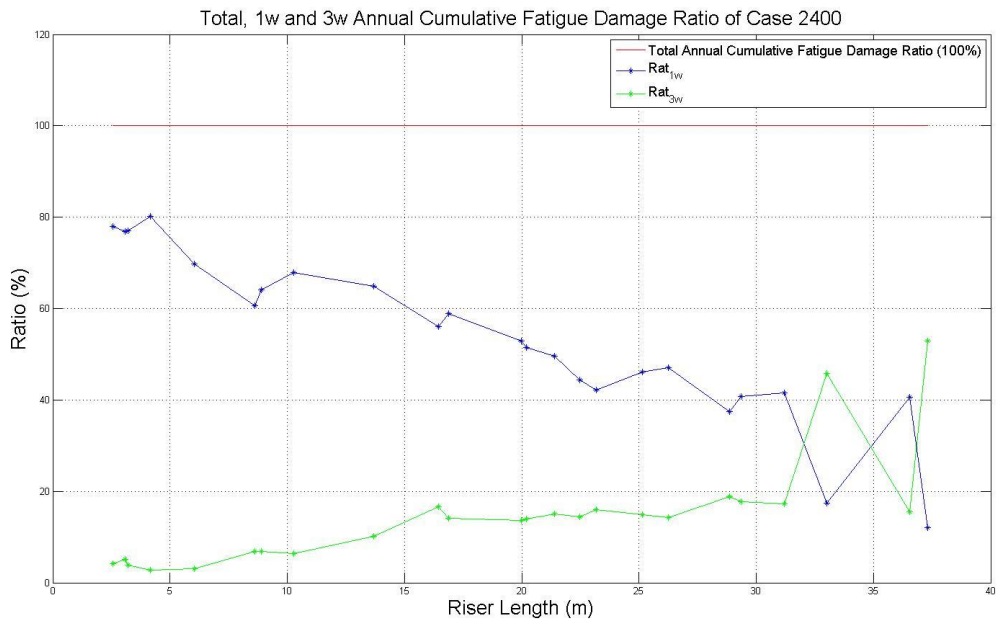
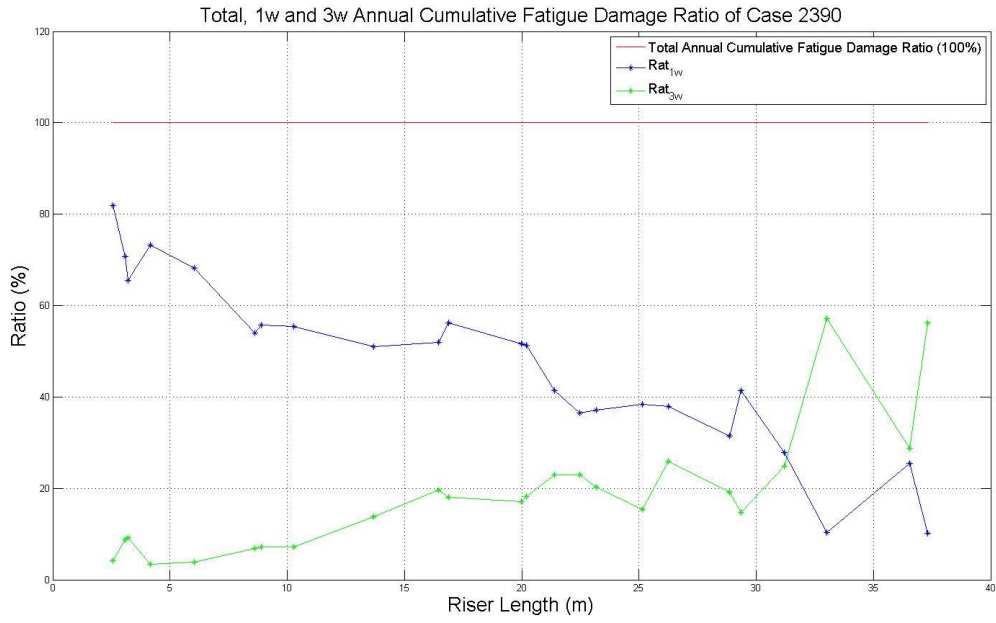
B.1 Comparison of Annual Cumulative Fatigue Damage Ratio for Total, $1 \times \omega$ and $3 \times \omega$ Frequency Component for Shear Flow Cases

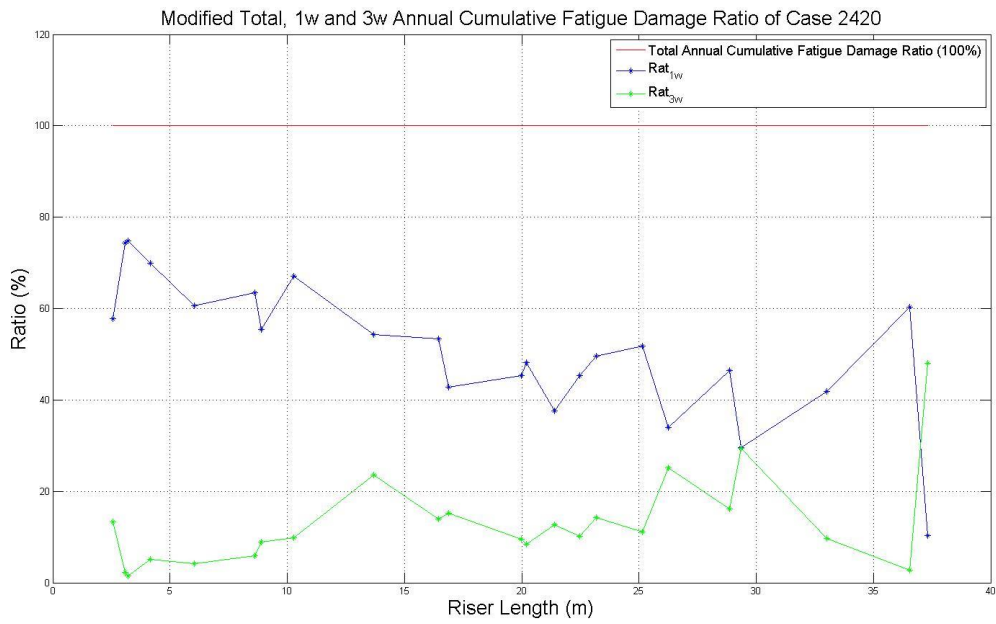
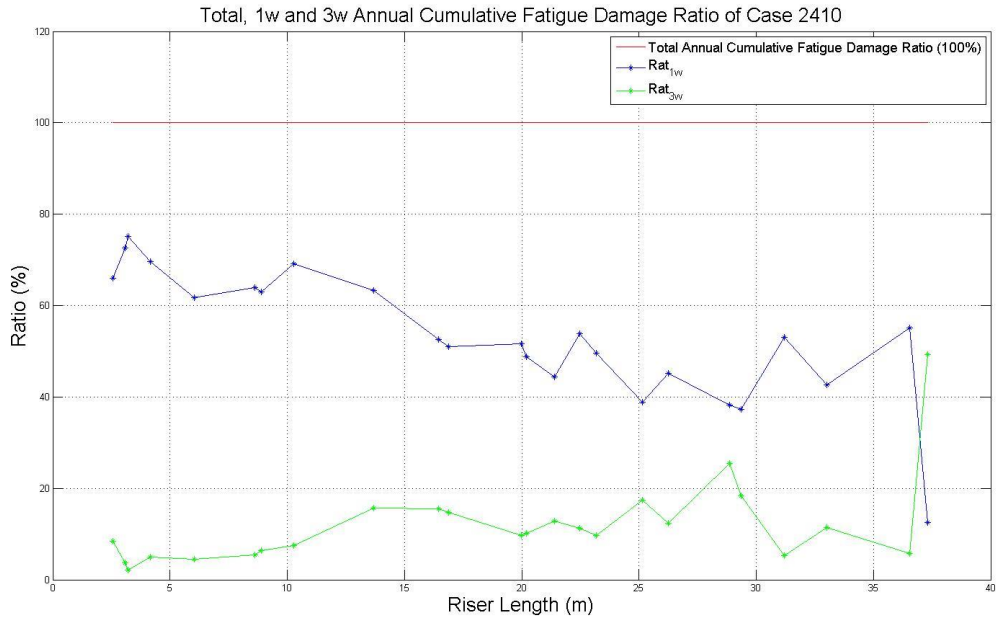


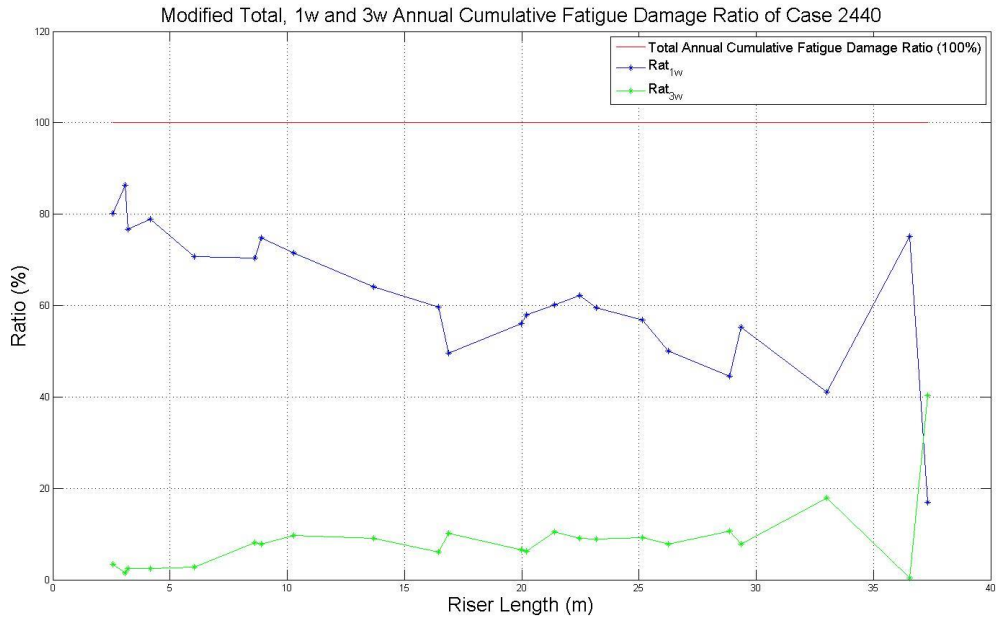
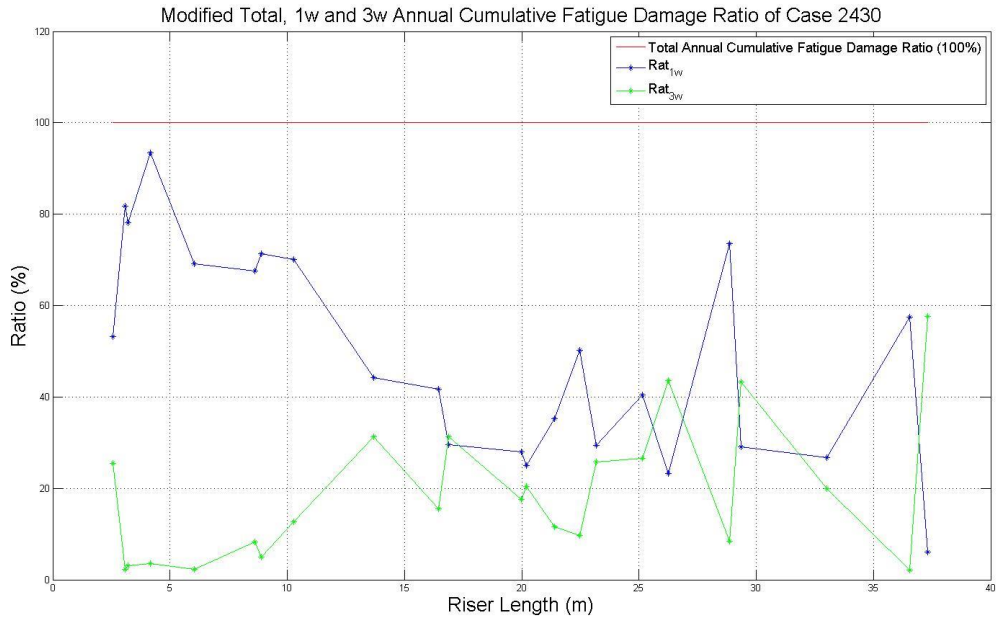


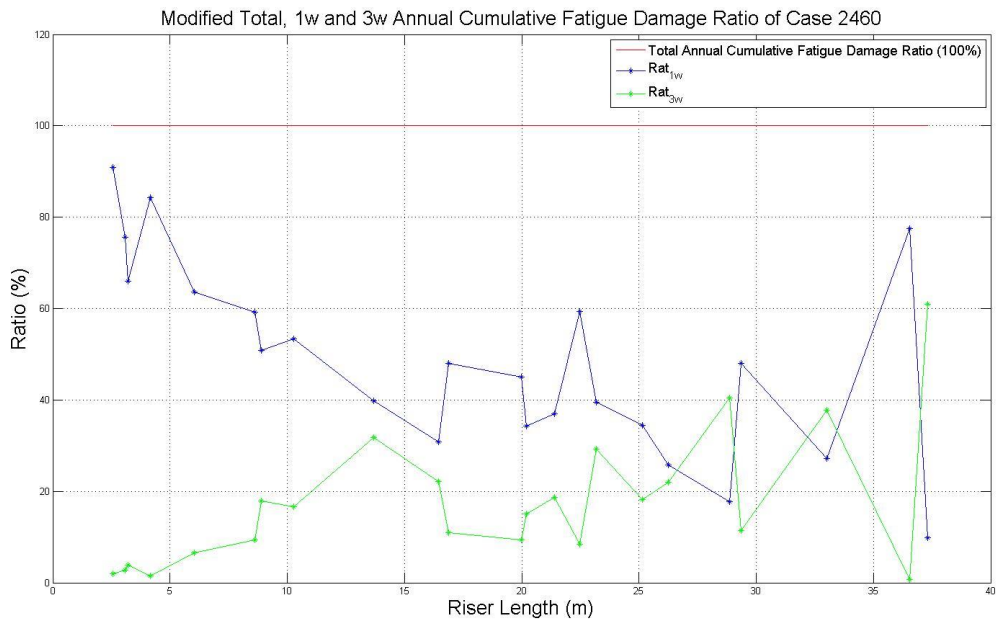
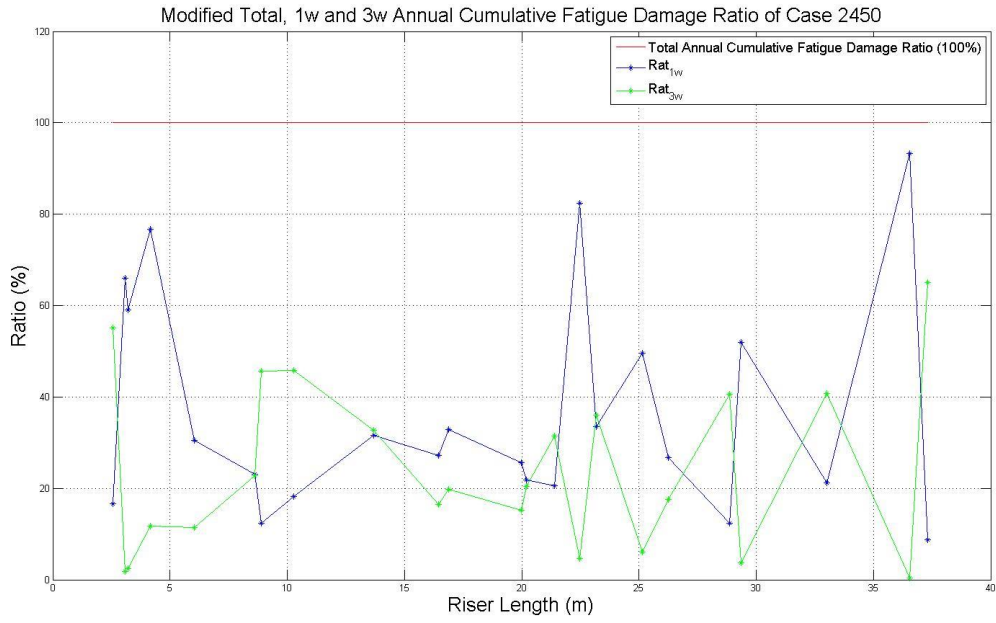


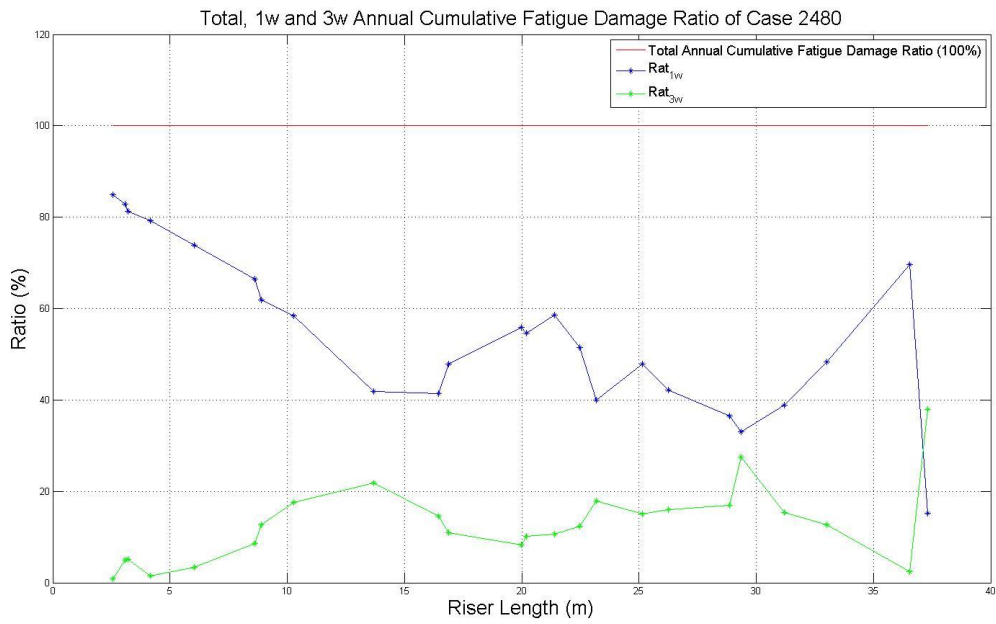
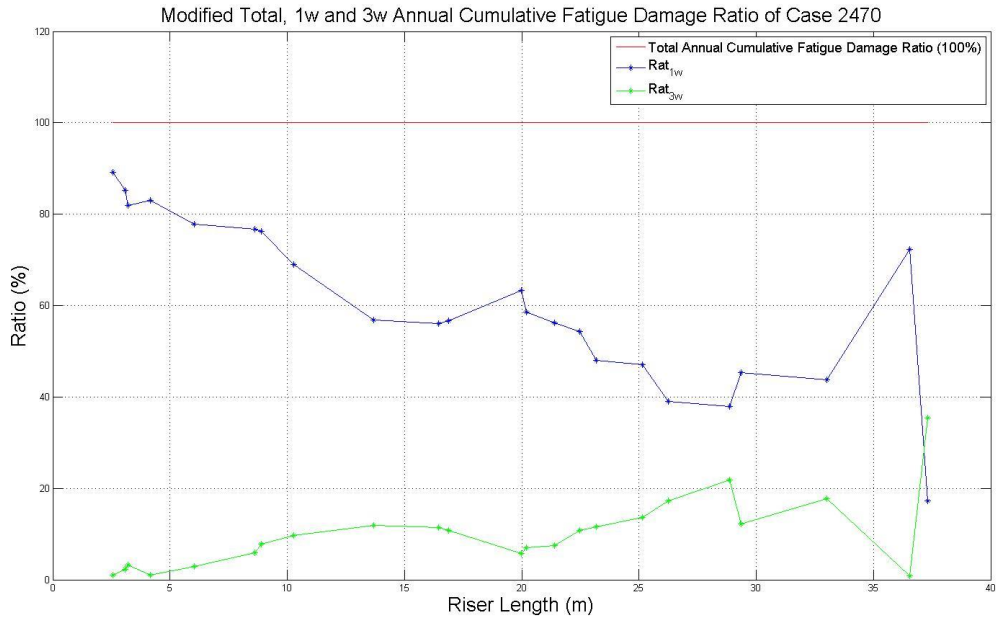


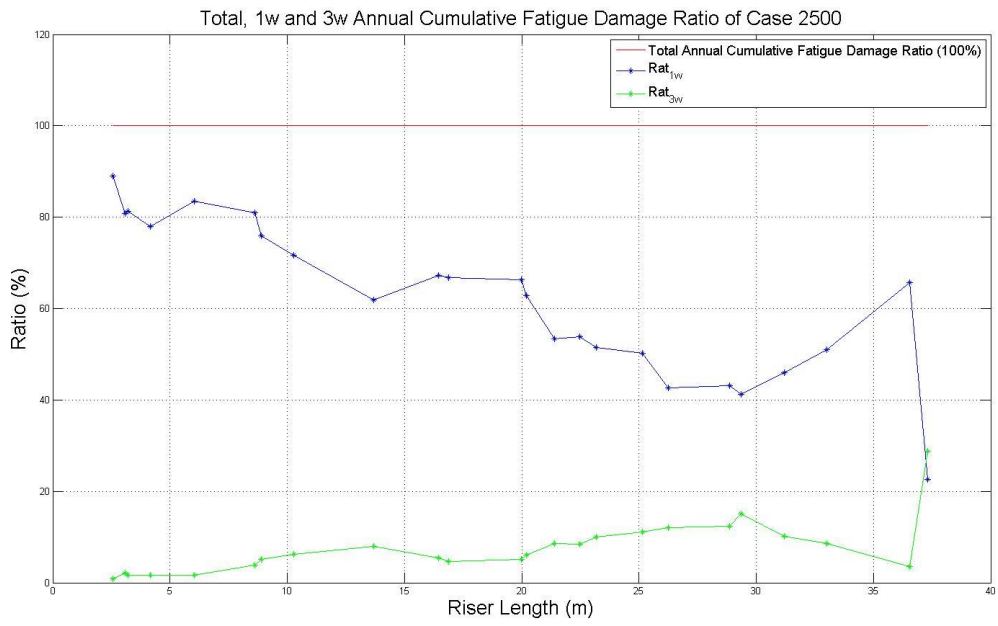
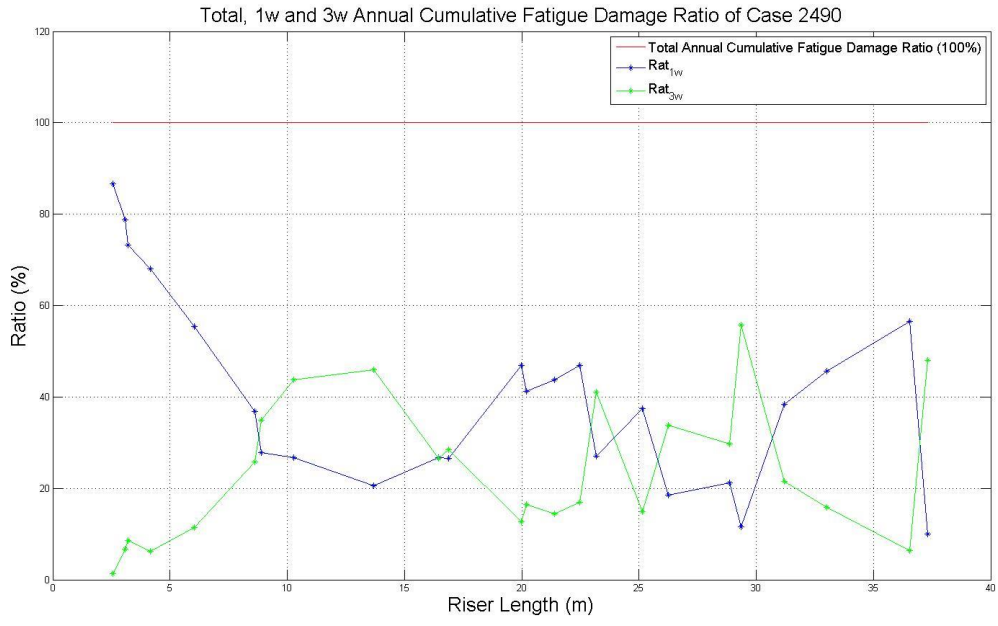


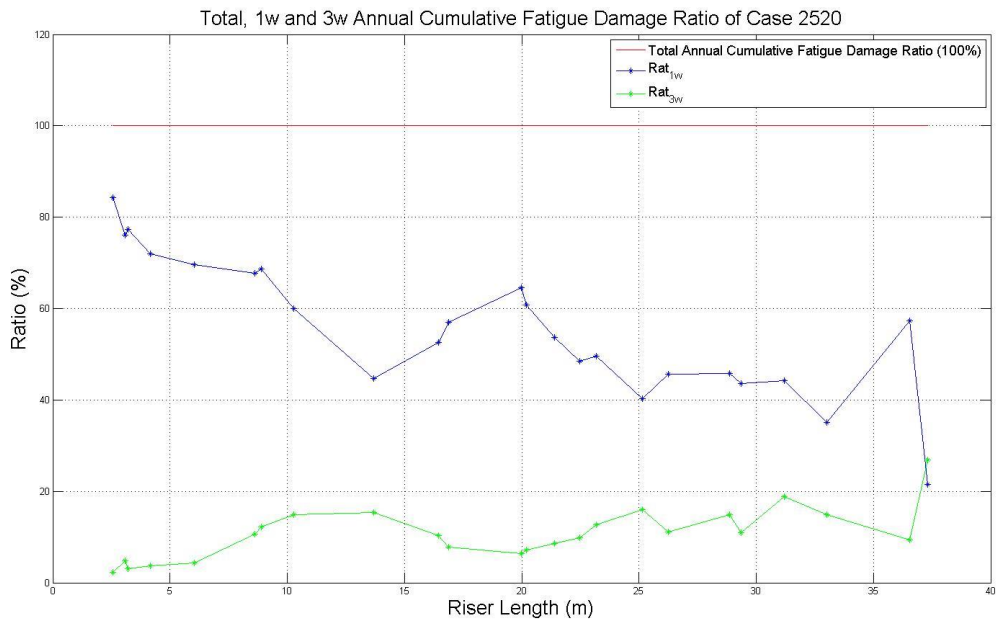
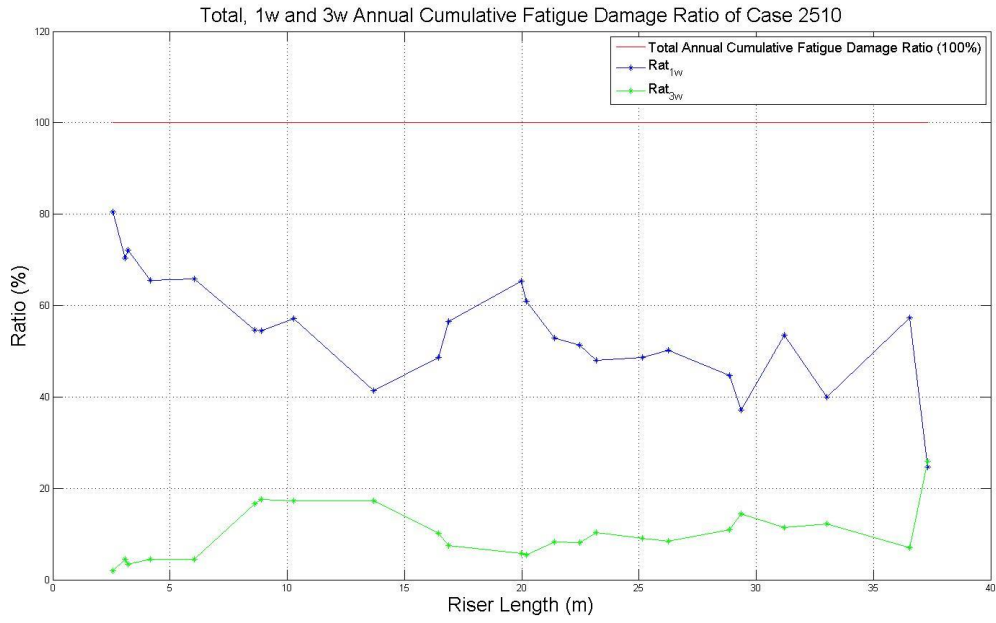




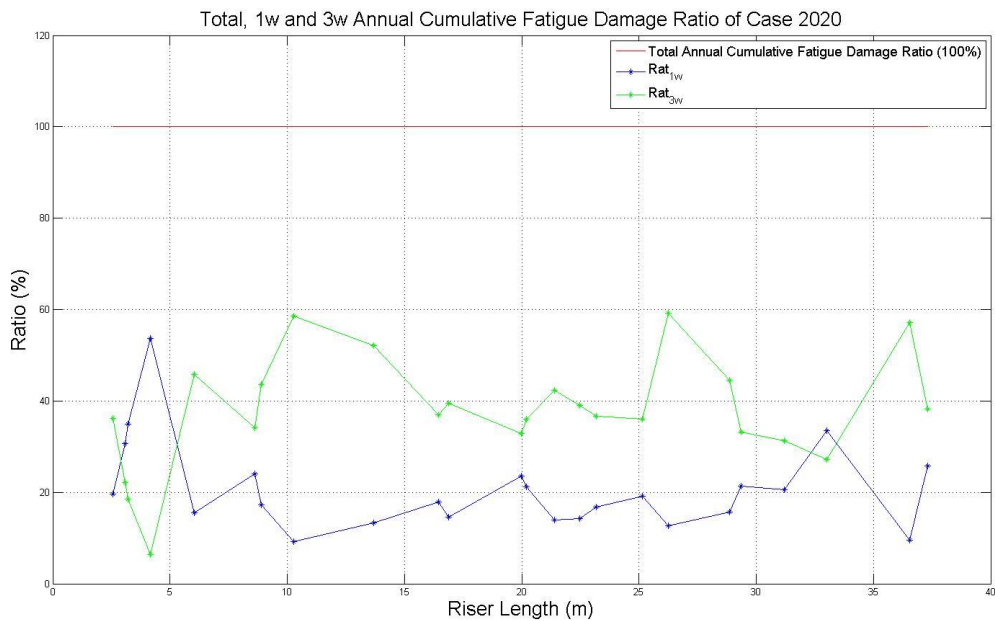
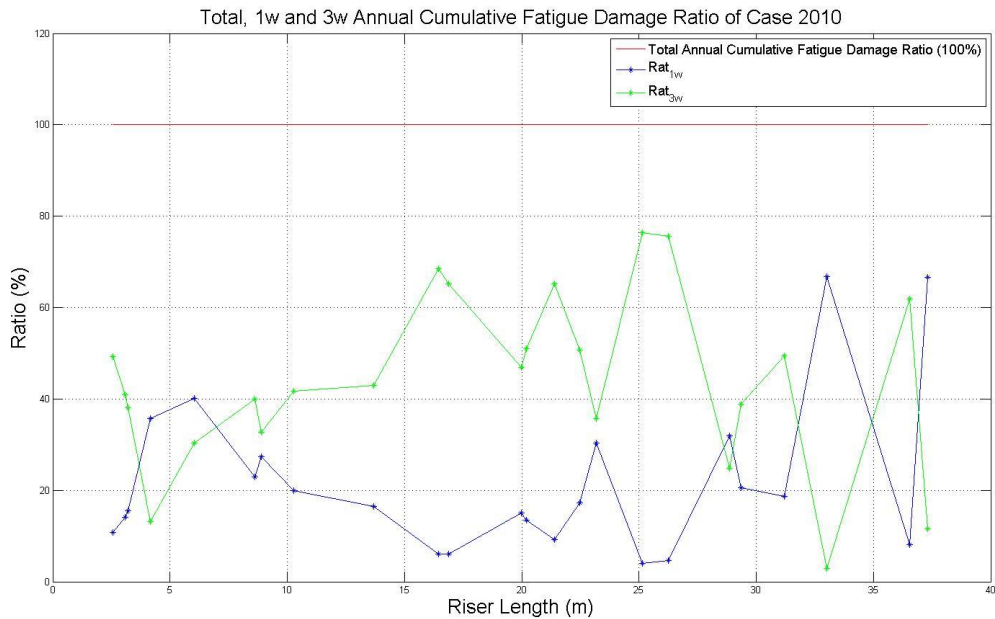


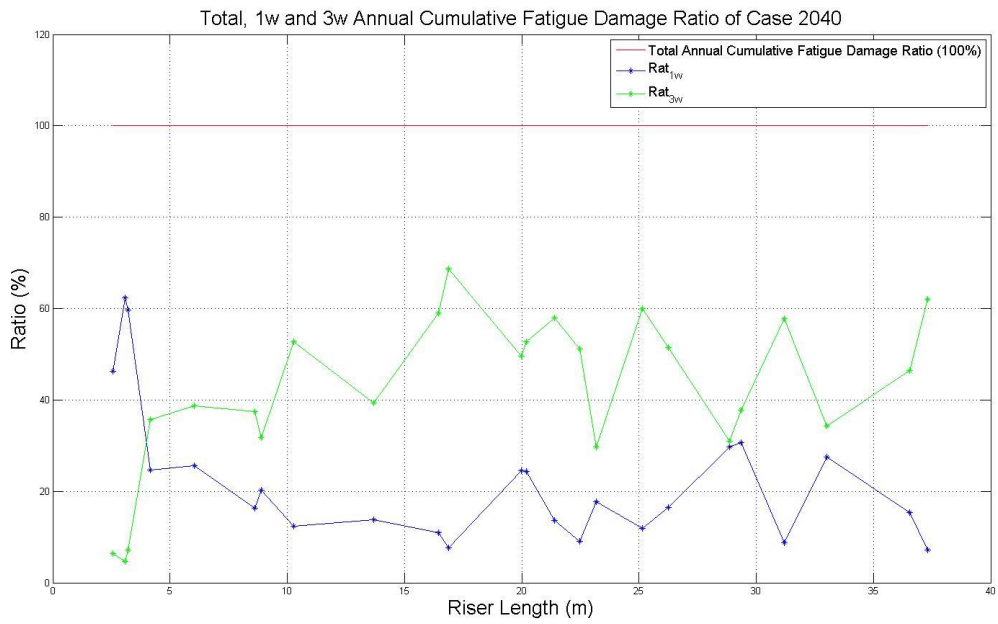
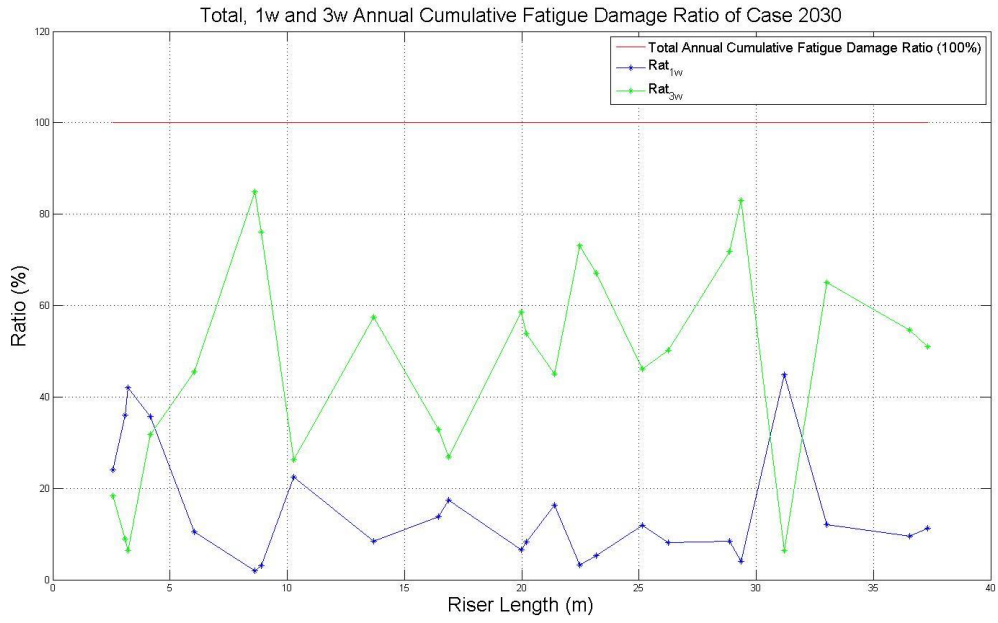


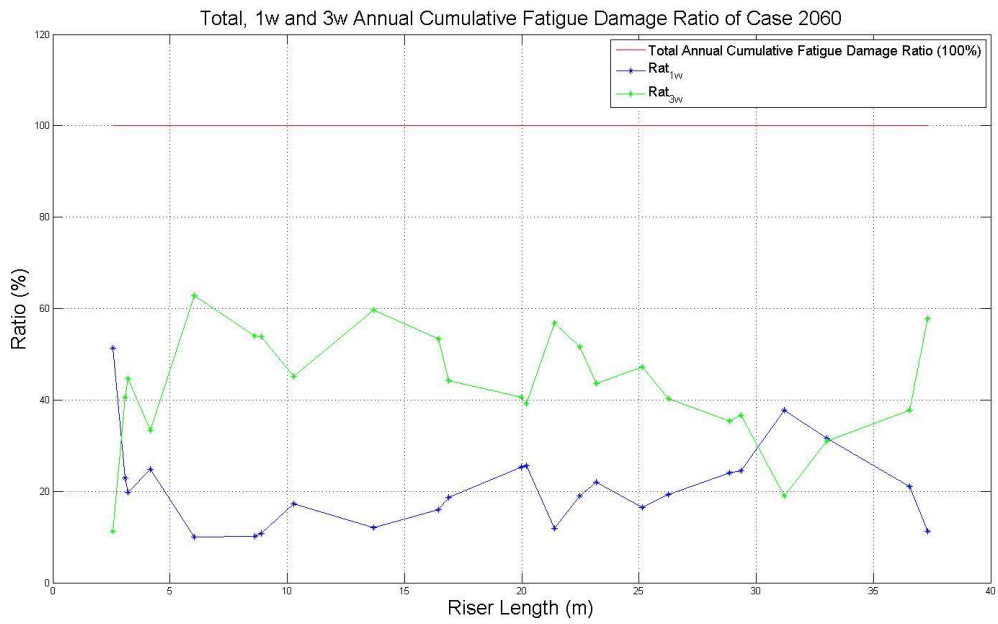
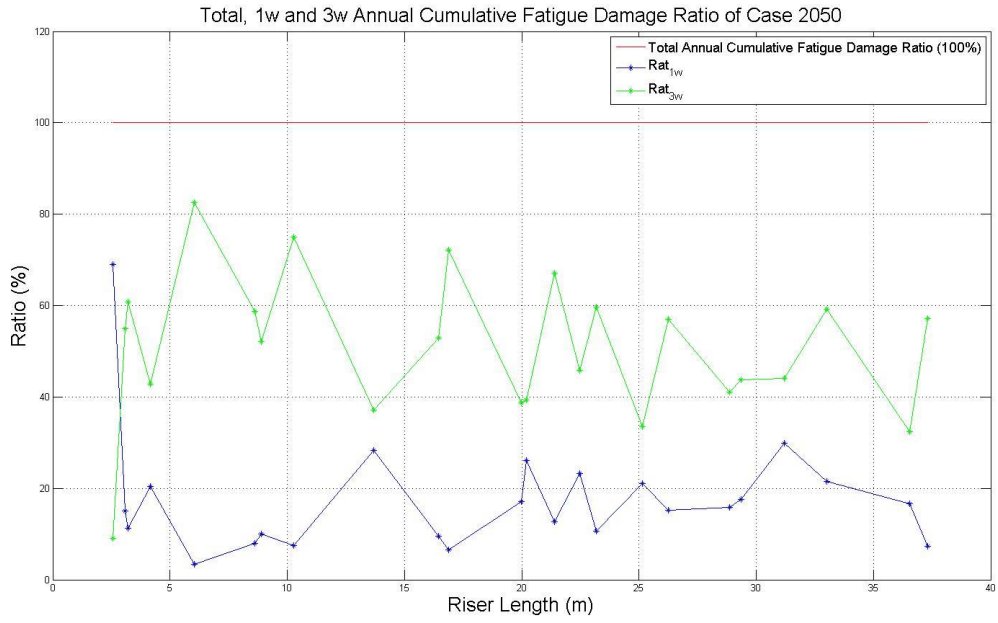


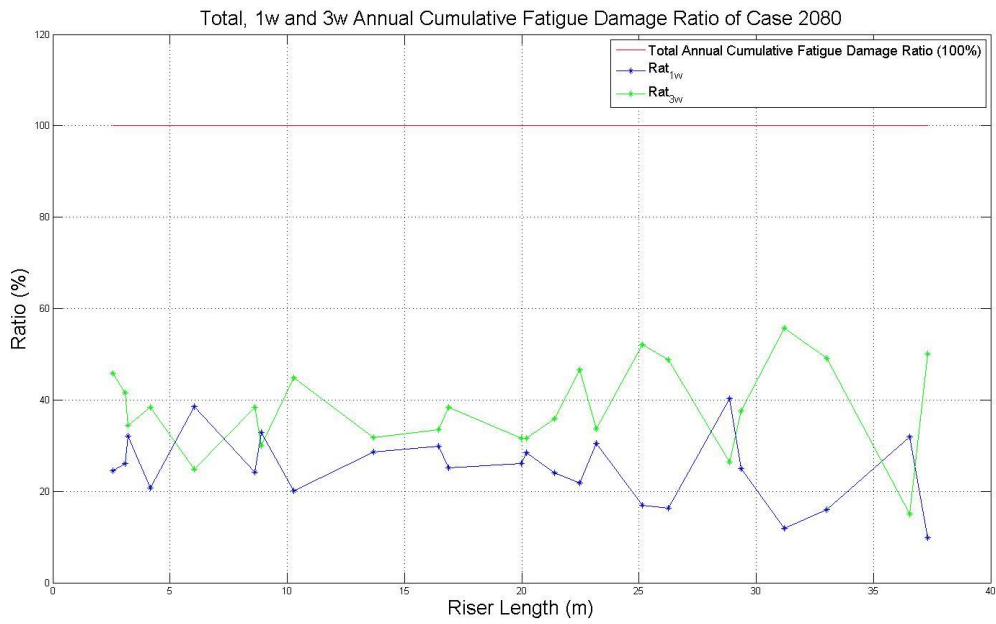
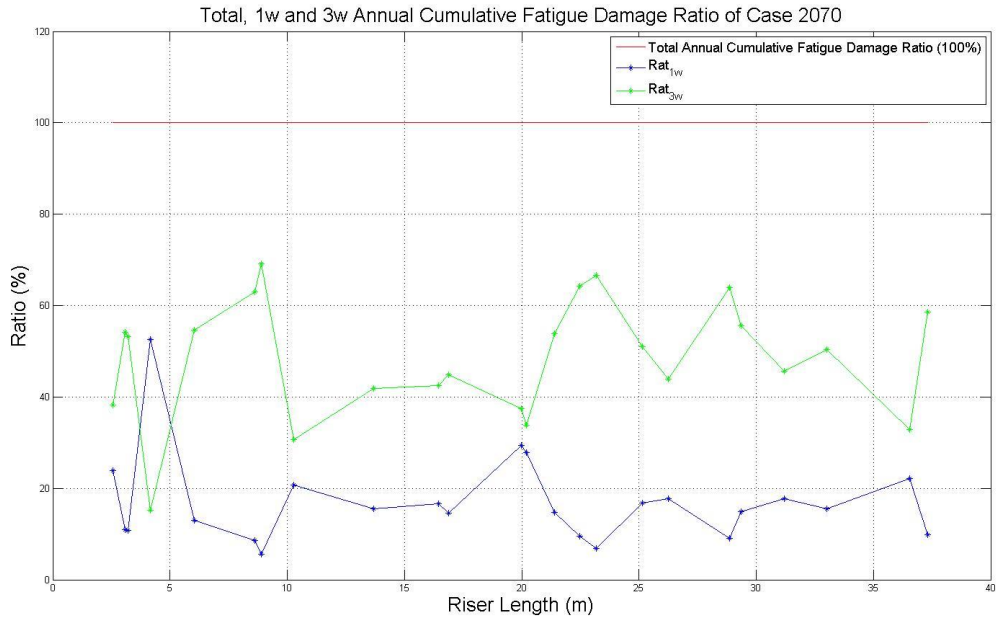


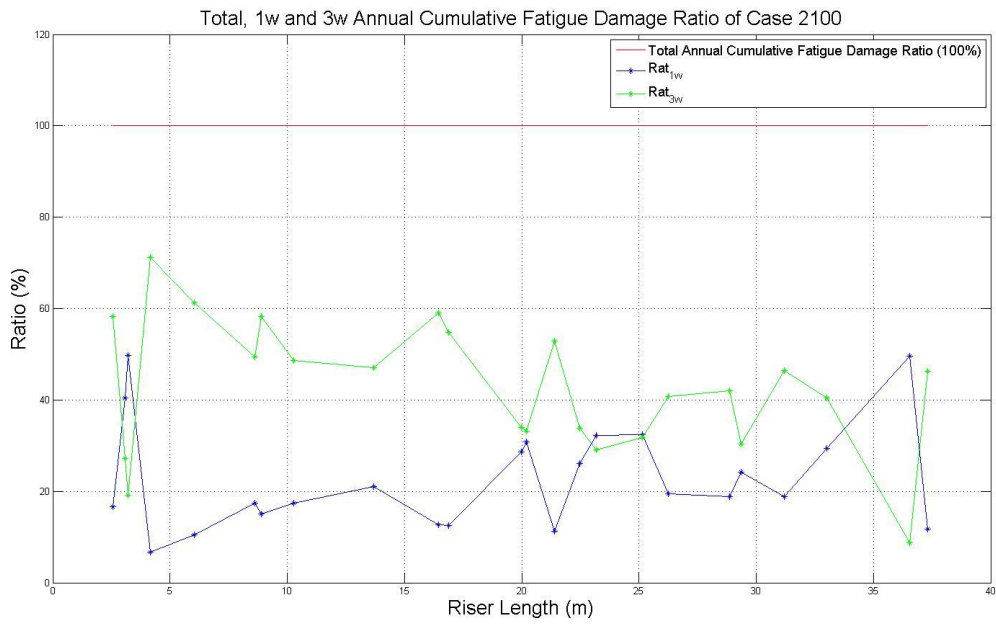
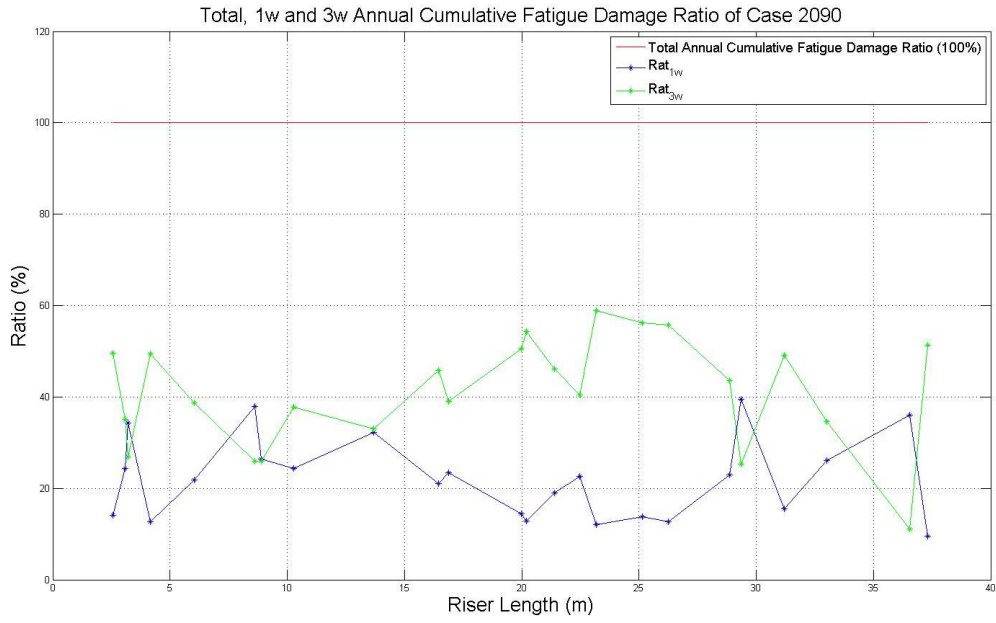
B.2 Comparison of Annual Cumulative Fatigue Damage Ratio for Total, $1 \times \omega$ and $3 \times \omega$ Frequency Component for Uniform Flow Cases

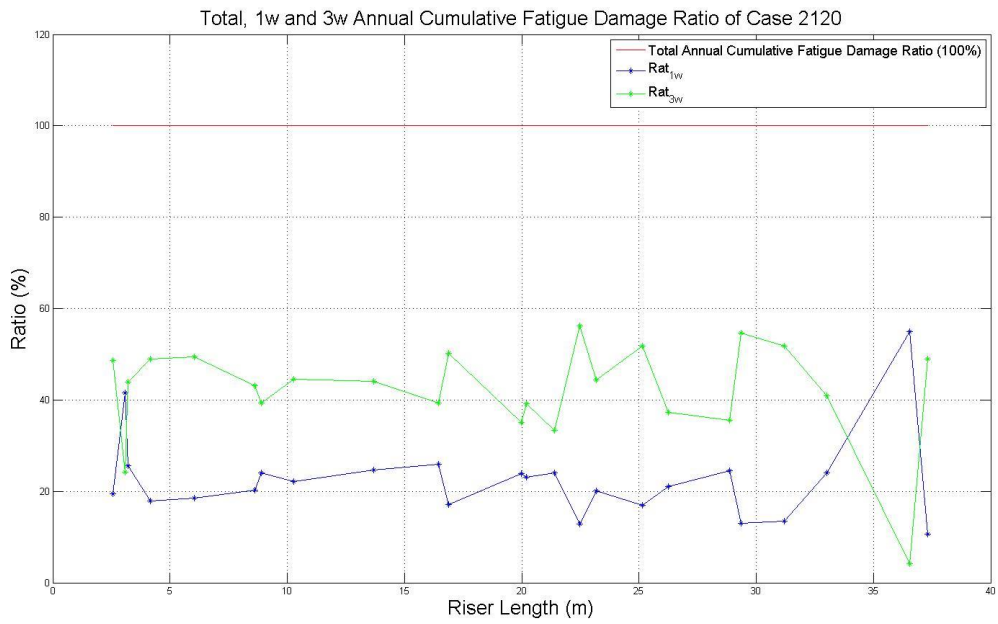
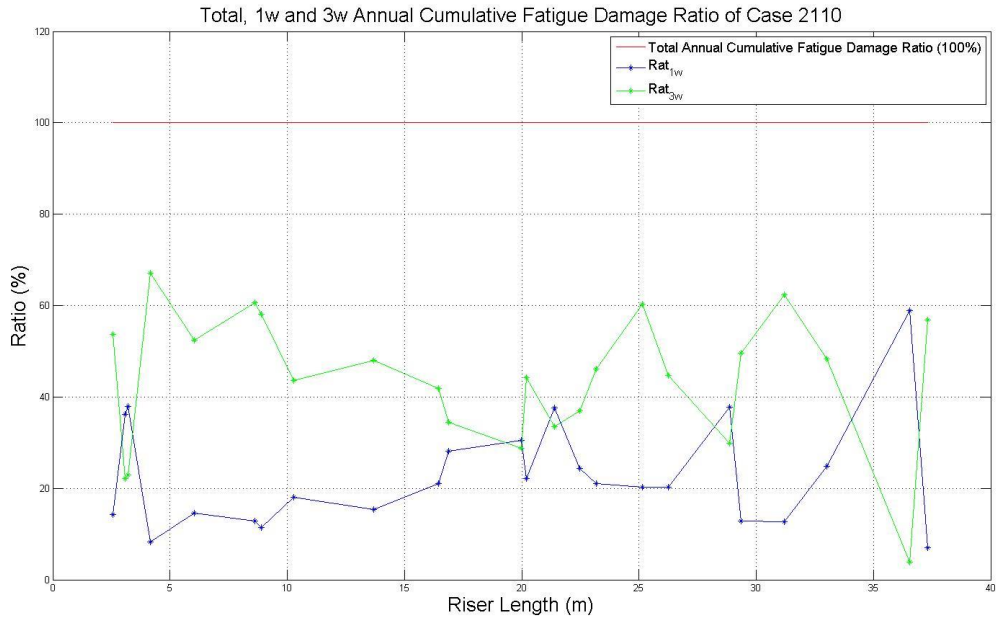


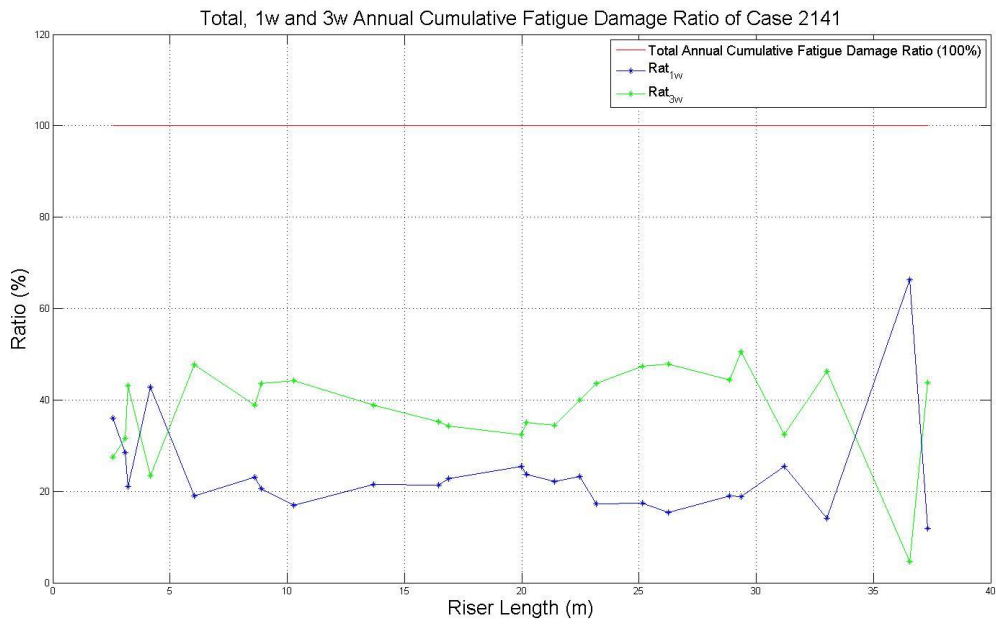
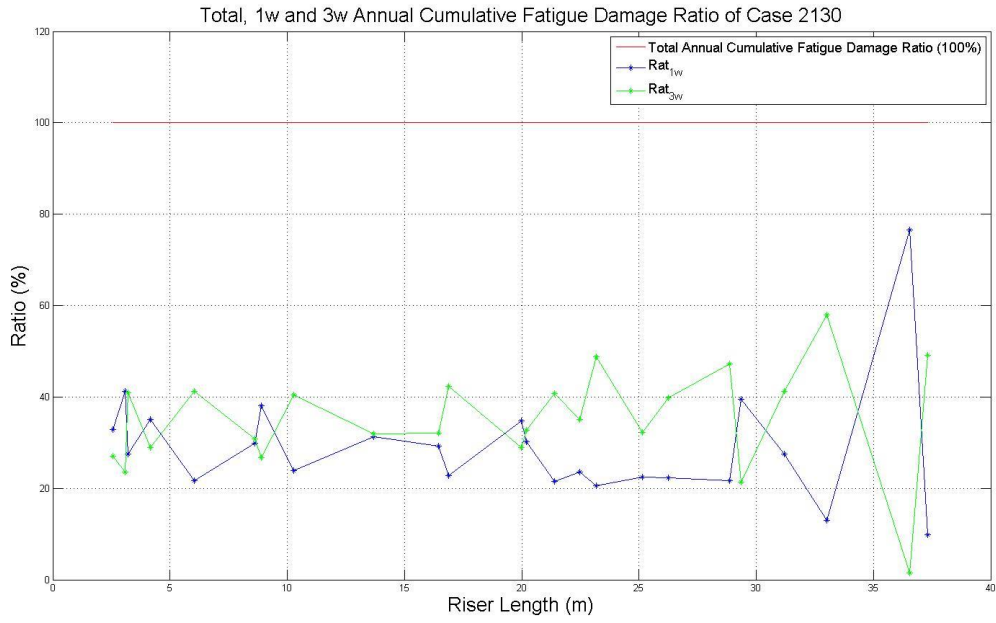


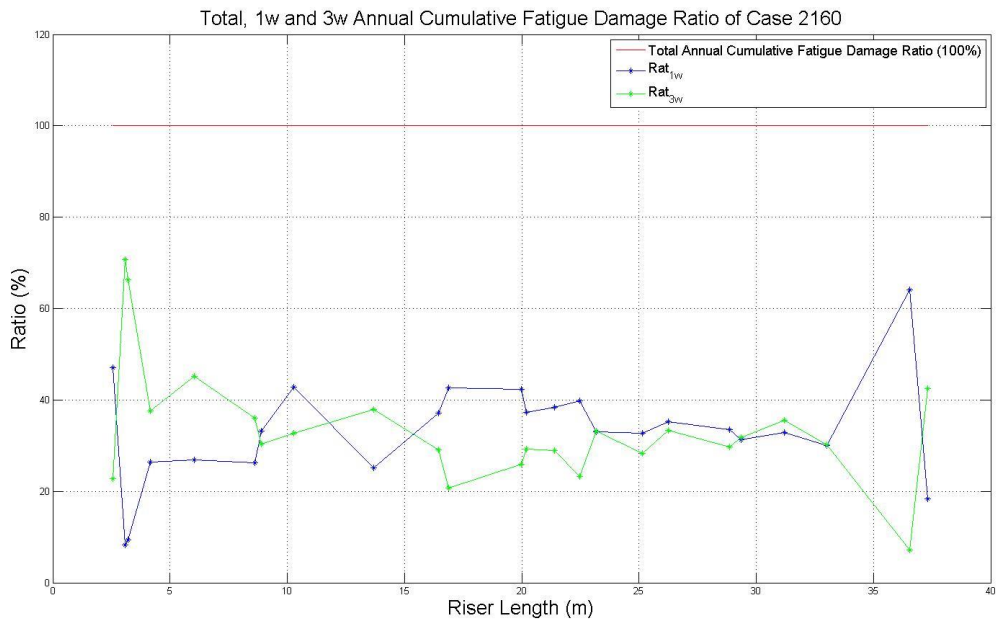
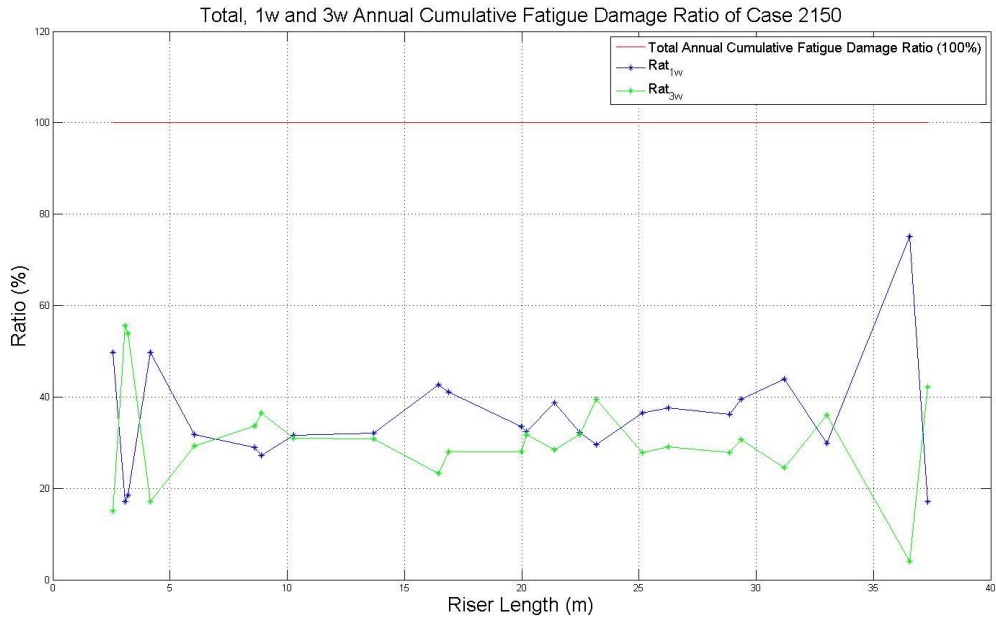


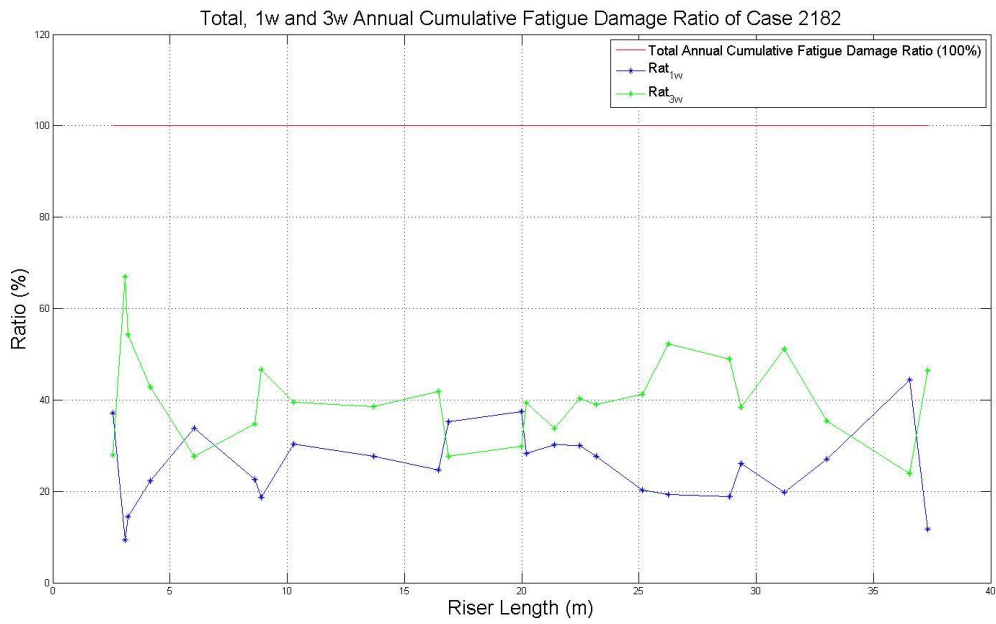
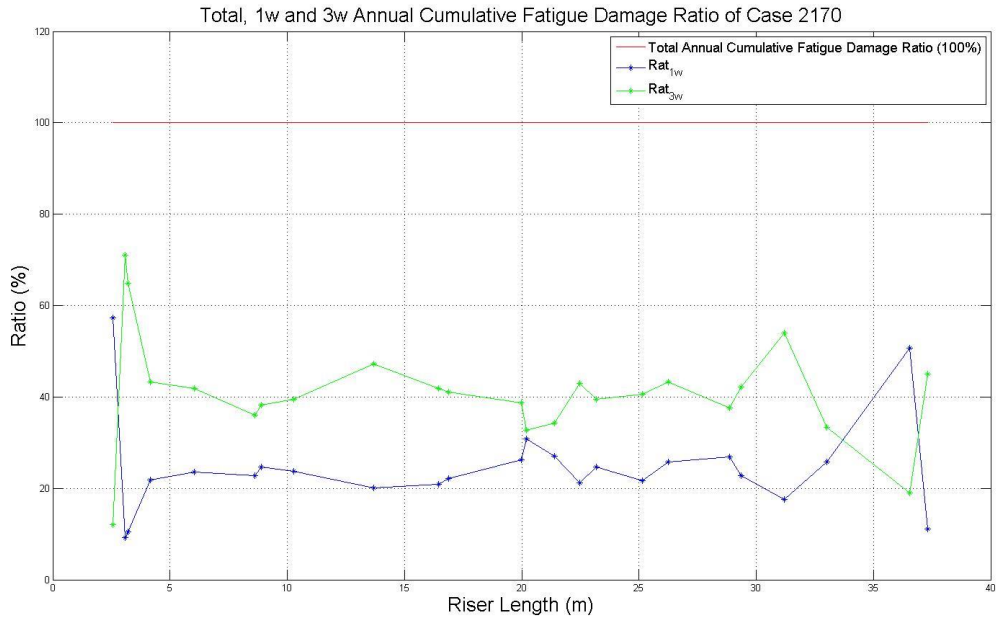


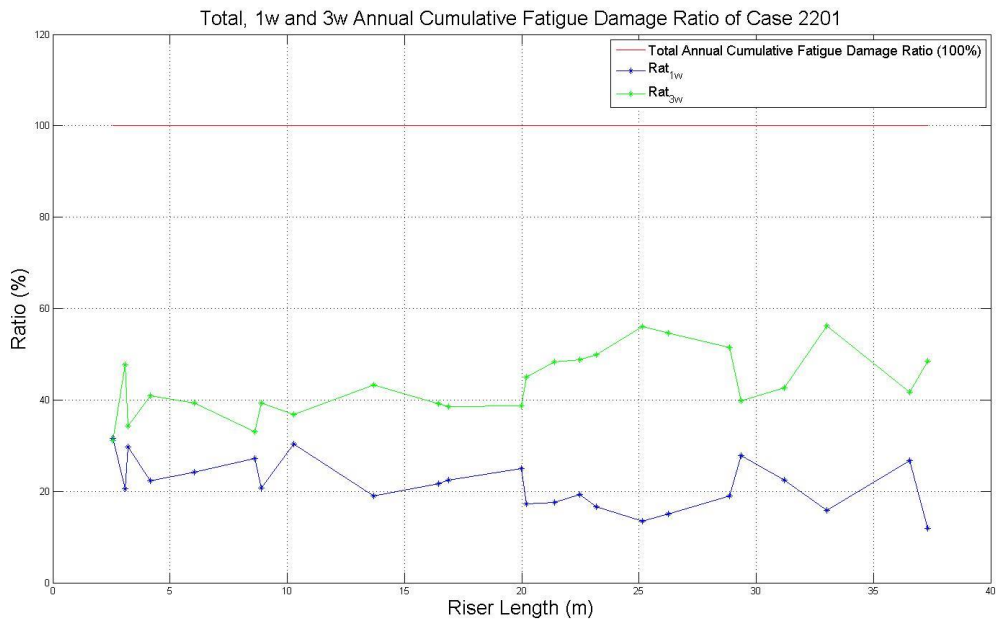
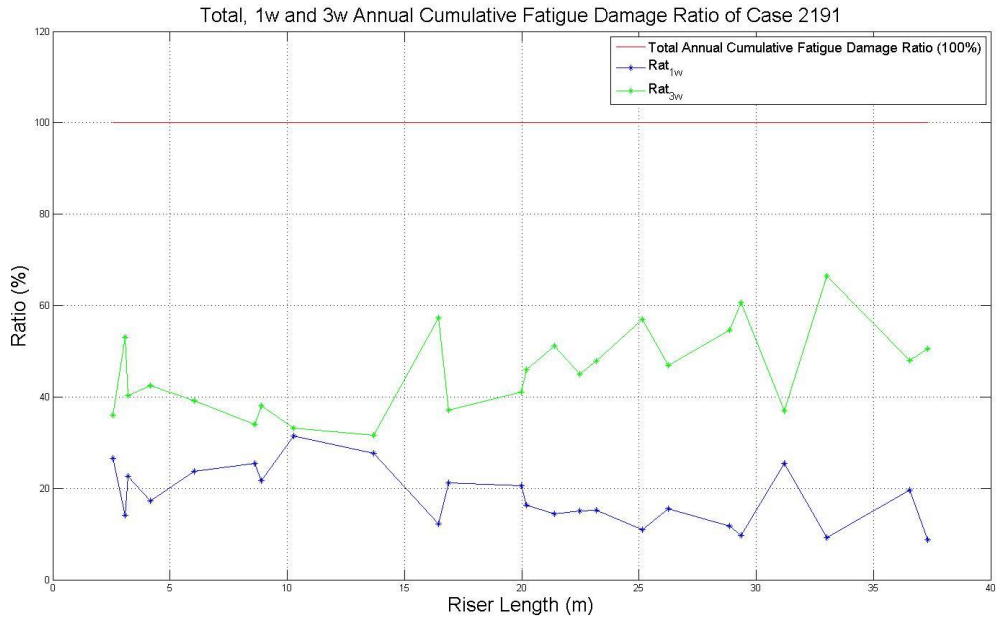


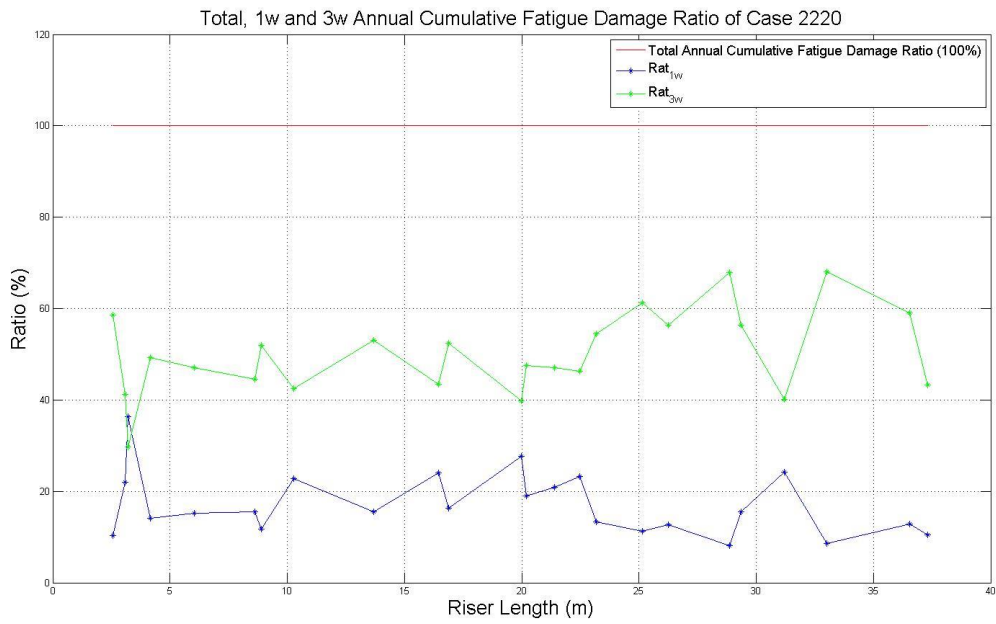
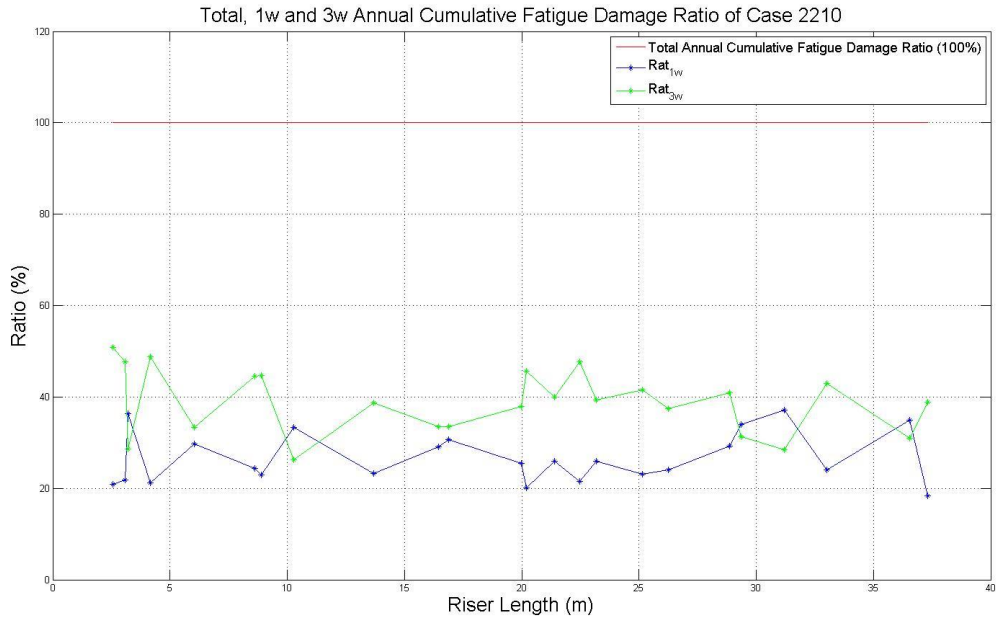












Bibliography

- [1] Larsen, C.M. and Lie, H., *On hydrodynamic coefficients for combined cross-flow and inline vortex induced vibrations*. The 27th International Conference on Offshore Mechanics and Arctic Engineering, OMAE2008-57569, June 2008, Estoril, Portugal.
- [2] Larsen C.M., Vikestad K., Yttervik R. and Passano E., *Empirical Model for analysis of vortex induced vibrations-theoretical background and case studies*. OMAE2001-1203, Rio de Janeiro, Brasil. 2001
- [3] Blevins, R.F., *Flow-Induced Vibration*. Krieger Publishing Company, Florida, Kriegerdrive, Florida, 2 edition, 1990.
- [4] Larsen, C.M., *Vortex induced vibrations (VIV)*. Lecture notes, 2007 Trondheim, Norway
- [5] Sumer, B.M. and Fredse, J., *Hydrodynamics around cylindrical structures*. World Scientific Publishing Co. Tte. Ltd, 2006, USA
- [6] Pantazopoulos, M. S., *Vortex-induced Vibration parameters: Critical review*. In Proceedings of the 17th International Conference on Offshore Mechanics and Arctic Engineering (OMAE), volume 1, pages 199-255, 1994.
- [7] Gopalkrishnan, R., *Vortex-Induced Forces on Oscillating Bluff Cylinders*. PhD thesis, Department of Ocean Engineering, Massachusetts Institute of Technology, Cambridge, MA, USA,1993.
- [8] Huse, E., Kleiven, G. and Nielsen, F.G., *Large scale model testing of deep sea risers*. Proceedings of the Offshore Technology Conference 1998, OTC 8701, Houston, Texas, USA.
- [9] Tognarelli, M., Fontaine, E., Beynet, P., Santosa,M. and Marcollo, H., *Reliability-based factors, of safety for VIV fatigue using field measurements*. Proceedings of Offshore Mechanics and Arctic Engineering Conference 2010, OMAE2010-21001, June 2010, Shanghai, China.
- [10] Jauvtis, N. and Williamson, C. H. K., *The effect of two degrees of freedom on vortex-induced vibration at low mass and damping*. Journal of Fluid Mechanics (2004), vol. 509,23-62.

-
- [11] Triantafyllou, M. S., Techet, A. H., Hover, F. S., Yue, D. K. P., *VIV of slender structures in shear flow. Presented at IUTAM symposium on Flow-Structure Interactions*, June 2003, Rutgers State University, USA.
- [12] Swithenbank, S. B., Vandiver, J.K., Larsen, C. M. and Lie, H., *Reynolds number dependence of flexible cylinder VIV response data*. The 27th International Conference on Offshore Mechanics and Arctic Engineering, OMAE 2008-57045, June 2008, Estoril, Portugal.
- [13] Maincon, P., A Wiener-Laguerre, *model of VIV forces given recent cylinder velocities*. Journal of Mathematical Problems in Engineering (In press)
- [14] Facchinetti, M. L. Langre, E. D. and Biolley, F., *Vortex Induced traveling waves along a cable*. European Journal of Mechanics B/Fluids (23), 199-208, 2004.
- [15] Guyan, R. J., *Reduction of Stiffness and Mass Matrices*. AIAA Journal, vol 3, no. 2, 1965.
- [16] Mukundan, H., Hover, F. S. and Triantafyllou, M. S., *A systematic approach to riser VIV response reconstruction*. Journal of Fluids, and Structures. (2010)
- [17] Maincon, P., Barnardo, C., *Inverse finite element methods for structural response and load estimation from measurement data*. Submitted to the Journal of Finite Elements in Analysis and Design.
- [18] Trim A. D., Braaten, H., Lie, H. and Tognarelli, M. A., *Experimental Investigation of Vortex Induced Vibration of long Marine Risers*. Journal of Fluids and Structures, 21(2005), 335-361.
- [19] Baarholm, R., Recent MARINTEK. *activities on assessment of Vortex-Induced Vibrations. PowerPoint presentation*, MARINTEK do Brazil Opening Seminar, Rio de Janeiro, April 19, 2007.
- [20] Lie, H., Mo. K. and Vandiver, J. K., *VIV Model Test of a Bare and Staggered Buoyancy Riser in a Rotating Rig*. OTC Paper No. 8700, Houston, May 1998.
- [21] Jie Wu, PhD thesis, *Hydrodynamic Force Identification from Stochastic Vortex Induced Vibration Experiments with Slender Beams*. Page 72. NTNU, Trondheim, Norway.
- [22] Larsen, C.M., Lie, H., Passano, E., Yttervik, R., Wu, J. and Baarholm, G. S., *VIVANA Theory Manual. Version 3.7*, 2009, Trondheim. Norway.
- [23] Franklin, G. F., Powell, J. D., and Workman, M. L., *Digital control of dynamic systems*. Addison-Wesley, 1998.
- [24] Yin. D. and Larsen, C. M., *on determination of VIV coefficients under shear flow condition*. OMAE 2010-20306, 29th International Conference on Ocean, Offshore and Arctic Engineering. Shanghai, China. 2010.

-
- [25] Aglen, I.. *Importance of Added Mass for the Interaction between IL and CF Vibrations of Free Spanning Pipelines*. OMAE 2011-49966, 30th International Conference on Ocean, Offshore and Arctic Engineering, Rotterdam, Netherlands, 2011.
- [26] Kyrre Vikestad. and Larsen C. M.. *Norwegian Deepwater Program: Damping of Vortex-Induced Vibrations*. OTC 11998, Presentation at the 2000s Offshore Technology Conference, Houston, 2000.
- [27] AMOG. and Deepstar. *Specification for VIV predictions and Measurements-NDP 38m Riser Model*. T2010.j052.001, Australia, 2011.
- [28] Stig Berge. *Fatigue and Fracture Design of Marine Structures*. Department of Marine Technology ,NTNU, Trondheim, 2006.